Hybrid entanglement for quantum communication

Isaac Mphele Nape

A Dissertation submitted to the Faculty of Science
in partial fulfillment of the requirements for the Degree of
Master of Science

School of Physics

University of Witwatersrand

Supervisor: Prof Andrew Forbes
Co-supervisor: Dr Melanie McLaren
November 1, 2017

Declaration

I declare that this Dissertation is my own, unaided work. It is being submitted for the Degree of Master of Science at the University of the Witwatersrand, Johannesburg. It has not been submitted before for any degree or examination at any other University.

_____

(Signature of candidate)

_____1_____ day of ___November___ 20 _____17_____ in__Johannesburg__

Abstract

The generation and detection of entangled photons is a topic of interest in quantum communication. With current state-of-the-art methods it is possible to manipulate any degree of freedom (DoF) of photons, e.g, polarisation, transverse momentum, orbital angular momentum and energy. Furthermore, it is possible to combine these DoF to realise hybrid entanglement – entanglement between the DoF of photons. In this dissertation we focus on hybrid entanglement between photon states of coupled orbital angular momentum and polarisation.

We engineer hybrid-entanglement using geometric phase control between spatially separated photons produced from spontaneous parametric down conversion. We present a new type of quantum eraser that does not rely on physical path interference. We show that in principle any other degree of freedom can be used and demonstrate this effectively through polarisation control.

The use of high dimensional hybrid photon states in quantum communication, particularly in quantum cryptography, is still in its infancy. Here we tailor photon states that are coupled in their polarisation and spatial DoF (orbital angular momentum) to realise high dimensional encoding alphabets. We show how photons entangled in their internal DoF can be generated and deterministically detected. We exploit them in a demonstration of a high dimensional quantum key distribution protocol and show that our scheme generates secure keys at high rates.

Acknowledgments

I would like to acknowledge the following people:

My supervisor Prof. Andrew Forbes, your guidance, mentoring and encouragement has helped me find my feet in the scientific world. Your detailed planning and insightful discussions saw this work to its completion. Notably, your influence has stimulated my obsession for delivering quality and outstanding results. For that reason, you have become a scientist I chose to model myself to.

My co-supervisor Dr. Melanie McLaren, Bienvenu Ndagano, Dr. Carmelo Rosales-Guzman, Benjamin Perez-Garcia and Stirling Scholes for their immense contributions. The work in this dissertation would not be successfully conducted without them. In particular Dr. Melanie McLaren and Bienvenu Ndagano, I thank you for helping me accelerate my learning and putting up with all my questions.

Dr. Daryl Naidoo from the National Laser Center (NLC) for encouraging me to be my best. You are one of my a role models. Prof Thomas Konrad and Dr. Philipus Roux from the University of KwaZulu Natal and National Metrology Institute of South Africa (NLC) for their stimulating conversions.

My family and friends for their continuous support and encouragement. Thank you for lending an ear. Your every attempt to understand my work and celebrate some of my accomplishments during the course of this work will not be forgotten.

Contents

List of Figures

List of Tables

Publications

Journal papers

1. **Nape, I.**, Ndagano, B. and Forbes, A., *"Erasing the orbital angular momentum information of a photon"*. *Physical Review A*, 95(5), p.053859, 2017.

2. **Nape, I.**, Kyeremah, C., Valls, A., Rosales-Guzmn, C., Buah-Bassuah, P.K. and Forbes, A., *"A hybrid quantum eraser scheme for characterization of free-space and fiber communication channels"*. *Optics Communications*, 2017.

3. Ndagano, B., **Nape, I.**, Perez-Garcia, B., Scholes, S., Hernandez-Aranda, R.I., Konrad, T., Lavery, M.P. and Forbes, A., *"A deterministic detector for vector vortex states"*. *Scientific Reports*, 7(1), p.13882, 2017.

Archived

1. **Nape, I.**, Ndagano, B., Perez-Garcia, B., Scholes, S., Hernandez-Aranda, R.I., Konrad, T. and Forbes, A., *"High-bit-rate quantum key distribution with entangled internal degrees of freedom of photons"*, arXiv preprint arXiv:1612.09261, 2016.

International conferences

1. Ndagano, B., **Nape, I.**, Perez-Garcia, B., Scholes, S., Hernandez-Aranda, R.I., Roux, F.S., Konrad, T. and Forbes, A., *"Quantum-key distribution with vector*

modes", *SPIE Proceedings Vol. 10120*, 2017.

2. **Nape, I.**, Ndagano, B. and Forbes, A., "*Hyper-entanglement for secure communication*", *International Workshop on Structured Light and Matter: Concepts and Applications*, Iran, Poster, 2016.

3. **Nape, I.**, A., "*Creation and detection of high dimensional quantum states for quantum communication*", *Quantum Africa 4*, Tunisia, Invited Talk, 2017.

National Presentations

1. **Nape, I.**, Ndagano, B. and Forbes, A., "Hyper-entanglement for quantum key distribution", *61st Annual Conference of the South African Institute of Physics*, Talk, 2016.

2. **Nape, I.**, Ndagano, B. and Forbes, A., "*Quantum eraser with vector modes*", *Quantum Information Processing Communication and Control 4*, Talk, 2016.

3. **Nape, I.**, Ndagano, B. and Forbes, A., "*High dimensional quantum key distribution with vector modes*", *62nd Conference of the South African Institute of Physics*, Poster, 2017.

4. **Nape, I.**, Ndagano, B. and Forbes, A., "*Delayed measure quantum eraser with orbital angular momentum*", *62nd Annual Conference of the South African Institute of Physics*, Talk, 2017.

Chapter 1

Introduction

Quantum entanglement is a phenomenon that characterises spatially separated quantum systems that cannot be described independently regardless of their separation distance [1]. Its applications range from quantum computation [2], teleportation [3], superdense coding [4, 5] to quantum cryptography [6, 7]. Most protocols in quantum communication manipulate individual degrees of freedom (DoF) of photons. However, it was recently realised that combining multiple DoF can benefit quantum communication where the unique qualities of each DoF can be exploited [8]. Remarkably, this has led to the development of hybrid entangled photon states where spatially separated systems can be tailored to exhibit entanglement between particles defined in differing DoF [9]. Analogously, the same non-separability can be observed in single photons and intense beams between their polarisation and orbital angular momentum (OAM) DoFs [10]. As such, we are drawn to the implementation of photon states of combined polarisation and the high dimensional OAM DoF. This raises the possibility of benefiting from increased dimensionality of encoding alphabets. In this chapter we review the concept of hybrid entanglement and introduce spin angular momentum and orbital angular momentum. Furthermore we review an application relevant to quantum communication, namely quantum key distribution.

1.1 Quantum entangled states

'Verschränkung' which translates as entanglement from German to English, was the term used by Schrödinger when referring to a class of quantum systems with qualities that had no classical counterparts. The intriguing nature of such systems was first discovered earlier in 1935 when Einstein, Padolsky and Rosen (EPR) published a paper in which they attempted to expose the incompleteness of the quantum mechanical description of nature [11]. They realised that a system containing two spatially separated quantum subsystems with perfectly correlated positions and momenta (EPR states) could not be described as independent quantum systems. Consequently, this meant that a measurement on one of the subsystems would instantaneously affect the outcome of another – a violation of local relativistic causality and realism in classical mechanics. Furthermore, they suggested that there must exist local hidden variables that could account for this miraculous and instantaneous random exchange of information between the two subsystems, finally concluding that the quantum description of reality was not complete.

It was in 1964 when Bell showed that quantum entanglement rules out the possibility of using any local hidden variable theories to describes the correlations manifested by entangled system. He derived inequalities that constrained the statistical correlations of a two particle system (see derivation in App. A) under the EPR assumptions [12]. In this approach, he ascribed values to the system prior to measurement with the aim of predicting the outcomes of the bipartite (two particle) measurements. This was motivated by the assumption that the two subsystems had a property which they held in common. Interestingly, he showed that the inequalities could be maximally violated by a collection quantum systems that admitted maximal correlations – known as Bell states.

1.1.1 Bell states

An elegant way of representing Bell states is through the Dirac notation [13]. In the Dirac notation, the corresponding quantum state of a system is represented by a state

vector that can be mapped onto a d dimensional Hilbert space ($\mathcal{H}_d$). The vector is represented as a ket, $|\cdot\rangle$, and has a complex conjugate called the bra $\langle\cdot|$. Consider the collection of eigenstates $\{|i\rangle\}$ spanning $\mathcal{H}_d$ and describing a single particle (e.g a photon). By the superposition principle the quantum state of the particle can be written as

$$|\psi\rangle = \sum_{i=0}^{\infty} a_i |i\rangle, \tag{1.1}$$

with $|a_i|^2$ being the probability of the particle occupying one of the orthonormal states, $|i\rangle$, with a normalisation condition following $\sum_{i=0}^{\infty} |a_i|^2 = 1$. For a compound system of spatially separated particles A and B belonging to subspaces $\mathcal{H}_A$ and $\mathcal{H}_B$ with each subspace spanned by the basis states $|i\rangle_A$ and $|j\rangle_B$, respectively. The quantum state of the compound system can be written as

$$|\psi\rangle = \sum_{ij=0}^{\infty} a_{ij} |i\rangle_A \otimes |j\rangle_B. \tag{1.2}$$

Here, $|a_{ij}|^2$ represents the probability of the system being in a product state $|i\rangle_A \otimes |j\rangle_B$ (commonly written as $|i\rangle_A |j\rangle_B$). Equation (1.2) is separable if the total quantum state can be written as a product of the two sub systems, i.e,

$$|\psi\rangle = |\phi\rangle_A \otimes |\varphi\rangle_B, \tag{1.3}$$

where $|\phi\rangle_A = \sum_{i=0}^{\infty} b_i |i\rangle_A$ and $|\varphi\rangle_B = \sum_{j=0}^{\infty} c_j |j\rangle_B$ represent the states of the individual subsystems. Conversely, the system in Eq. (1.2) is said to be entangled if $a_{ij} \neq b_i c_j$. This provides us with a definition of entanglement that depends on the non-separable superposition of compound quantum states with a condition that the systems are correlated even when spatially separated. Bell states are a collection of quantum states with maximal correlations. A well known example is the set constructed from the qubit logical basis $\{|0\rangle, |1\rangle\}$ taking the form

$$|\psi\rangle_{AB}^{\pm} = \frac{1}{\sqrt{2}}(|0\rangle_A \otimes |1\rangle_B \pm |1\rangle_A \otimes |0\rangle_B), \tag{1.4}$$

$$|\phi\rangle_{AB}^{\pm} = \frac{1}{\sqrt{2}}(|0\rangle_A \otimes |0\rangle_B \pm |1\rangle_A \otimes |1\rangle_B). \tag{1.5}$$

Here A and B denote two spatially separated subsystems. Equation (1.4) and Eq. (1.5) cannot be written in the form of Eq. (1.3). Moreover, a projection onto of the eigenstates of subsystem A determines the outcome of subsystem B. For example according to $|\psi\rangle_{AB}^{+}$ (Eq. 1.4), when subsystem A is projected onto the state $|0\rangle$, subsystem B instantaneously collapses into the state $|1\rangle$ due to the entanglement shared between the two subsystems. The Bell states form a four dimensional orthogonal basis which has previously been exploited in superdense coding for the transfer of quantum information [5] using polarisation states.

1.1.2 Density matrix

Another way of presenting quantum states is through a statistical operator called the density matrix. For pure states, the density matrix takes the following form

$$\rho = |\psi\rangle \langle\psi|, \tag{1.6}$$

which is idempotent ($\rho^2 = \rho$), has a trace of unity and is positively definite, i.e., that it has positive eigenvalues. From the density matrix, measures such as the degree of entanglement and entropy can be obtained, offering alternative ways of determining if quantum states are entangled or separable and provide an indication of their purity. We will later explore a technique for reconstructing the quantum state of entangled photons carrying orbital angular momentum (OAM).

1.2 Hybrid entanglement

Photon pairs described by Bell states have been experimentally prepared with single DoF such as polarisation [14–16], time [17–19] and orbital angular momentum [20–23]. That is, the Bell states given in Eq. (1.4) and Eq. (1.5) can be written in a single DoF of the photon with each of its eigenstates associated with a state from the logical basis. However, the two spatially separated photons can each be defined in differing degrees of freedom resulting in a hybrid entangled system.

The Bell state associated with a hybrid entangled quantum state can be written in the logical basis $|0\rangle$, $|1\rangle$ as

$$|\psi\rangle_{AB} = \frac{1}{\sqrt{2}}(|0_\sigma\rangle_A |1_\pi\rangle_B \pm |1_\sigma\rangle_A |1_\pi\rangle_B). \tag{1.7}$$

Here the subscripts σ and π correspond to the DoF of each photon. This system is maximally entangled and therefore photons A and B are correlated in their respective DoF. The measurement on one photon determines the outcome of the measurement in the DoF corresponding to its entangled twin. For example, projecting photon A onto the state $|0_\sigma\rangle_A$ in the σ DoF, collapses photon B onto the state $|1_\pi\rangle_B$ in the π DoF. The system can be described on the Hilbert space that results from the tensor product of the individual Hilbert spaces of each photon, $\mathcal{H}_{\sigma,2} \otimes \mathcal{H}_{\pi,2}$. Significantly, systems described by Eq. (1.7) have played a crucial role in the development of quantum eraser experiments wherein the particle-wave duality of photons is investigated through polarisation-path hybrid entanglement [24–26].

In this dissertation, we wish to explore the hybrid entanglement that can be generated involving the components of the angular momentum of photons, namely, spin angular momentum (SAM) and orbital angular momentum (OAM).

1.3 Spin angular momentum

Spin angular momentum (SAM) is associated with the circular polarisation of light. Photons carrying SAM have an angular momentum of $\pm\hbar$ per photon. The sign
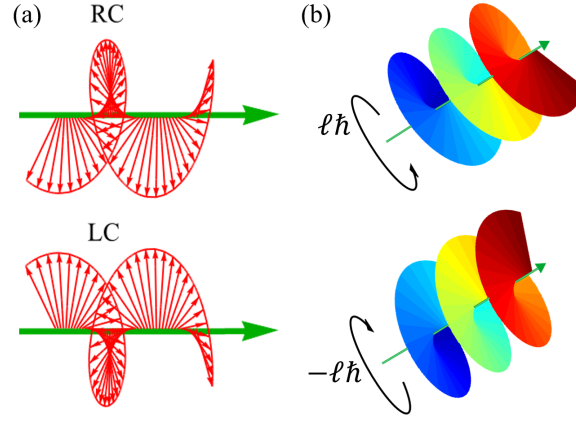
Figure 1-1: (a) An illustration of the electric field oscillations for the right (RC) and left (LC) circular polarisations corresponding to SAM. (b) illustrates the handedness of azimuthal phase rotations corresponding to the amount of OAM ($\pm\ell\hbar$) per photon where the wavefront has ℓ twists per wavelength.

depends on the handedness of their spins. The quantum states associated with spins can be represented by ket vectors, $|L\rangle$ and $|R\rangle$, representing the right circular and left circular spin eigenstates, respectively. For many photons, SAM corresponds to the rotation of the electric fields about the beam axis as illustrated in Fig. 1-1(a). In general, all polarisation states can be described by a two dimensional state-space (See Fig. 1-2(a)) called the Poincaré sphere [27].

The poles contain the orthogonal circular polarisation eigenstates while the equator contains the linear polarisation states such as the horizontal $|H\rangle$, vertical $|V\rangle$ and rectilinear diagonal $|D\rangle$ and anti-diagonal $|A\rangle$ states.

Photons encoded in the polarisation DoF allow for qubit manipulations. Qubits are a quantum measure of information analogous to classical bits in classical information theory. Unlike classical bits, qubits can occupy multiple states (bit values) simultaneously. Significantly, the encoding alphabet, which is restricted to two alphabets with qubits, can be increased by considering alternative DoFs such as the orbital angular momentum.
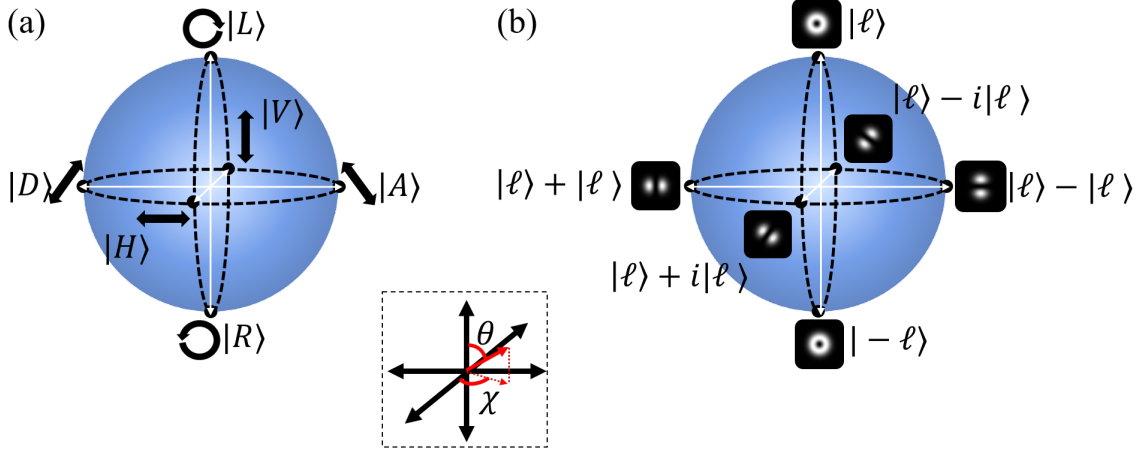
Figure 1-2: (a) Poincaré sphere for polarisation DoF and (b) its analogue , the Bloch sphere, for the OAM DoF in the $|\ell| = 1$ subspace. The symbols are described in the text. Any state on the surface of the sphere can be described using the azimuthal (θ) and elevation angles (χ).

1.4 Orbital angular momentum

The orbital angular momentum (OAM) of light is a component of the total angular momentum that is associated with the transverse spatial profile of photon. Allen et al. [28] showed that beams propagating with helical phase fronts characterized by an azimuthal phase variation, $e^{i\ell\phi}$, carry an angular momentum of $\ell\hbar$ per photon, where ℓ is an integer called the topological or azimuthal charge representing the number of azimuthal rotations (or spirals) in a single wavelength depending on the direction of the spiraling phases [29–32] (See Fig. 1-1(b)). The main feature of these beams is a vortex that is at the origin of the beam cross-section, having an intensity distribution that resembles a donut like structure.

The mode function of OAM beams can be found by solving the Helmholtz equation

$$(\nabla^2 + k^2)u(\mathbf{r}) = 0. \tag{1.8}$$

Here ∇^2 is the Laplacian, $\frac{\partial^2}{\partial^2 x} + \frac{\partial^2}{\partial^2 y} + \frac{\partial^2}{\partial^2 z}$ in Cartesian coordinates, k represents the magnitude of the wave-vector and $u(\mathbf{r})$ is the field function.Under the paraxial approximation (the limit of small beam divergence in the traverse plain) it can be
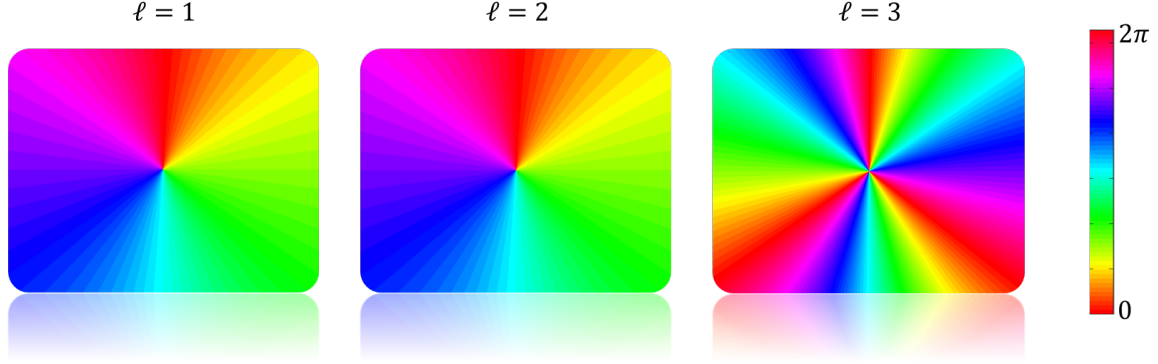
Figure 1-3: An example of azimuthal phase variations for topological charges $\ell = 1, 2, 3$ for any spatial mode with an azimuthal transverse profile characterised by $e^{-\ell\phi}$.

assumed that $u(\mathbf{r})$ is a slowly varying function of z, i.e., the paraxial inequality [27]

$$|\frac{\partial^2}{\partial^2 z}u((r))| << k\frac{\partial}{\partial z}u(\mathbf{r}), \tag{1.9}$$

can be satisfied. Subsequently, Helmholtz equation can be approximated by

$$(\nabla_\perp^2 + ik^2)u(\mathbf{r}) = 0, \tag{1.10}$$

where $\nabla_\perp^2$ represents the transverse part of the Laplacian. The general solutions to this equation in cylindrical coordinates are

$$U(r, \phi, z) = U(r, z)e^{i\ell\phi}. \tag{1.11}$$

Here r and ϕ are the azimuthal and radial coordinates, ℓ is the azimuthal charge and $U(r, z)$ is the radial profile of the beam. These solutions have the characteristic eigenfunction $e^{i\ell\phi}$ of OAM modes.

The family of modes that take up the description given in Eq. 1.11 include Laguerre-Gaussian (LG) [28], Ince-Gaussian modes [33] and Bessel-Gaussian (BG)
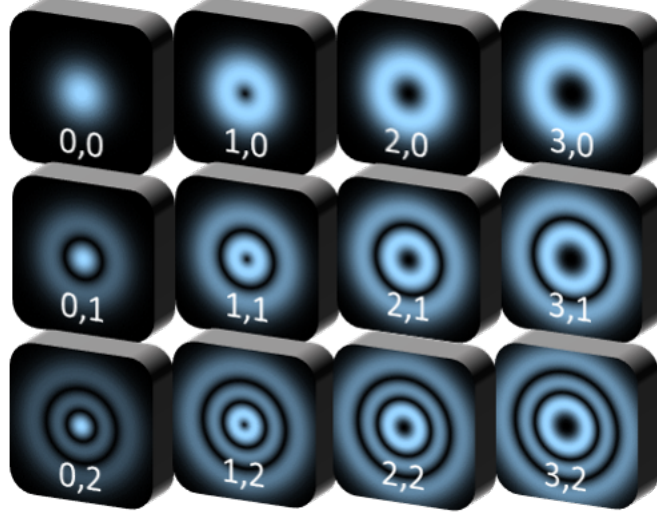
Figure 1-4: An illustration of the transverse profile of $LG_{\ell,p}$ modes with varying ℓ azimuthal and p radial indices. The modes are labed in (ℓ, p) pairs where ℓ increase to the right and p increases downwards. As ℓ increase the size of the vortex increases and as p increases so do the the number of concentric rings. For $p > 0$, p+1 concentric rings are observed.

[34] modes. For LG modes the solution is

$$LG_{\ell,p} = \sqrt{\frac{2^{|\ell|+1}p!}{\pi(p+|\ell|)!}} \frac{1}{\sqrt{w(z)}} L_{p,l}\left(\frac{2r^2}{w^2(z)}\right)\left(\sqrt{2}\frac{r}{w(z)}\right)^{|\ell|} e^{-\frac{-r^2}{w^2(z)}} \quad (1.12)$$

$$\times e^{-ik\frac{r^2 z}{2(z_R^2+z^2)}} e^{i\ell\phi)} e^{-i(2p+|\ell|+1)\tan^{-1}\left(\frac{z}{z_R}\right)}.$$

Here ℓ, p represents the azimuthal and radial indices and $L_{p,\ell}(x)$ represents the Laguerre polynomials. For $\ell > 0$ one will observe $p + 1$ concentric rings around the origin of the beam cross-section with ℓ determining the size of the vortex (see Fig. 1-4). The beam waist, $w(z)$, is given along the z axis as

$$w(z) = w_0\sqrt{\frac{z^2 + z_R^2}{z_R^2}}, \quad (1.13)$$

with w_0 being the beam waist when $z = 0$, where z_R is the Rayleigh range which is defined as the distance where beam cross-section doubles. The cross-section is given by $\frac{\pi w(0)^2}{\lambda M^2}$ where λ is the wavelength of the beam. Here $M^2 = 2p + \ell + 1$ is called the beam quality factor and describes the deviation of the beam from an ideal Gaussian beam having $M^2 = 1$.
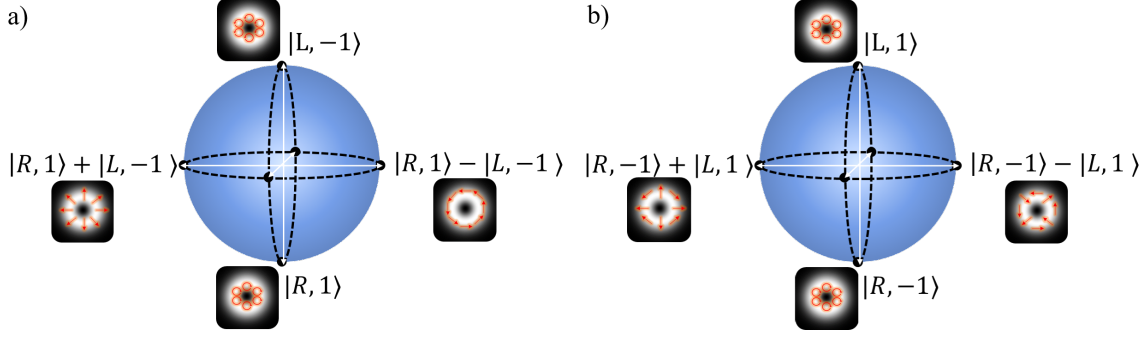
Figure 1-5: Higher order Poincaré sphere for the subspaces spanned by (a) $\{|R\rangle, |L\rangle\} \otimes \{|1\rangle |-1\rangle\}$ and for (b) spanned by $\{|R\rangle, |L\rangle\} \otimes \{|-1\rangle |1\rangle\}$.

LG modes (and any other set of OAM modes) can be described on an analogous state-space to the polarisation Poincaré sphere called the Bloch sphere (see Fig. 1-2.(b)). The north and south poles are the basis states $e^{i\ell\phi} \sim |\ell\rangle$ and $e^{-i\ell\phi} \sim |-\ell\rangle$ and the superposition states are found on the equator. In general, any point on the sphere can be written as,

$$|\psi_{\ell\theta\chi}\rangle = \cos\left(\frac{\theta}{2}\right) e^{i\chi} |\ell\rangle + \sin\left(\frac{\theta}{2}\right) e^{-i\chi} |-\ell\rangle. \tag{1.14}$$

Where θ is the angle measured with respect z axis the sphere and χ is measured with respect the xy plane. A unique sphere can be constructed for each ℓ allowing for a description of the OAM modes on the infinite Hilbert space.

1.5 Hybrid spin-orbit coupled photon states

The family of OAM modes that where considered in Sec. 1.4 have linear polarisation states throughout the cross section of a beam. One can describe a family of OAM modes with coupled to polarisation states as a complete set of modes. These modes can be described on the higher order Poincaré sphere [35] (see Fig. 1-5). This state space is a tensor product of the polarisation qubit ($\mathcal{H}_2$) and the OAM qudit ($\mathcal{H}_d$) spaces , respectively. The resulting Hilbert space is $\mathcal{H}_2 \otimes \mathcal{H}_d$. Each subspace is a span of the scalar mode basis $\{|R\rangle |\ell\rangle, |L\rangle |-\ell\rangle, |R\rangle |-\ell\rangle, |L\rangle |\ell\rangle\}$.

Two qubit spheres can be constructed from the scalar mode basis where the po-
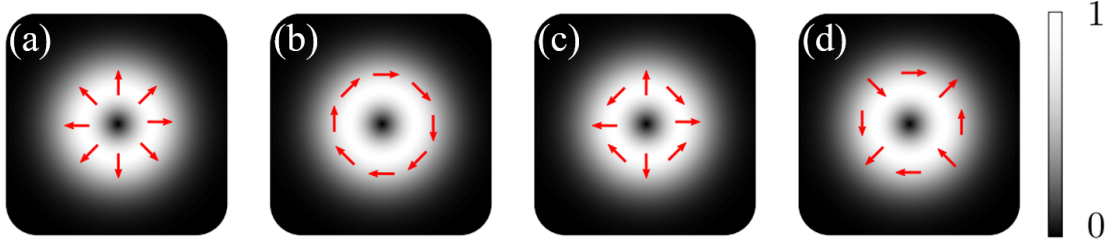
Figure 1-6: Examples of vector vortex modes: (a) is known as the radial mode and (b) is the azimuthal mode while (c) and (d) are the hybrid electric modes.

larisation and OAM handedness are the same (see Fig. 1-5 (a)) and were they are opposite (see Fig. 1-5 (b)). The poles of the spheres represent orthogonal scalar modes of circular polarisation states coupled to OAM modes while the equator contains non-separable superpositions states. The non-separable superposition states take the following form

$$|\psi\rangle_\ell = \frac{1}{\sqrt{2}}(|R\rangle\,|\ell\rangle \pm |L\rangle\,|\ell\rangle),\qquad(1.15)$$

resembling a maximally hybrid entangled Bell state with a non-separability in the OAM and polarisation DoF. Photons described by Eq. (1.15) are called vector modes. The non-separability of the OAM and polarisation of vector modes has been reported using a Bell-like inequality with classical (laser) light [36] and at the single photon level [37, 38]. Similarly, demonstrations involving polarization and momentum DoF of heralded single photons [39] and with spatial and spin DoF of single neutrons [40] have been reported. Classically, vector modes represent a class of spatial modes that have spatially varying polarisation states [41–43] (see Fig. 1-6). They offer the advantage of increasing the photon encoding alphabet, relevant for high communication high bandwidth communication. They been exploited in classical for optical communication [44], more recently for quantum error correction [45], and in quantum cryptography for their rotational invariance [46] allowing for the development of alignment free quantum channels. Interestingly, their high dimensional characteristic has not been explored for applications in quantum cryptography which may benefit from high dimensional encoding alphabets at the single photon level [47, 48].

It is worth noting to the reader that although vector modes share an equivalent mathematical description as hybrid entangled states, they are not entangled quantum states as described in Sec. 1.1 (with non-locality). However, we say that the internal DoF are entangled to emphasize their non-separability. We will present experiments that exploit each instance (of hybrid entanglement and vector modes) independently, showing discrepancies between the two physical descriptions.

1.6 Quantum communication

1.6.1 Quantum key distribution

One of the application we wish to explore in quantum communication is quantum key distribution. Messages exchanged between banks, military intelligence, airlines, etc, mostly depend on computationally difficult problems to generate encryption keys. An example of a computationally difficult problem is the factorisation of a number obtained from multiplying two large prime numbers. This is a method commonly used to produce secure keys in RSA cryptography. Only a party with knowledge of the two prime numbers can gain access to encrypted messages [49]. Such methods are under threat by quantum computers, known to one day perform factorisation promptly [50]. The solution to this problem is provided by nature through quantum key distribution.

Quantum key distribution (QKD) belongs to the broader field of quantum cryptography in quantum communications. It harnesses the properties of quantum mechanics to solve the problem of securely generating and distributing encryption keys using single photons. Bennett and Brassard proposed the first prepare and measure protocol (BB84) [6] and later Ekert, in 1991 developed an entanglement based protocol (E91) [7].
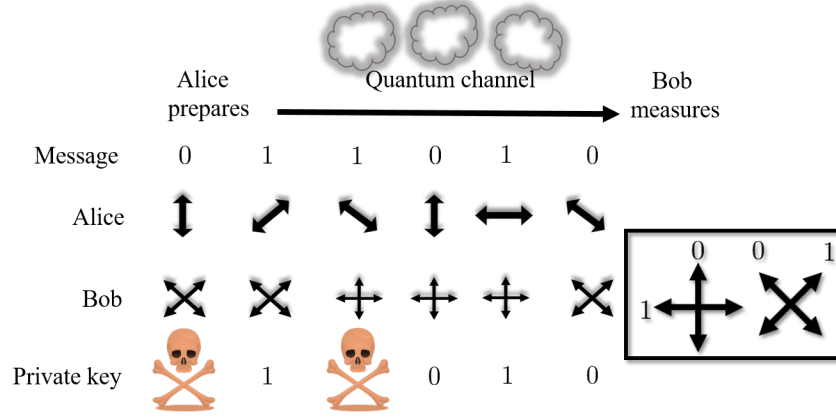
Figure 1-7: An illustration of the BB84 prepare and measure protocol. Alice would encode a photon with one of the polarisation states from their MUB of linear and rectilinear polarisation states associated with logical bit values. Bob then selects a measurement orientation randomly. After N transmissions they reconcile their selections and discard bits that are not correlated. The remaining bits are to establish the secure key with which information is encrypted.

1.6.2 The BB84 protocol

In the BB84 protocol, Alice and Bob would randomly choose between two mutually unbiased bases (MUB) of polarisation states (Fig. 1-7) satisfying the following criterion [51]

$$| \langle \psi_i, \phi_j \rangle |^2 = \frac{1}{d} \quad (i,j = 1..d), \tag{1.16}$$

where $\{|\psi_i\rangle\}$ and $\{|\phi_j\rangle\}$ are d is the dimensional encoding basis. For polarisation d=2. Equation (1.16) means that projections between the two bases do not yield a distinguishable result. If the linear $\{|H\rangle, |V\rangle\}$ polarisation basis is selected as a standard basis then the rectilinear $\{|D\rangle = \frac{1}{\sqrt{2}}(|H\rangle + |V\rangle), |A\rangle = \frac{1}{\sqrt{2}}(|H\rangle + |V\rangle)\}$ basis qualifies as an MUB to he linear polarization basis. Alice can encode her photon with one of the polarisation states (selected at random) and transmit it to Bob whom randomly selects a measurement orientation between the bases. After N transmissions, they reconcile the states Alice prepared and the states Bob measured and discard the ones that do not correlate. The remaining bits form a secure key. At most 50% of the bits will form the key. Some of the errors introduced into their key

may result from eavesdropping. Remarkably, quantum mechanics ensures that the presence of the eavesdropper can be detected and that they cannot obtain enough information key. This is reflected by the no-cloning theorem.

1.6.3 The no-cloning theorem and eavesdropping

In order to gain knowledge of Alice and Bob's key they, the eavesdropper has to determine the basis chosen by Alice during her transmissions or clone the quantum state of Alice's transmitted photon and subsequently send an identical copy to Bob. However, it is impossible to fully clone the quantum state of a quantum system. We will demonstrate a proof by contradiction.

Suppose that an eavesdropper, Eve, has a machine that can clone the linear polarisation states as follows

$$|H\rangle_A |\alpha\rangle_E \rightarrow |H\rangle_A |H\rangle_E \,,$$
$$|V\rangle_A |\alpha\rangle_E \rightarrow |V\rangle_A |V\rangle_E \,, \tag{1.17}$$

were $|\alpha\rangle_E$ is an initial state of Eve's (E) photon or the 'blank' state. If Alice's photon was prepared in the linear polarsation state upon entering the machine, it exits with Eve's photon, the clone, encoded with the same linear polarisation. The process collapses when Alice sends a superposition of the linear polarisations, i.e, the diagonal polarisation state ($|D\rangle$). By the linearity of quantum mechanics and Eq. 1.17

$$|D\rangle_A |\alpha\rangle_E \rightarrow \frac{1}{\sqrt{2}} |H\rangle_A |H\rangle_E + \frac{1}{\sqrt{2}} |V\rangle_A |V\rangle_E). \tag{1.18}$$

The transformation in Eq. (1.18) does not produce the state $|D\rangle_A |D\rangle_E$ and therefore Eve cannot clone superposition states of Alice's photons. This also holds for arbitrary superpositions. In general there are no machines (operators) that can produce a perfect copy of any arbitrary quantum state. This is called the no-cloning theorem [52, 53].

The no-cloning theorem also means that the eavesdropper can introduce errors into the message from Alice to Bob transmissions that can be detected once Alice and Bob reconcile their prepared and measured states – a feature that cannot be found in any classical cryptography techniques. If errors are found in the key they must all be attributed to Eve [54].

1.6.4   The secure key rate

The secure key rate (R) is a measure of the rate at which Alice and Bob are able to generate secure keys. The lower bound on the secret key rate for a d-dimensional basis is given by [55]

$$R = \log_2(d) + 2F \log_2(F) + 2(1 - F) \log_2 \left(\frac{1 - F}{d - 1} \right), \tag{1.19}$$

where $F = \frac{1}{n} \sum_k^n F_k$ with F_k being the fidelity of Bob's measurements in the kth basis of n MUBs. The error rate of their transmission is $Q = 1 - F$ (see [56] for description of Q). Here F_k is obtained from

$$F_k = \frac{1}{d} \sum_i^d \sum_j^d Tr \left[P_{k,j}^{B\dagger} U_c^\dagger P_{k,i}^{A\dagger} \rho_A P_{k,i}^A U_c P_{k,j}^B \right], \tag{1.20}$$

with ρ_A being the initial density matrix of Alice's single photon, $P_{k,i}^A$ and $P_{k,j}^B$ being the projection on the single photon by Alice (prepared) and Bob (measured), respectively, onto a state from the kth basis and U_c is a unitary operator characterising the transformation by the quantum channel. For a near perfect system, the effects of the environment are minimal and therefore U_c can be approximated to unity. Since $P_{k,j}^B$ and $P_{k,j}^B$ are projection operators from the same Hilbert space then $F_k = 1$ if the states within each basis are orthogonal. The key rate, R, now depends on the dimension of the MUBs. A theoretical plot based on the assumptions above is presented in Fig. 1-8. The keys rates increases with dimensionality. For polarisation, this sets the limit to 1 bit per photon. This limitation has raised interest in the development of protocols that exploit high dimensional ($d > 2$) DoF.
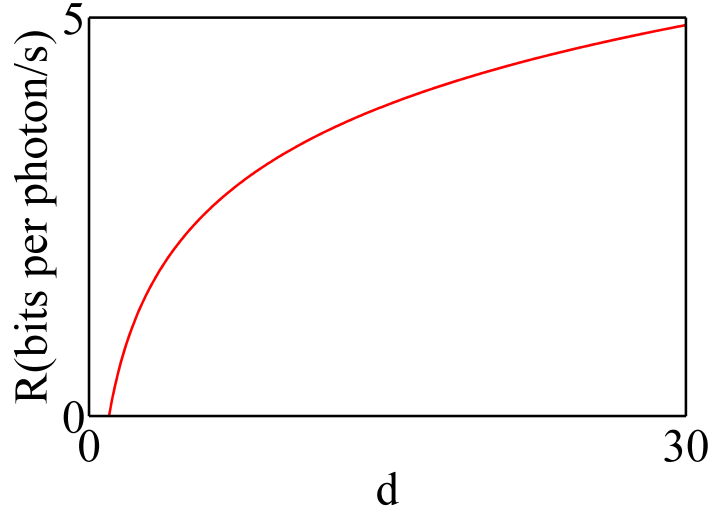
Figure 1-8: Theoretical secure key rate (R) vs encoding basis dimensions (d) assuming a perfect fidelity of $F \approx 1$.

The highest dimensions QKD protocols reported to date are d=11 [57], d=7 [58] and d=4 [56] using traverse momentum and orbital angular momentum of photons. These schemes exploit a single DoF and it may be interesting to ask whether combining multiple DoFs, as in hybrid entanglement, could benefit the protocol and increase the rate at which secure keys are generated. As part of this study we will attempt to use hybrid photonic states of coupled DoF (polarisation and OAM) to realise high dimensional quantum key distribution.

Outline

Our work is structured as follows: In chapter 2 we will demonstrate the techniques used to generate spatial modes that carry orbital angular momentum. We will explore two techniques based on liquid crystal display technology, namely spatial light modulaters (SLM) and specially designed geometric phase plates with a spatially varying optical axes. Significantly, the detection of these modes is crucial for quantum communication and therefore we will demonstrate projecive measurement techniques classically with a Fourier lens and at the single photon level using a single mode fiber

coupled to a single photon detector.

In Chapter 3 we demonstrate a method of generating entangled photons via spontaneous parametric down-conversion (SPDC) which enables for the generation of entangled photons pairs from a non-linear crystal. To detect the entangled photons we implement the projective measurement technique from the previous Chapter 2. The alignment and characterisation of the experimental set-up will be demonstrated in a prepare and measure scheme, called back projection, based on a retroactive argument of quantum entanglement. We show that our non-linear crystal produces photon pairs that conserve orbital angular momentum and subsequently confirm the entanglement of the system via a Bell inequality violation. We will evaluate the fidelity, linear entropy and concurrence of the SPDC photons by performing a full state tomography.

In Chapter 4 we employ SPDC to generate the entangled photons and use geometric phase control to establish hybrid entanglement where the polarisation of one photon is entangled to the OAM of its entangled twin, enabling us to perform the experiment in delayed measure mode. Will show how the which-way quantum eraser can be performed with polarisation-OAM entanglement by replacing the idea of tradition physical double slits with the concept of virtual slits defined in the orbital angular momentum of a photon. Analogous to the traditional which-way experiment we will show that it is possible to erase the OAM information of a photon through polarisation control of its entangled twin.

Lastly, in Chapter 5 we will demonstrate the potential of using high dimension encoding of hybrid photon states for quantum key distribution. We will present a set of scalar (with separable DoF) and vector modes (with entangled DoF) that establish a mutual unbiased basis and use the geometric phase control, a technique from Chapter 2, to generate them. We will also present a hybrid (exploiting the coupled DoF) deterministic detection system that enables us to sort the modes into unique positions yielding a higher photon efficiency and secure key rates than probabilistic detection methods.

Chapter 2

Experimental techniques

Quantum communication with photons depends on the ability to generate and detection photon states unambiguously. In this chapter, we explore the techniques required to generate and detect photons with OAM-polarisation coupled DoF. We focus on techniques that exploit the dynamic and geometric phase of light. These techniques will become useful in the generating and detecting hybrid photon states in subsequent chapters.

2.1 OAM mode generation via dynamic phase
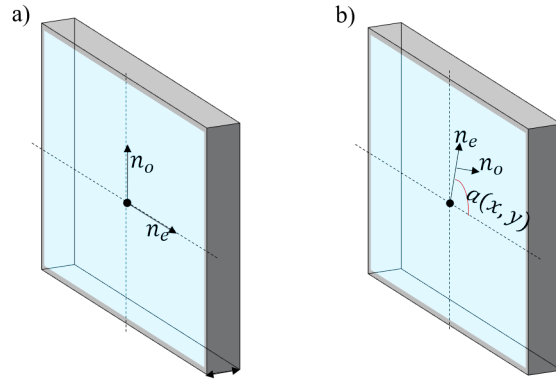
Figure 2-1: (a) An optical element with a uniform birefringence (polarisation dependent refractive index) imparts a dynamic phase on the extraordinary (e) and ordinary rays (o). The phase of a beam can be varied by changing the width of the optical element or by varying the index of refraction ($n_{o,e}$). If the plate is isotropic, the extraordinary and ordinary rays experience the same dynamic phase change, e.g. in lenses. (b) Geometric optical elements have an inhomogeneous anisotropy, owing to the varying optic axis. The optical axis lies parallel to the extraordinary ray. The optics axis orientation is given by $\alpha(x, y)$. Subsequently, the geometric phase change is proportional to $2\alpha(x, y)$

.

Dynamic phase is a feature found in optical elements that affect the path and propagation time of light through a variation in the thickness (d) or the refractive index of a medium (see Fig. 2-1(a)) and this can be exploited to generate OAM modes. Dynamic phase can be written as

$$\delta_d = 2\pi \frac{(n_e + n_o)d}{\lambda}, \tag{2.1}$$

where λ is the wavelength of light in a vacuum, n_e and n_o are the refractive indexes that the extraordinary and ordinary rays experience in the medium, respectively. The extraordinary rays are aligned to the axis where there is rotational invariance of the refractive index about that axis, also known as the optic axis. In contrast, the ordinary rays are perpendicular to the optic axis. The dependence of a beams refractive index on its polarisation is called birefringence. Not all optical elements exhibit this feature, for example, in lenses the polarisation of a beam is independent of rotations about any axis and therefore the refractive index is uniform in all directions.

This is called isotropy.
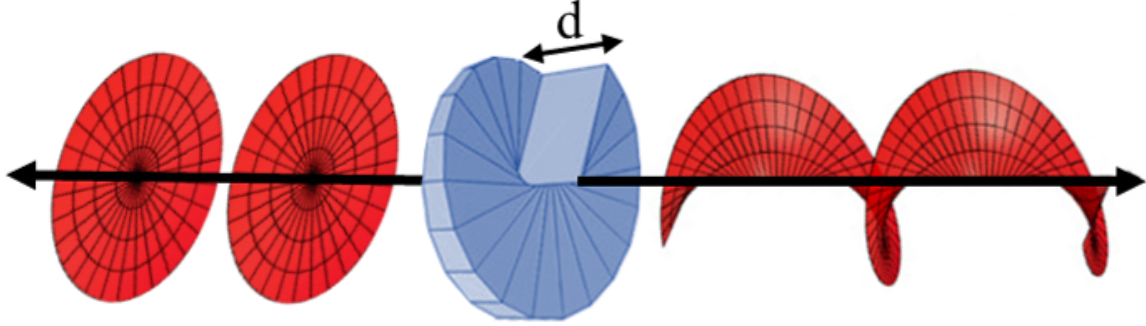
Figure 2-2: OAM mode generation using spiral-phase plates. A beam with a flat wavefront is incident on the spiral glass and subsequently gains a helical phase with an OAM proportional to the depth of the azimuthal step in wavelengths.

Spiral-phase plates are examples of optical elements that can be used to generate OAM beams through dynamic phase control [59]. These are transparent optical elements with a spiral depth (d) and a uniform refractive index (see Fig. 2-2). In spiral-phase plates a beam with a complex field $\psi(r, z)$ and flat wavefront undergoes a transformation

$$\psi'(r, z) \rightarrow \psi(r, z)e^{-i\Delta\ell\phi}, \tag{2.2}$$

with $\Delta\ell = \frac{nd}{\lambda}$ being the depth of the phase plate in wavelengths and $2\pi\Delta\ell$ is the phase difference (equivalent to Eq. (2.1)). The transmitted beam now has a helical transverse profile and carries an OAM of $\Delta\ell\hbar$. The spiral-phase plate relies on the varied depth of the plate to impart OAM on an incident beam. However, the same phase change can be achieved by fixing the thickness and varying the refractive index of the material. This can be done with liquid crystal technology that enables phase information to be encoded on computer controlled displays, called spatial light modulators (SLM), enabling for the digital control of dynamic phase. SLMs use liquid crystals (LC), an interface between the liquid and solid matter phase, to modulate either the amplitude or phase of light. The liquid crystals are sandwiched between an array (pixels) of electrodes (see Fig. 2-3). The orientation of the crystals is varied with an applied voltage between the electrodes enabling each pixel's refractive index
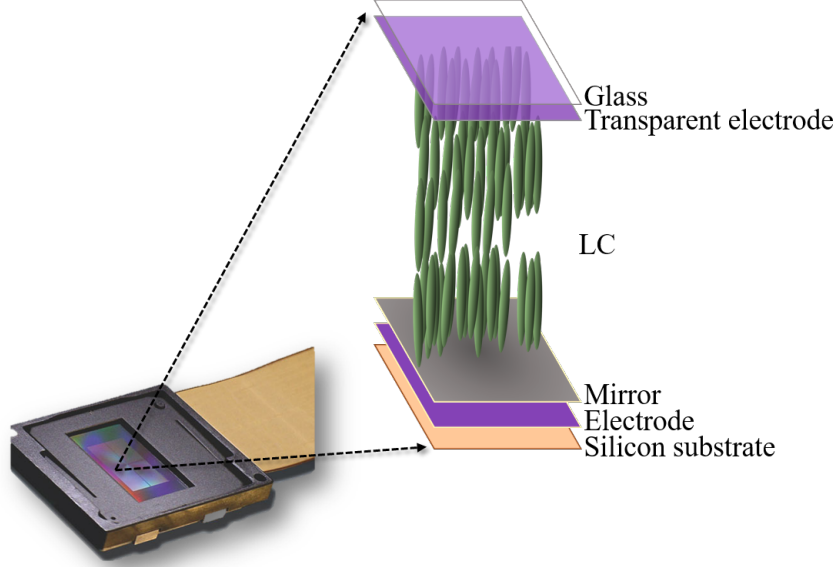
Figure 2-3: An illustration of an SLM screen that operates in reflective mode. Each pixel contains liquid crystals (LC), sandwiched between electrodes, glass and a silicon substrate.The addition of a mirror serves to reflect the incident beam once it has interacted with the LCs. The index of refraction that light sees when interacting with each pixel depends on the orientation of the LCs. The orientation is controlled by a applied voltage across the electrodes

.

to be tailored. The resulting phase change is

$$\delta_d \propto \frac{2\pi V L}{\lambda}. \tag{2.3}$$

Here V is the voltage applied across the electrodes and L is the depth of each pixel. The birefringence of LC's enable for the modulation of horizontally polarised light (aligned to the slow axis). Since the voltage determines the index of refraction, it follows that the retardation is varied through voltage control enabling fast variation of the phase information encoded in each pixel.

We use a Holoeye PLUTO phase-only SLM, designed to modulate the phase of an incoming beam and not its amplitude. The display of the SLM has a 1920×1080 pixel resolution where each pixel is 8 μm in size with an 8-bit encoding capacity that can be addressed with a gray scale image ranged from 0 (black) to 255 (white) corresponding

to a 0 to 2π phase shift. The grey levels are associated with the alignment of the crystals and therefore depend on the applied voltage. The pixels have a 50 Hz refresh rate. Moreover, it functions in reflective mode (see schematic of the SLM display in Fig. 2-3).

Vortex (OAM) modes can be generated using SLMs through phase modulation by encoding the phase-front associated of the desired field onto the SLM. This is associated with a transmission function

$$T_\ell(\phi) = e^{i\ell\phi}, \tag{2.4}$$

where ϕ is the azimuthal coordinate and ℓ is the topological charge of the OAM. Subsequently, the argument of the transmission function is encoded on the SLM screen as a gray scale image. To generate the vortex mode, a Gaussian beam would interact with the hologram and the desired phase fronts would be diffracted into the first order of the output beam. Unfortunately, not all the incident light interacts with the hologram. The light that is not modulated (zeroth order) propagates on axis with the diffracted first order. This causes them to interfere. To retrieve the modulated light, a periodic grading is added to separate the first and zeroth order which can then be isolated with a aperture. Now, the transmission function is

$$T_\ell(\phi) = e^{-i\ell\phi+2\pi\frac{x}{t_x}}. \tag{2.5}$$

with t_x being the period of the grating and x is the (Cartesian) coordinate. The diffraction orders will be spread in the horizon of the SLM. Note that any direction may be chosen for the grating. For example, replacing the x coordinate with the y coordinate, spreads the orders vertically. A typical generation and detection scheme is shown in Fig. 2-4. As illustrated, a Gaussian beam ($\ell = 0$) with flat wavefronts is prepared and subsequently interacts with the computer generated hologram phase only encoded with the argument of the desired transmission function. Interestingly, due to the reciprocity of light, the reverse operation is true. For example a mode carrying an azimuthal charge of $\ell = 1$ incident on the hologram will be modulated

22
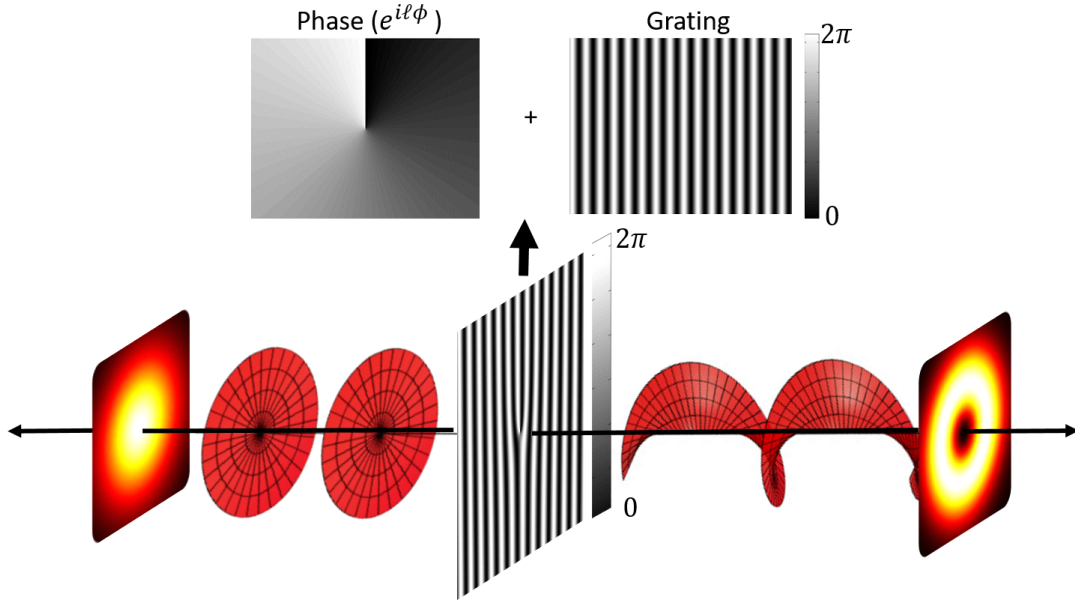
Figure 2-4: Mode generation and detection using holograms encoded on an SLM. A Gaussian beam with a flat wavefront is incident on a phase-only SLM encoded with an azimuthal phase profile. The output is a donut mode with a helical wavefront. The reciprocal nature of light allows the reverse operation to serve as a method where the spatial mode is projected onto a Gaussian mode.

into a Gaussian mode. This is desirable for measuring single photon states as the modulated photon can be coupled into a single-mode fiber (SMF) which has maximum transmission when the mode of the photon is Gaussian. Therefore the combination of the SLM and the SMF perform a projective measurement of the spatial mode of the incoming photon [60] (to be discussed later).

2.2 OAM mode generation via geometric phase

In the previous section the polarisation of the photons was ignored due to to its uniformity across the beam. For example an OAM mode generated with an SLM can be uniformly horizontally polarised since the SLM only modulates the component of the polarisation that is aligned to the slow axis of them liquid crystals. Thus the polarisation and OAM are separable and can be treated independently. Vector vortex modes have non-separable polarisation (spin) and OAM (orbit). Interestingly,
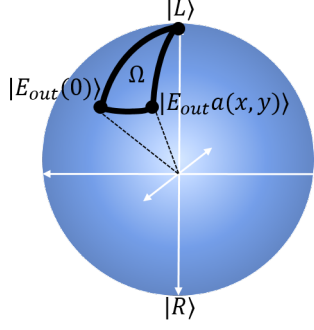
Figure 2-5: An illustration of the geometric phase as defined by for a photon traversing a geometric phase optical element with an optical axis defined by $\alpha x, y$. According to Berry [70], the geometric phase is equal to half the solid angle enclosed by the loop.

a measurement of the polarisation (spin) determines the outcome of the spatial field [36, 37]. Earlier methods of generating vector modes relied on axial birefringence [61–63] or dichroism [64, 65] in intra-cavity bulk devices. Birefringence is a property of optical materials that is associated with the dependence of polarisation on the refractive index. The previous generation methods are polarisation selective and force a laser cavity to oscillate in a desired cylindrically symmetric vector mode. SLMs have been used for the generation of vector modes by superimposing scalar modes with orthogonal polarisations in path interferometers [66–68]. With this scheme, the phase and amplitude can be tailored as desired although phase instability and misalignment still remain a challenge. It ia possible to generate vector modes with single optical elements that have a spatially varying optical axis. Their transformation is similar to that of half-wave plates but with a locally varying birefringence (anisotropy) [69].

2.2.1 Geometric phase

In contrast to dynamic phase, geometric phase or Pancharatnam-Berry phase does not rely on the optical path of the beam, it depends on the geometric orientation of the optical axis found in inhomogeneous anisotropic materials. In these materials, the extraordinary (n_e) and ordinary (n_o) refractive indices are spatially varying (Fig. 2-1b). If the orientation of the optic axis is given by a geometrical parameter $\alpha(x, y)$, and assuming a half-wave ($\frac{\lambda}{2}$) phase retardation, then the operator associated with

this optic element is [71],

$$M\big(\alpha(x,y)\big) = R\big(\alpha(x,y)\big) J_\pi R\big(-\alpha(x,y)\big)$$

$$= \begin{bmatrix} \cos(2\alpha(x,y)) & \sin(2\alpha(x,y)) \\ \sin(2\alpha(x,y)) & -\cos(2\alpha(x,y)) \end{bmatrix} \tag{2.6}$$

where $J_\pi = \begin{bmatrix} 1 & 1 \\ 1 & -1 \end{bmatrix}$ is the operator associated with a half wave retarder written in

the linear polarisation basis $\{|H\rangle = \begin{bmatrix} 1 \\ 0 \end{bmatrix}, |V\rangle = \begin{bmatrix} 0 \\ 1 \end{bmatrix}\}$ and $R\big(\alpha(x,y)\big)$ is the rotation

operator. This acts as a half-wave ($\frac{\lambda}{2}$) plate that performs localised transformations of the beam's polarisation. Suppose an input beam has the following field description,

$$|E_{\text{in}}\rangle = E_o |R\rangle, \tag{2.7}$$

with $|R\rangle = \frac{1}{\sqrt{2}}(|H\rangle - i|V\rangle)$ and E_o being the amplitude. The operator $M(x,y)$ acting on $|\psi_{\text{in}}\rangle$ yields the following output

$$|E_{\text{out}}(\alpha(x,y))\rangle = E_o M\big(\alpha(x,y)\big)|R\rangle$$

$$= E_o e^{-2\alpha(x,y)}|L\rangle, \tag{2.8}$$

where $|L\rangle = \frac{1}{\sqrt{2}}(|H\rangle + i|V\rangle)$ is the left circular polarisation state. The spin of the input field has been inverted and accumulates a phase front proportional to $e^{-2\alpha(x,y)}$ that depends on the geometric parameter of the optic axis. Pancharatman showed that the geometric phase can be calculated from $i \times \arg(\langle E_{\text{in}}(0)|E_{\text{out}}(\alpha(x,y))\rangle)$. It follows that the geometric phase for the transformation given by $M(x,y)$ is $-2\alpha(x,y)$ if the input state is $|R\rangle$ polarisation state. Note that it only depends on the geometric parameter of the optical element. Similarly for a beam that is prepared in the left circular polarisation state, $|L\rangle$, the accumulated geometric phase is $2\alpha(x,y)$.

In general the geometric phase is given by $\Delta\Phi(x,y) = \pm 2\alpha(x,y)$, relying on the handedness of the input polarisation and the geometry of the optic element. Berry
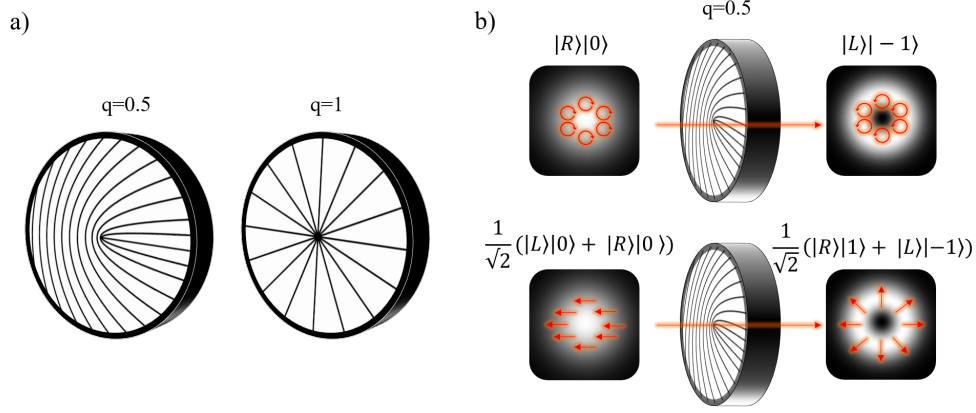
Figure 2-6: (a) An illustration of the geometry of the spatially varying optic axis for q-plates with charges $q = 0.5$ and $q = 1$. (b) An illustration of spin-orbit coupling with a q-plate that has a $q = 0.5$. Scalar OAM modes with a homogeneous state of polarisation and vector modes with inhomogeneous states of polarisation can be generated with an incident g.

showed that the phase accumulation is due to a cyclic evolution of the field [70], this is illustrated in Fig. 2-5. This will become useful in the generation of hybrid-entangled photon states with using q-plates for spin-orbit coupling.

2.2.2 q-plates for vector mode generation and detection

Q-plates are geometric phase elements that couple the polarisation (spin) and orbital angular momentum of light [71]. As a result, hybrid photonic states (photon states with coupled DOF) have been generated with q-plates and exploited for applications in quantum communications at the classical and quantum level [10].

The geometry of the q-plate is given by $\Delta\alpha(\phi) = q\phi$, where q characterises the charge of the plate. Remarkably, the accumulated phase front, $e^{\pm i2q\phi}$, corresponds to an OAM eigenstate $|\pm 2q\rangle$ for a field carrying an angular momentum of $\pm 2q\hbar$ per photon and depending on the input handedness of the input polarisation. The transformation of the q-plate is governed by the following rules

$$|L\rangle\,|\ell\rangle \xrightarrow{\text{q-plate}} |R\rangle\,|\ell + 2q\rangle \tag{2.9}$$

$$|R\rangle\,|\ell\rangle \xrightarrow{\text{q-plate}} |L\rangle\,|\ell - 2q\rangle\,, \tag{2.10}$$

following the half-wave operator given in where $|\ell\rangle$ is the initial OAM mode of the input field. Note the use of Dirac notation $(|\cdot\rangle_{\text{spin}}|\cdot\rangle_{\text{orbit}})$. Here, the incident circular polarisation is inverted and with an additional OAM of $\pm 2q$. For example if a right circularly polarised Gaussian beam $(|R\rangle|\ell = 0\rangle)$ is incident on the q-plate, the polarisation becomes left handed with an OAM of $-2q\hbar$ (see Fig. 2-6). This is called spin to orbit conversion [72] where all the spin of the photon is converted into orbital angular momentum. This will become useful in generating spin-orbit hybrid entanglement. Furthermore, this process is useful for generating scalar modes since the output polarisation is uniform.

To generate vector modes, photons need to be prepared in superposition states of circular polarised photon states and Gaussian profiles for example in the horizontal polarisation state $\frac{1}{\sqrt{2}}(|L\rangle|0\rangle + |R\rangle|0\rangle)$. Applying the transformation of the q-plate yields $\frac{1}{\sqrt{2}}(|R\rangle|m\rangle + |L\rangle|-m\rangle)$ which is a non-separable superposition of OAM and spin (polarisation) reminiscent of a hybrid entangled state with $m = 2q$. Due to the reciprocity of light, the reverse process also holds and enables us to use the q-plate to detect the scalar and vector modes. At this point it is important to note that these transformations also hold at the single photon level.

Experimental scalar and vector mode generation and detection

We demonstrate the experimental generation of scalar and vector mode sets. Our set of scalar modes is comprised of orthogonal photon states with circular polaristions coupled to OAM modes defined in the $|\ell| = \pm 1$ subspaces. Moreover, we selected a set of orthogonal vector modes that take the form

$$|\psi\rangle_{\ell,\theta} = \frac{1}{2}(|R\rangle|\ell\rangle + e^{i\theta}|L\rangle|-\ell\rangle), \tag{2.11}$$

where the OAM is defined in the $\ell = \pm 1$ subspace and θ is a relative phase which can be tailored by manipulating the polarisation of the initial beam before interacting with the q-plate using a $\frac{\lambda}{2}$ wave-plate. We generated the radial mode $|\psi\rangle_{1,0}$, azimuthal mode $(|\psi\rangle_{1,\pi})$ and the hybrid electric modes $|\psi\rangle_{-1,0}$ and $|\psi\rangle_{-1,\pi}$. In Fig. 2-7 we
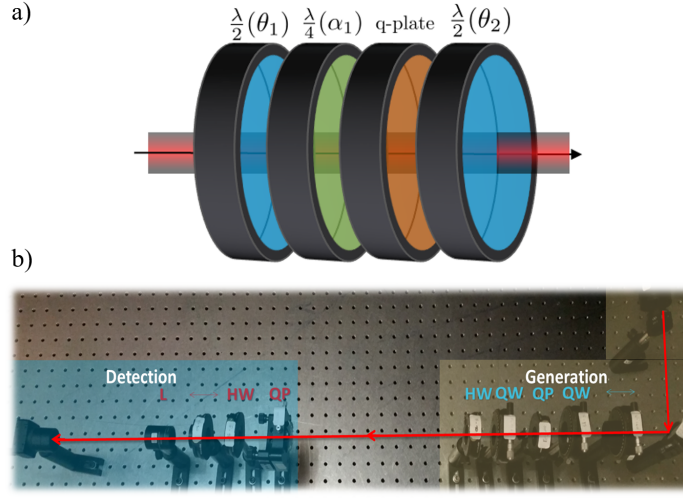
Figure 2-7: (a) The vector and scalar modes are generated using a q-plate and wave plates ($\lambda/2$ and $\lambda/4$). We use the $\lambda/4$ wave plates to convert between linear and circular polarisation states and the $\lambda/2$ plates to rotate between desired linear polarisation states. The generation scheme assumes an input of horizontally polarised light with a Gaussian profile ($|H\rangle\,|0\rangle$). (b) Generation and detection via modal decomposition where the overlap is observed in the far-field of the Fourier lens with where the on axis intensity is recorded. We used a helium-neon (HeNe) laser as a light source and a charge couple device (CCD camera) as a detector. We use a Fourier lens to perform the overlap by measuring the on axis intensity in the far-field (focal length of the lens) [60].

present the experimental set-up used to generate and detect scalar and vector modes. To generate the scalar modes, the wave plates are arranged as illustrated in Fig. 2-7(a). However, to generate the vector modes the $\frac{\lambda}{4}$ plates are removed since they rotate polarisation states from circular and linear and vise-versa.

Table 2.1: Generation of our scalar and vector mode sets from an input horizontally polarised Gaussian beam. The wave-plate angles are defined with respect to the fast axis of each plate.

Mode	$\lambda/4(\alpha_1)$	$\lambda/2(\theta_1)$	q-plate	$\lambda/2(\theta_2)$
$|R\rangle\,|\ell\rangle$	$-\pi/4$	$-$	0.5	$-$
$|L\rangle\,|\ell\rangle$	$-\pi/4$	$-$	0.5	$\pi/2$
$|R\rangle\,|-\ell\rangle$	$\pi/4$	$-$	0.5	$\pi/2$
$|L\rangle\,|-\ell\rangle$	$\pi/4$	$-$	0.5	$-$
$|\psi\rangle_{\ell,0}$	$-$	0	0.5	$-$
$|\psi\rangle_{\ell,\pi}$	$-$	$\pi/4$	0.5	$-$
$|\psi\rangle_{-\ell,0}$	$-$	0	0.5	0
$|\psi\rangle_{-\ell,\pi}$	$-$	$\pi/4$	0.5	0

28

The set-up in Fig. 2-7(b) is used to prepare and measure the modes sets, we exploit the reciprocity of light to detect the modes; the plates are re-stacked in the reverse order to detect the modes. The prescribed orientations of the plates are presented Table. 2.1. We used a Helium-Neon (HeNe) laser as a light source followed by the wave plates for generation and detection. After traversing the detection and generation plates we observe the optical overlap in the far field. This is achieved by using a Fourier lens. To illustrate this consider the inner product between two functions

$$
\begin{aligned}
c_i \quad &= \langle \psi_i | \Phi \rangle \\
&= \int \int \psi_i^*(x,y) \Phi(x,y) dx dy,
\end{aligned}
\tag{2.12}
$$

where $\psi_i(x,y)$ can represent a target mode that we wish to overlap with a field $\Phi(x,y)$. To perform this inner product optically, a generated field $\Phi(x,y)$ interacts with an optical element corresponding to the function ψ_i. The resulting field is $F(x,y) = \psi_i(x,y) \times \Phi(x,y)$. This field can be Fourier transformed using a Fourier lens. It follows that

$$
\mathcal{F}\{F(x,y)\} \quad = \int \int \psi_i^*(x,y) \Phi(x,y) e^{i(k_x x + k_y y)} dx dy,
\tag{2.13}
$$

where $k_{x,y}$ are the transverse spatial frequencies. Experimentally we can only evaluate the field intensity. We restrict our measurement to the on axis intensity therefore $k_{x,y} = 0$. It follows that Eq. (2.13) takes the form

$$
|\mathcal{F}\{F(0,0)\}|^2 = |\int \int \psi_i^*(x,y) \Phi(x,y) dx dy|^2,
\tag{2.14}
$$

which is the $|c_i|^2$, calculated from the inner product in Eq. (2.12). Therefore this forms a projective measurement for optical fields [60]. For $\Phi(x,y) = \psi_j(x,y)$ we obtain $|c_i| = \delta_{i,j}$. This motivates our use of a far-field on axis intensity measurement to detect the overlap based on the the set-up in Fig. 2-7(b).
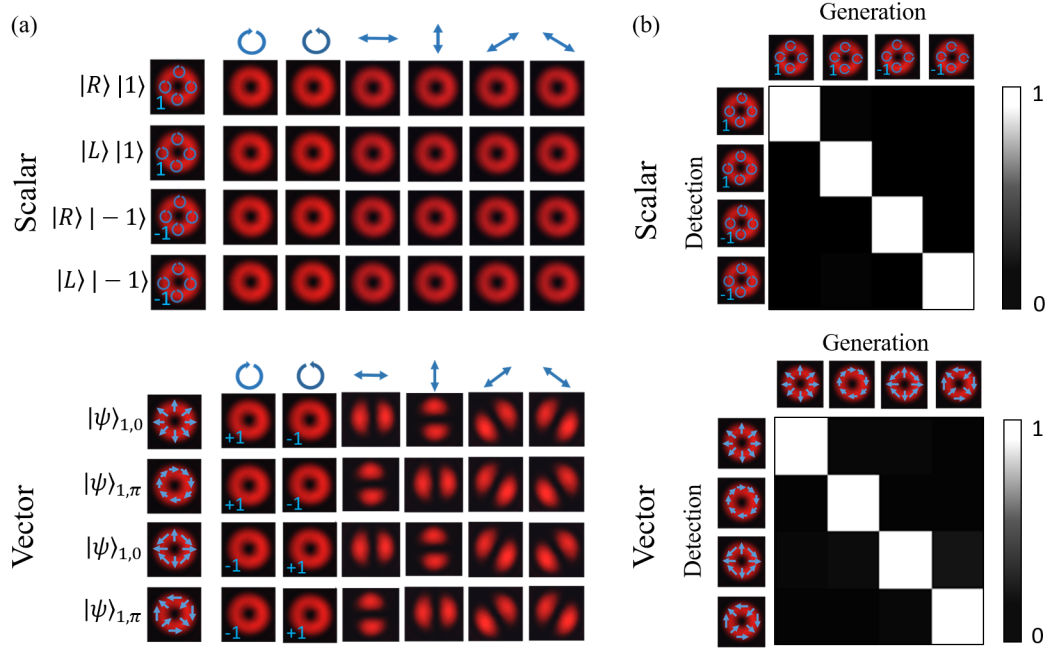
Figure 2-8: Experimental scalar and vector mode decomposition with q-plates. (a) illustrates the dependence of the spatial structure of the mode sets by performing polarisation projections of each generated mode. The scalar modes show no variation of the polarisation while the vector modes show a dependence of the spatial structure resulting from polarisation projections. The petals structures are HG modes modes which are superpositions of oppositely charged OAM modes, $|\ell| = 1$ in our case. This confirms the non-separability of the vector modes. (b) prepare and measure results of the scalar and vector modes presented in the form of a density matrix. Each channel (in the matrix) represents an overlap between a prepared and measured mode equivalent to an overlap performed in quantum mechanics.

Experimental results

In Fig. 2-8(a) we show that the spatial structures of the scalar modes are invariant of the polarisation projection by taking CCD images of the intensities after polarisation projections and that the vector modes show a variation in their spatial structure when projected onto linear polarisation states. For the vector modes, linear polarisation projections yield petals which rotate according to the angle (χ) of the polariser. Since a polariser orientated at an angle χ projects onto the target state $|\chi\rangle = \frac{1}{2}(|R\rangle + e^{i\chi}|L\rangle)$, the result of the projection is

$$\langle\chi|\psi\rangle_{\ell,\theta} = \frac{1}{\sqrt{2}}(|1\rangle + e^{i(\theta-\chi)}|-1\rangle), \tag{2.15}$$

30
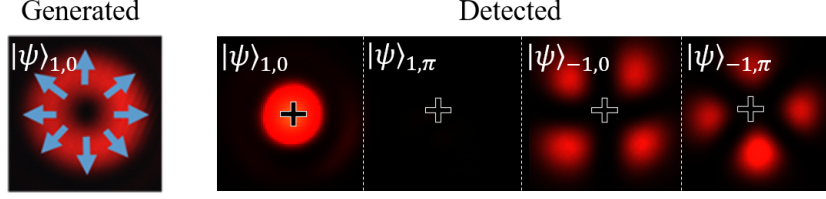
Figure 2-9: Experimental decomposition of the radially polarised mode in-terms of the vector mode set.

an OAM superposition state of $|1\rangle$ and $|-1\rangle$ with a relative phase that varies with χ. This explains the rotating petal structure observed on the CCD camera when the polariser is oriented at χ. Rotating the polarisers is therefore equivalent to projecting the vector mode onto the equator of the Bloch sphere. Projections of this form have been used to demonstrate the violation of a Bell-like inequality to confirm the non-separability between the polarisation and OAM DoF of vector vortex modes [36].

The experimental normalised intensities as obtained from the optical inner-product measurements are presented in Fig. 2-8(b) as a density matrix plots, within each mode set, showing maximal on axis intensities when the prepared and measured modes correlate. For example when a radially polarised mode ($|\psi\rangle_{1,0}$) is prepared and the detection side is oriented to measure a radially polarised mode, a high on axis intensity is observed. However, detection orientations corresponding to the other modes yield a minimal (≈ 0) on axis intensity (see Fig 2-9). The diagonal matrices in Fig. 2-8(b) show that each set is orthogonal. This is essential in optical communication and therefore each mode set can be used to encode information.

2.3 Projective measurement for single photon OAM states

In the previous section we showed that optical inner products can be performed using q-plates for hybrid photon states with classical light. Now we present a technique for performing an inner product for spatial modes at the single photon level.
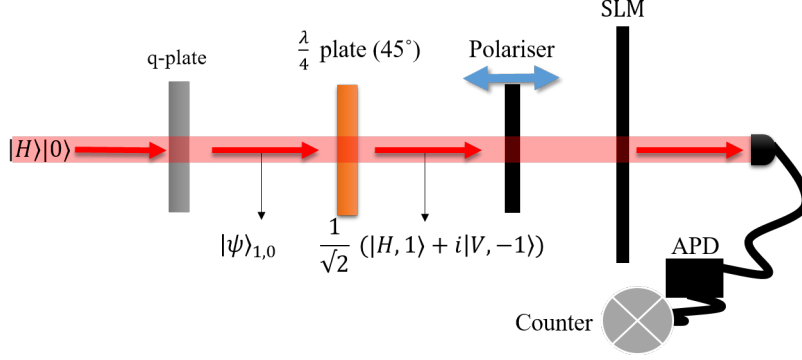
Figure 2-10: The experimental set up for measuring the OAM content of a vector mode at the single photon level. The blue arrow corresponds to the alignment of the polarizer and can be rotated at various angles.

Experimentally, the inner product between the quantum state corresponding to the measurement apparatus and that of the photon is proportional to photon counts. We use an avalanche photo-diode (APD) to count the single photons. APDs can be coupled to single mode fibers (SMF). The SMF collects the light which is fed the APD. This triggers avalanche currents that are converted into digital signals that can be processed using a counting card. In our lab we use PerkinElmar single photon counting modules (SPCM) connected to a 6602X counting card.

We generated the radial mode ($|\psi\rangle_{1,0}$ see Eq. (2.11)) the q-plate. To measure the OAM content, we convert the polarisation of the vector from circular to linear using a $\frac{\lambda}{4}$ wave-plate. This transforms the radial mode,

$$|\psi\rangle_{\ell,0} \rightarrow \frac{1}{\sqrt{2}}(|H\rangle |1\rangle + i |L\rangle |-1\rangle), \qquad (2.16)$$

where $|H\rangle$ and $|V\rangle$ are the linear horizontal and vertical states of polarisation. In this way, we can select between a pure OAM mode and and superposition of OAM modes through polarisation control. For example, filtering the $|H\rangle$ polarisation state collapse the photon onto the $|1\rangle$ state and by filtering a superposition $|H\rangle + |V\rangle$, the photon collapses the photon onto the state $|1\rangle + i |-1\rangle$.

We the detect the resulting spatial mode using a SLM coupled to a single mode fiber (SMF) and APD. This combination served as our projective measurement.

To illustrate how it works, consider the normalised quantum state $|f\rangle$ representing

a spatial field of prepared photons and a normalised state $|g\rangle$ to be encoded on a SLM. After modulation with the SLM and coupling the photons into the fiber, the probability of the photon arriving at the APD is

$$P = \frac{1}{\mathcal{N}} \int \int g^*(x,y) f(x,y) G(x,y) dx dy. \qquad (2.17)$$

Here $G(x,y)$ is the Gaussian profile $(G(x,y) = \frac{1}{w\sqrt{2\pi}} e^{\frac{-(x^2+y^2)}{w^2}})$ if a beam where emerging from the SMF. Equation (2.17) can be expressed as $P = \langle f,g|G\rangle$, in this form the inner product is distorted by the fiber – P does not take the form $\langle g|f\rangle$. Furthermore, note that the integral is maximal if and only if $g^*(x,y)f(x,y) = G(x,y)$. This can be satisfied with OAM modes since they can be modulated into Gaussian modes by encoding their complex conjugate on the SLM.

Using this measurement technique we probed the mode content of our prepared photons, by scanning through OAM eigenmodes in the range $\ell = [-5,5]$ with an integration time of 3 sec for photon counting. We normalised the counts by the sum of all photon counts to conserve probability. We did not subtract the background counts of the system to demonstrate the effects of noise resulting form dark counts. Dark counts are registered by the APD in the absence of of light. They are caused by the thermal emission of electrons and can be reduced by cooling the detectors. Significantly, increasing the photon flux may help reduce the signal to noise ratio however this must be done taking care not to saturate the detectors. In Fig. 2-11(a) we present the OAM spectrum after filtering the polarisation state $|H\rangle$ of Eq. (2.16), resulting in photons collapsing onto the OAM mode $|1\rangle$. The spectrum shows a dominant presence of the $|1\rangle$ mode. Similarly, a projection of the polarisation state onto the superposition state $\frac{1}{\sqrt{2}}(|H\rangle + |V\rangle)$ (by rotating the polariser to 45°) shows a maximal transmission of superposition of the $|\pm 1\rangle$ OAM modes as expected. It is worth noting that the photon counts dropped to half since the SLM only modulates the horizontal polarisation components of the photons.
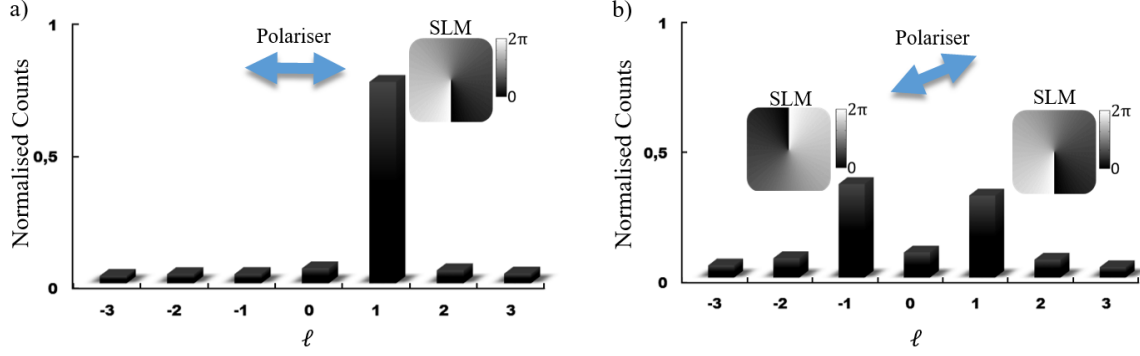
Figure 2-11: Experimental photon counts for modal (OAM) decomposition using an SLM for horizontal (a) and diagonal (b) polarisation projections of a vector mode.

2.4   Conclusion

In this chapter we have demonstrated the use of dynamic and geometric phase for generating and detecting the orbital angular momentum of photons. We generated and detected a set of 4 dimensional scalar and vector modes with q-plates. The modes where prepared with intense light from a laser source and detected using and projective measurement analogous to an inner-product in quantum mechanics. Our results showed that each mode set is orthogonal. Furthermore, we demonstrated a projective measurement for single photons using a SLM and a single mode fiber coupled to a single photon detector. We used a q-plate and polariser to filter an OAM state and a superposition, subsequently showing that our digital projective measurements can reveal the OAM content of single photons. The q-plate and SLM will become useful in preparing hybrid entanglement and as a digital spatial mode detector, respectively.

Chapter 3

Spontaneous parametric down-conversion

In this chapter we explore the techniques needed to generate and detect photons entangled in the orbital angular momentum (OAM) degree of freedom (DoF). We make of use of spontaneous parametric down-conversion (SPDC), a process that occurs in non-linear crystals, to generate the entangled photon pairs. We detect the entangled photons with the aid of the digital holographic projective measurement technique illustrated in Chapter 2. Furthermore, we confirm the entaglement of our system via a Bell inequality violation and perform a full state tomography.

3.1   Theory and background

SPDC can be used as a source of entangled photon pairs. Burnham and Weinberg [73] were the first to report the detection of photon pairs at spatially separated detectors using SPDC. This method was favoured over atomic cascading techniques [14], since SPDC could constrain the direction of the photon emission making photon collection easier and more efficient. Significantly, through SPDC, quantum entanglement with various DoF has been reported, e.g polarisation [16,74–76], time-bin encoding [17–19], linear momentum [77,78] and photon orbital angular momentum [20–23], making it an ideal source for generating photons. The generation of the entangled photons with
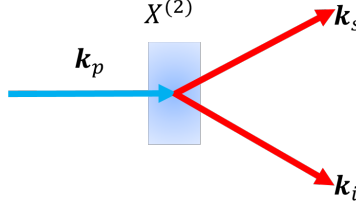
Figure 3-1: An illustration of spontaneous parametric down-conversion in nonlinear crystals. A high frequency pump (p) photon interacts with a non-linear crystal, characterised by a second order non-linear susceptibility ($\chi^{(2)}$). The crystal spontaneously converts the input photon into two lower frequency daughter photons (signal (s) and idler (i)) satisfying energy and momentum conservation laws. The photons are correlated in energy, momentum and time.

SPDC is associated with the second order parametric processes (to be discussed in the following section) in non-linear crystals that is characterised by a real second order susceptibility tensor $\chi^{(2)}$. In this process, a high frequency pump (p) photon is spontaneously converted into two lower frequency (down-converted) photons with highly correlated position, the momenta and temporal components governed by conservation laws known as the phase matching conditions.

3.1.1 Phase matching

In the SPDC process a high frequency pump photon excites polarisation dipoles within the material resulting in random emissions of photon pairs with lower frequencies (down-converted), subject to conservation laws. The photons impinging the material cause the molecules to populate of energy levels (virtual energy levels) permitted by the uncertainty principle, with a subsequent depopulation from the excited states back to their original state after a time interval proportional to the energy difference. The depopulation causes fluorescent scattering of the entangled pair. Since no energy is dissipated nor transferred by the material onto the photons, the properties of both the input photon and material are conserved. For an emission of photons pairs, the following phase matching conditions must be satisfied,

$$\omega_p = \omega_s + \omega_i, \tag{3.1}$$

$$\mathbf{k}_p = \mathbf{k}_s + \mathbf{k}_i, \tag{3.2}$$
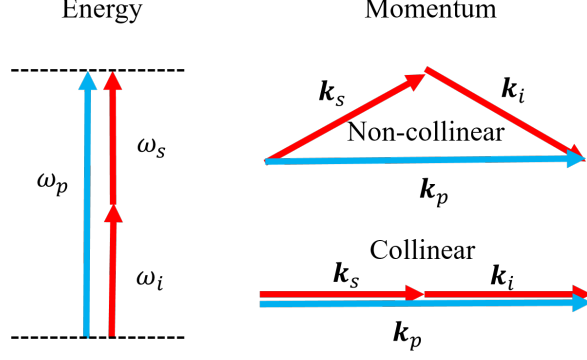
Figure 3-2: Phase matching conditions for the pump photon (p) and the entangled signal (s) and idler (i) photons spontaneously emitted by the non-linear crystal. The energy (ω) and momentum ($\mathbf{k}$) are conserved by the process. The Phase matching conditions allow for the non-collinear and collinear emission of photons.

where $\omega_p, \omega_s, \omega_i$ and $\mathbf{k}_p, \mathbf{k}_s \mathbf{k}_i$ are the frequency and wave vectors of the pump photon and down-converted signal and idler photon pairs, receptively. Accordingly, the frequency and total momentum of the down-converted photons must add up to that of the pump photon. Consequently, the total orbital angular momentum of the system is also conserved in the process [20] enabling OAM correlations between the down-converted pair.

The phase matching conditions can produce a collinear or non-collinear system of photon pairs (see Fig. 3-2). In the collinear system, the entangled photons travel in the same direction and in the non-collinear system, they move in a divergent manner. Furthermore, SPDC processes are mainly categorised as Type-0, Type-I and Type-II. In Type-0, the down-converted photons have the degenerate polarisations equivalent to that of the pump. Type-I down-converted photon pairs have degenerate polarisation but orthogonal to the pump photon. On the contrary Type-II produces photon pairs with orthogonal polarisations. To generate our OAM entagled photons we have chosen to use type Type-I phase matching.

3.1.2 SPDC quantum state

For a collinear Gaussian pump, the quantum state of the SPDC output is [79, 80]

$$|\psi\rangle_{SPDC} = \int \frac{d^2q_s}{2\pi} \frac{dq_i^2}{2\pi} \Phi(\mathbf{q}_s - \mathbf{q}_i) a_s^\dagger(\mathbf{q}_s) a_i^\dagger(\mathbf{q}_i) |0\rangle |0\rangle, \tag{3.3}$$

where $\mathbf{q}_p$, $\mathbf{q}_s$ and $\mathbf{q}_i$ are the transverse components of the wave-vectors $\mathbf{k}_p$, $\mathbf{k}_s$ and $\mathbf{k}_i$, respectively. Here $a_{s,i}^\dagger(\mathbf{q}_{s,i})$ are the creation operators, $|0\rangle$ represents a vacuum state and $\Phi(\mathbf{q}_s - \mathbf{q}_i)$ represents the phase matching function written as [80]

$$\Phi(\mathbf{q}_s - \mathbf{q}_i) = \sqrt{\frac{2L}{\pi^2 k_p}} \mathcal{E}_p(\mathbf{q}_s + \mathbf{q}_i) \times \mathrm{sinc}\left(\frac{\Delta k L}{2}\right) \times e^{-i\frac{\Delta k L}{2}}. \tag{3.4}$$

Here $\Delta k = \frac{|\mathbf{q}_s - \mathbf{q}_i|^2}{2k_p}$ is the phase mismatch which is zero when perfect phase matching is achieved. The function $\mathcal{E}_p(\mathbf{q})$ is the Fourier transform of

$$E(\mathbf{r}) = \sqrt{\frac{2}{\pi w_p^2}} e^{-\frac{r^2}{w_p}}, \tag{3.5}$$

a Gaussian profile of the pump photons with a beam diameter w_p at the interface of the crystal. In principle the spatial mode of the pump beam can be tailored as desired. We chose a Gaussian beam since this is relevant to our experiment.

The SPDC state, $|\psi\rangle_{SPDC}$, in Eq. (3.3) can be decomposed using any complete orthonormal mode set. Since OAM eigenmodes form a complete orthonormal basis and are cylindrically symmetric, Eq. (3.3) can be decomposed as

$$|\psi\rangle_{spdc} = \sum_{\ell_s p_s \ell_i p_i} c_{\ell_s p_s}^{\ell_i p_i} |\ell_s, p_s\rangle |\ell_i, p_i\rangle, \tag{3.6}$$

where ℓ represent the topological charge (OAM) and p represents the radial index of the photon. The state $|\ell, p\rangle = \int d^2q LG_{\ell,p}(\mathbf{q}) a^\dagger |0\rangle$ is the quantum state upon quantisation of the Laguerre-Gaussian basis functions $LG_{\ell,p}(\mathbf{q})$ written in the spatial

frequency domain. The probability amplitudes are calculated from

$$c_{\ell_s p_s}^{\ell_i p_i} \propto \int d^2 q_s d^2 q_i \big(LG_{\ell_s,p_s}(\mathbf{q}_s)\big)^* \big(LG_{\ell_i,p_i}(\mathbf{q}_i)\big)^* \Phi(\mathbf{q}_s - \mathbf{q}_i), \qquad (3.7)$$

where $|c_{\ell_s p_s}^{\ell_i p_i}|$ is the probability of finding the signal and idler photons in the state $|\ell_s, p_s\rangle$ and $|\ell_i, p_i\rangle$, respectively. Note, that the conservation of momentum also conditions the OAM of the systems, therefore

$$\ell_p = \ell_s + \ell_i. \qquad (3.8)$$

Under perfect phase matching conditions, the signal and idler photons have equal but oppositely charged OAM and therefore $\ell_s = -\ell_i = \ell$ due to the OAM of the Gaussian pump ($\ell_p = 0$). In the collinear system $\mathbf{q}_s - \mathbf{q}_i = 0$ phase matching function (Φ) is only described by the pump beam profile $\mathcal{E}_p$. Applying these conditions and converting to the cylindrical coordinates, Eq. (3.7) becomes

$$c_{|\ell|} \propto \int_0^\infty r dr \int_0^{2\pi} d\phi \big(LG_{\ell_s}(r, \phi)\big)^* \big(LG_{\ell_i}(r, \phi)\big)^* E(r). \qquad (3.9)$$

Here r and ϕ represent the radial and azimuthal coordinates respectively. Noting this and only considering the OAM DoF ($p_i, p_s = 0$) , Eq. (3.6) can be written in the following compact form

$$|\psi\rangle_{SPDC} = \sum_\ell c_{|\ell|} |\ell\rangle_s |-\ell\rangle_i . \qquad (3.10)$$

Here $c_{|\ell|}$ is found from Eq. (3.7). We will employ Eq. (3.10) for the description the quantum state of the SPDC process in the OAM basis. Experimentally, the probabilities, $c_{|\ell|}$, are determined from coincidence counts; a simultaneous detection of photon pairs at spatially separated detectors. The distributions rely on the characteristics of the SPDC process (e.g phase matching) and the efficiency of the detection system. These properties can be studied through a charactrisation of the spiral bandwidth of the system [81].
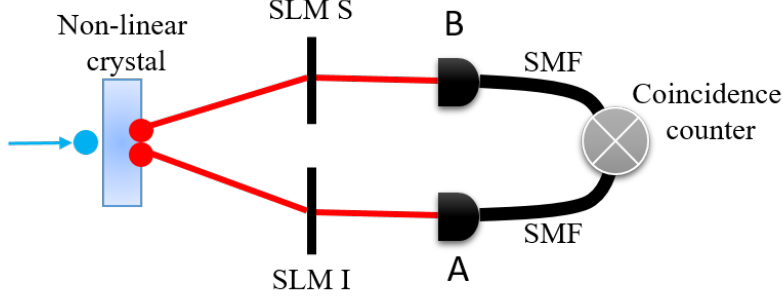
Figure 3-3: Entanglement set-up schematic. An entangled photon pair is produced from an SPDC source. The photons are spatially separated and OAM states are post-selected states with the combination of the SLM and single mode fibers (SMF). Simultaneous photon detections are registered as coincidence counts.

3.1.3 Spiral bandwidth

The OAM probability distributions $|c_{|\ell|}|^2$ rely on the conditions at the source [82] and the effects of the measuring apparatus [81]. It is important to be able to isolate the effects of the two contributions for an effective characterisation of an entanglement system. This can be achieved by using the spiral-bandwidth of the mode distribution. We associate the spiral band width with the full width half maximum (FWHM) of the $|c_{|\ell|}|^2$ distribution. In this way the spiral band width is a measure of the number of modes with strong correlations. This depends on the SPDC generated modes and the modes that the systems is able to detect.

The generated spiral-bandwidth defines the spectrum of modes that are produced by the SPDC process. Significantly, this depends on the phase matching conditions and the waist thus affecting the maximum number of modes that are accessible upon detection [80,83]. Consequently, this imposes limits on the number of modes that can be detected by the measurement apparatus.

Experimentally, holographic techniques with SLMs are used to measure spatial modes from the SPDC source (See Fig. 3-3 for a schematic.). The conjugate of the probe OAM modes ($|\ell\rangle$ and $|-\ell\rangle$) would be encoded on the spatial light modulator (SLMs) A and B, respectively.

We modeled the probabilities according to Eq. (3.9) by varying the ratio ($\gamma = \frac{w_p}{w_{s,i}}$)
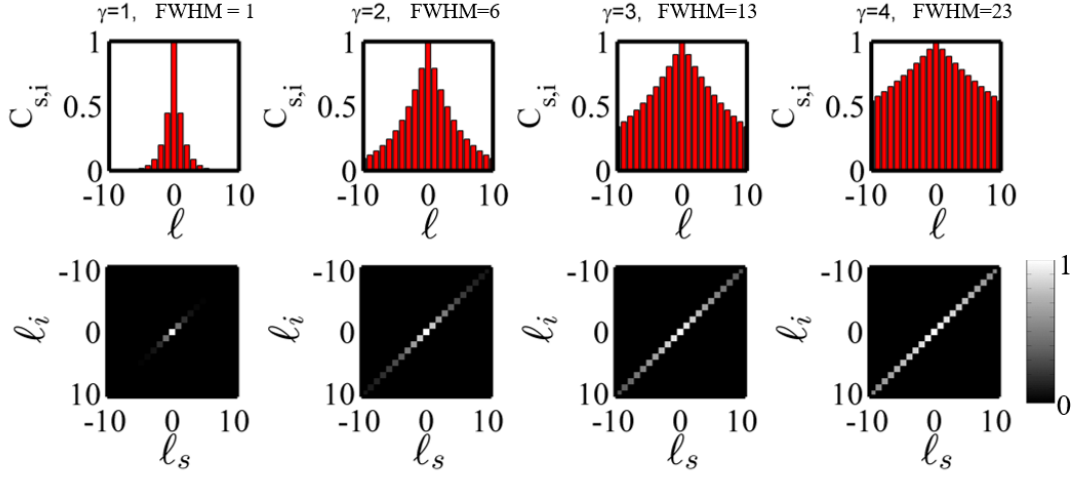
Figure 3-4: Simulated coincidence counts $(C_{s,i})$ vs the OAM modes (ℓ) with a variation of γ, the pump and back projected beam waist ratio, ranging from 1 to 4

.
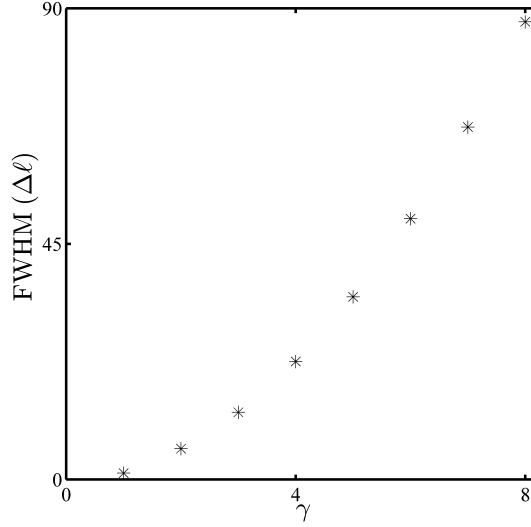
Figure 3-5: FWHM vs γ. FWHM denotes the full-width-half-maximum of each photon distribution (number of usable modes) and γ is ratio of the pump and back-projected beam waist at the SLM.

of the waists pump (w_p) and the LG modes encoded hologram $(w_{s,i})$ in Fig. 3-4 plotted as bar graphs and and below as density plots. Significantly, the spiral bandwidth, which we take as the FWHM of the count distribution increases with the size of the pump beam waist; clearly observed in Fig. 3-5. That is, more modes become strongly correlated with the increase in the pump size relative to that of the encoded waist

41
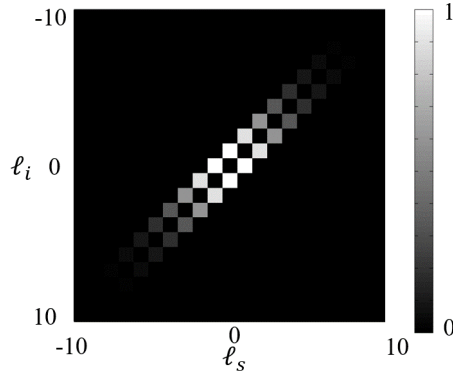
Figure 3-6: A simulation of the effect of pump shaping on the measured SPDC OAM spectrum which can also be predicated by back projection [85]. A pump with the mode function $LG_{1,0} + LG_{-1,0}$ is decomposed in the LG spectrum. The labels ℓ_i and ℓ_s represent the topological charge (OAM) in the idler and signal photon, respectively

.

of the mode function. This increase comes at the cost of losses in the count rate of the photons [80, 81]. To characterise the effects of the system on the SPDC state we adopt Klyshko's advanced wave model using back-projection [84].

3.1.4 Back-projection

The post selection on the entangled photons performed by the SLMs can be mimicked using back-projection alignment to characterise the effects of the apparatus on the SPDC state. The scheme exploits the retrodictive advance wave model proposed by Klyshko [84]. In the Klyshko picture, the probability of detecting a photon at detector A and B is equivalent to treating the entanglement system as though a photon registered at detector detected A travels back in time to the crystal and is reflect onto the path leading to detector B. This can be used to isolate the effects of the experimental apparatus from the nonlinear crystal using classical optics by replacing one of the detectors and the nonlinear crystal with laser and mirror, receptively.

This scheme has proven useful in ghost imaging experiments [86] where the two photon imaging experiment is simulated using a single photon in the advanced wave picture. Another interesting application is in quantum state engineering where the effects of pump shaping on the SPDC state can be investigated with back-projection
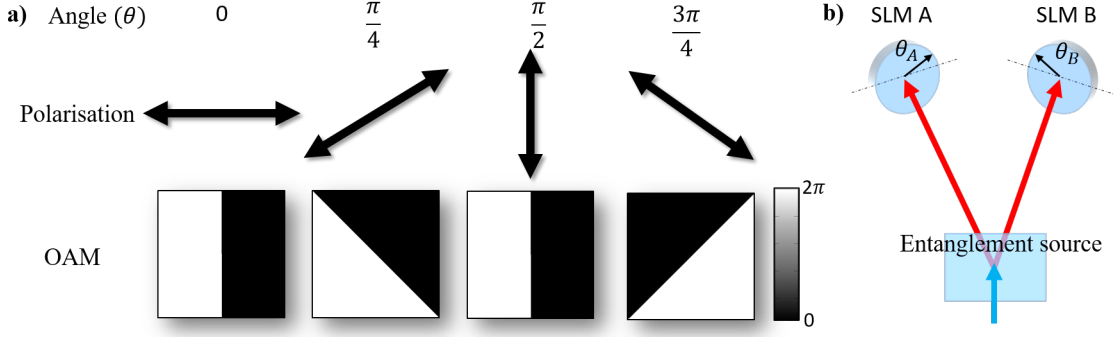
Figure 3-7: (a) Analogy between the angles of a polariser and the orientations of holograms for OAM superposition states given by Eq. (3.11), for $\ell = 1$. (b) An illustration of two SLMs with holograms similar oriented at angles θ_A and θ_B respectively. Analogous to performing measurements with polarisers orientated at different angles on entangled photons.

[85]. For example by preparing a pump photon described with a superposition of the LG modes. e.g $LG_{1,0} + LG_{-1,0}$. This can also be predicted by the general form of Eq. (3.9). We present the simulated correlations in Fig. 3-6.

We use back-projection to to align and optimise the performance of our experimental system (to be presented in the Experimental section).

3.1.5 Bell inequality violation with OAM

A method developed for locality tests between spatially separated bi-photon systems is the demonstration of a Bell-like inequaltiy [12] violation. In 1969 Clauser, Horne, Shimony and Holt (CHSH) formulated an alternative version of the Bell inequalities, relevant for an experimental application [87]. A series of demonstrations soon followed with reports of convincing evidence of the CHSH-Bell inequality violation using polarisation entangled photons generated from cascade atomic decays in calcium [88, 89], however, it was Aspect et al. [14, 15, 90] who reported more convincing evidence of the CHSH-Bell inequality violation. Unfortunately, atomic cascade methods made photon capturing difficult due to the random emission of photons at full solid angles. More interest went towards finding more efficient ways of producing entangled photons. There have been multiple reports of CHSH inequality violation with polarisation qubits using SPDC. [16, 74–76]. These experiments required corre-

lated polarisation measurements between superposition states of the two entangled photons. For example, for circularly polarised entangled photons, this would involve the use of linear polarisers as analysers. Rotating a polariser from vertical to horizontal is a projections onto superposition states along the equator of the Poincar*texte* sphere. Just as with polarisation, we measure correlations between superposition OAM eigenstates for a particular OAM subspace by preparing holograms on SLMs described by [22]

$$|\theta\rangle = \frac{1}{\sqrt{2}}(|\ell\rangle + e^{2\theta} \, |-\ell\rangle), \tag{3.11}$$

taking the form of a phase step. The angle θ describes the rotation of the phase step which is analogous to the rotation of polarisation states (see Fig. 3-7). To determine the correlations, consider two photons produced in the from the SPDC state similar to Eq. (3.10) in arm A and B, entangled in OAM. By post selecting on coincidence for a particular ℓ (or restricting measurements to a particular ℓ subspace), Eq. (3.10) becomes

$$|\psi\rangle_{AB} = \frac{1}{\sqrt{2}}(|\ell\rangle_A \, |-\ell\rangle_B + |\ell\rangle_A \, |-\ell\rangle_B). \tag{3.12}$$

Let SLM A and B be placed in the paths of the entangled photons and encoded with holograms corresponding to Eq. (3.11), respectively. SLM A is encoded with a hologram $|\theta_A\rangle$ similarly SLM B is encoded with a hologram corresponding to the state $|\theta_B\rangle$. The probability of observing a coincidence based on the rotation angle *theta* selected in arm A or B is

$$P(\theta_A, \theta_B) = |\langle\theta_A| \, \langle\theta_B|\psi\rangle_{AB}|^2 = \cos^2(\theta_A - \theta_B). \tag{3.13}$$

The coincidence counts are highest when the detection systems are orientated at 0 and π integer multiples relative to each other. During measurements, the angle of one analyser is usually fixed at some angle (θ_A) and the other (θ_B) is rotated while the coincidence rates are measured. We adopt the CHSH variation of the Bell inequity given by [87],

$$S = |E(\theta_A, \theta_B) - E(\theta_A, \theta'_B) + E(\theta'_A, \theta'_B) + E(\theta'_A, \theta_B)| \leq 2, \tag{3.14}$$

where $E(\theta_A, \theta_B)$, is the correlations between the measurements in arm A and B when the holograms on the SLMs are encoded with holograms corresponding to $|\theta_A\rangle$ and $|\theta_B\rangle$. S is maximally violated when $\theta_A = 0, \theta_B = \frac{\pi}{8\ell}, \theta'_A = \frac{\pi}{4\ell}$ and $\theta'_B = \frac{3\pi}{8\ell}$.

Experimentally, the correlations can be calculated using the measured coincidence counts $C(\theta_A, \theta_B)$ as follows

$$E(\theta_A, \theta_B) = \frac{C(\theta_A, \theta_B) + C(\theta_A + \frac{\pi}{2\ell}, \theta_B + \frac{\pi}{2\ell}) - C(\theta_A + \frac{\pi}{2\ell}, \theta_B) - C(\theta_A, \theta_B + \frac{\pi}{2\ell})}{C(\theta_A, \theta_B) + C(\theta_A + \frac{\pi}{2\ell}, \theta_B + \frac{\pi}{2\ell}) + C(\theta_A + \frac{\pi}{2\ell}, \theta_B) + C(\theta_A, \theta_B + \frac{\pi}{2\ell})},$$
$$(3.15)$$

The system is considered to be quantum entangled, if it violates the CHSH Bell's inequality ($|S| > 2$) and bounded above by $2\sqrt{2}$ [91] . Satisfying these conditions implies that the two subsystems are non-separable and that they exhibit non-local interactions and confirm the entanglement of the system [89]. Conversely, the system is separable.

3.2   Experimental set-up

3.2.1   SPDC characterisation

Here we present the experimental procedure used to characterise the down-converted field. In our experiment we used a $2 \times 2 \times 1$ mm^3 periodically-poled-potassium-titanyl-phosphate (PPKTP) non-linear crystal as our entangled photon source. The crystal is designed to achieve quasi-phase-matching by alternating the orientations of birefringent KTP layers with a period of Λ (see Fig. 3-8(a)). Λ is chosen such that it counteracts phase mismatching, Δk, found in the phase-matching term of Eq. (3.4). Since the birefringence of the KTP crystal varies with temperature, then $\Delta k = \frac{\omega}{c} \frac{|n_s(T,\omega) - n_i(T,\omega)|}{2k_p}$ where $n_{s,i}(T, \omega)$ are the temperature (T) dependent refractive indexes of the signal and idler photons. Therefore perfect phase matching could only be achieved at a temperature where the refractive indices are degenerate. Note that refractive index also depended on the wavelength of the pump photon.

A schematic of the experimental set-up that was used to characterise the down-converted field is shown in Fig. 3-8(b). We used a Coherent Cube diode laser with
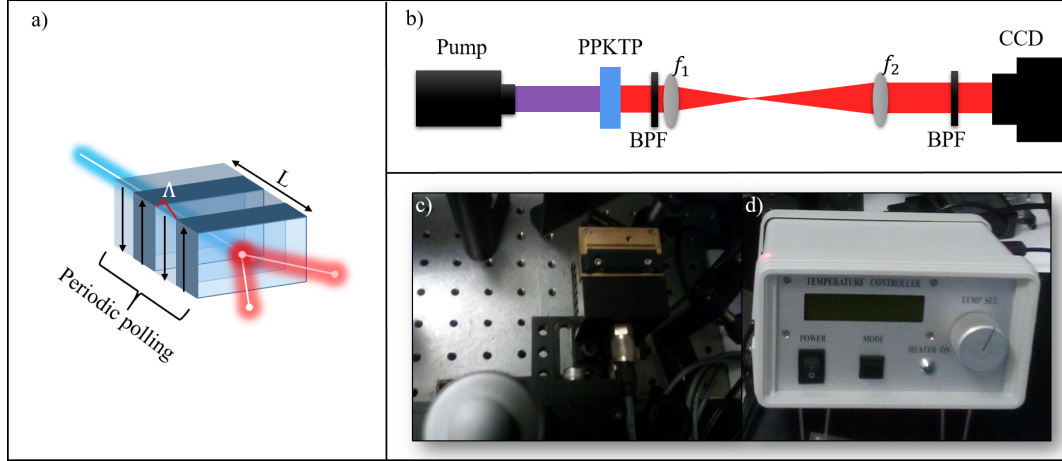
Figure 3-8: (a) An illustration of periodic-polling in quasi phase-matched crystals. Birefringent crystal domains (layers) are alternated for a crystal with a give length (L). The period of each successive alternation is given by Λ. b) Experimental set-up used for imaging the down-converted photons from the periodically-poled-potassium-titanyl-phosphate (PPKTP) crystal. The crystal plane was imaged into a charge coupled device (CCD) using lenses $f_1 = 300$ mm and $f_2 = 150$ mm in a 4f system. The PPKTP crystal was placed on (c) a heat oven which was regulated with (d) temperature controller for phase matching.

a Gaussian profile, having a nominal wavelength of 405 nm and horizontal polarised. The birefringence of PPKTP resulted in the down-converted photons having a vertical state of polarisation – indicative of Type-I phase matching. The laser was focused onto the PPKTP crystal placed on heat oven shown in Fig. 3-8(c) which we used as a means of controlling the phase matching conditions of our temperature dependent crystal. The down-converted field was demagnified from the crystal plane into the CCD camera which was used to take images of the intensity profiles while the room kept dark to reduce noise levels. Band-pass filters with a 10 nm bandwidth were used to filter the 810 nm down-converted photons: one was placed after the crystal and another at the camera.

A transition of the down-converted light from a non-collinear to a non-collinear geometry is shown in Fig. 3-9, resulting from an increase in the oven temperature. The down-converted field is concentrated at the edges with a ring like geometry when the temperature was set to $43°C$ and converged with increase in temperature indicating that the wave-vectors of the signal and idler morph from a non-collinear to a collinear geometry (see Fig. 3-2 for the orientation of the wave-vectors). The areas
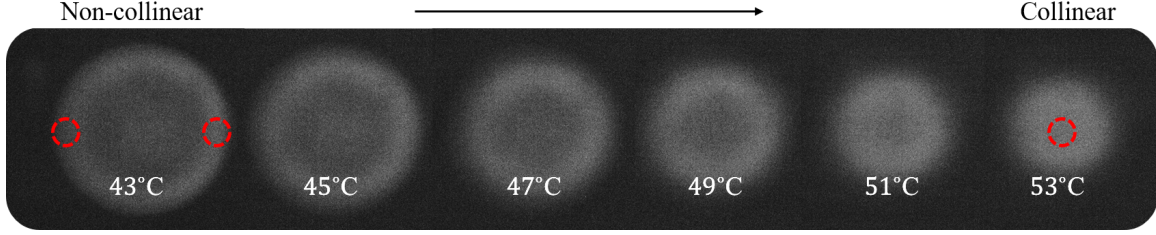
Figure 3-9: Experimental intensity profiles of the down-conversion cone with temperature change.

with red circles represent the positions where correlated photons are most likely to be found with their respective geometries (collinear and non-collinear).

3.2.2 Back-projection and down-conversion alignment

Before performing measurements on the down-converted photons the system had to be aligned was aligned perfectly and then charaterised. To achieve this the method back projection was. The experiment was performed in non-collinear mode with the temperature of the crystal maintained at $45°C$. A D-shaped mirror was used to separate the photons emerging from the down converted cone into arm A (signal) and arm B (idler), respectively. The system to be prepare is illustrated in Fig. 3-10(a). However, it was more practical to build the system in back-projection first as in Fig. 3-10(b).

Firstly, a HeNe laser (633 nm) beam was coupled to SMF A for (filtering the Gaussian mode) and attenuated to avoid saturating the APD. Treating the laser source as though it were a photon traveling back in time, it was imaged from SMF A onto SLM A with lenses f_4 (2 mm) and f_3 (500 mm) and then onto the crystal plane (mirror) with lenses f_2 (1000 mm) and f_1 (300 mm). This marks the path to be taken by the signal photon. The beam reflecting off the mirror or equivalently, the crystal plane, was used to replicate the same system leading to detector B, marking the path of the idler photon. The coupling into detector B was improved and enabling for the simulation some of the quantum measures using laser light.

Next, the system was prepared for correlation measurements with down-converted photons by replacing the mirror with the crystal and the HeNe laser with detector
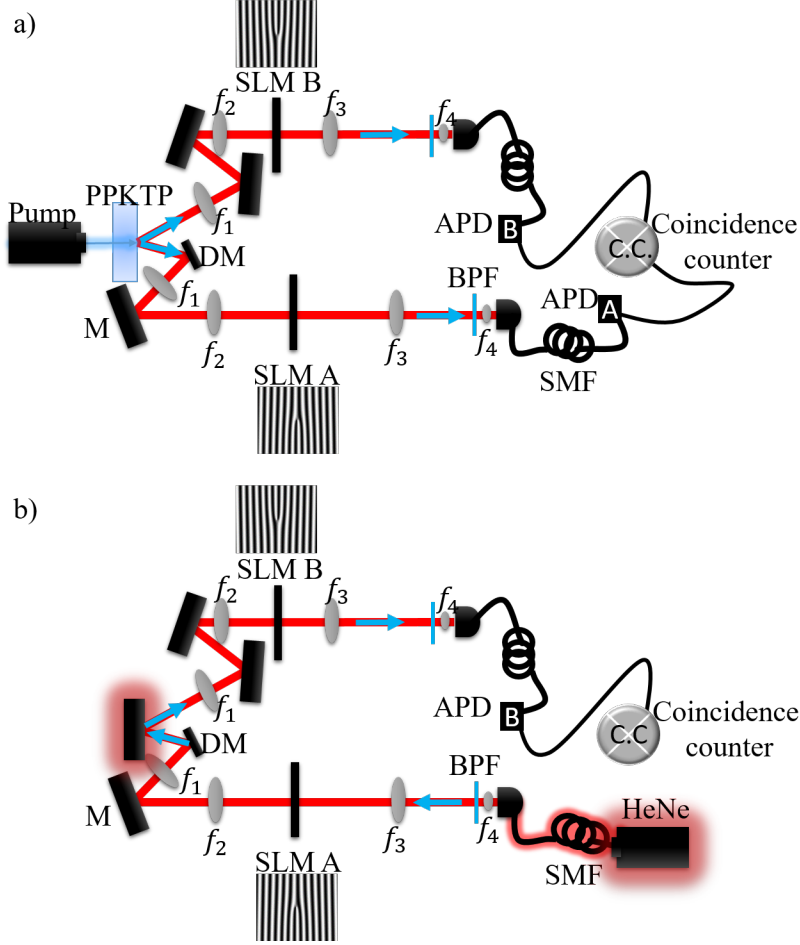
Figure 3-10: (a)Experimental setup for non-collinear SPDC with the entangled photon pair separated by a D-shaped mirror (DM). A 405 nm Coherent Cube diode laser was as a pump photon source (Pump). The emerging signal and idler photons were directed onto paths leading to detector A and B. We treated the crystal, spatial light modulators (SLM) and single mode fibers (SMF) as image planes. As such, the plane of the crystal was imaged onto the SLMs with lenses (f_1=300 mm) and f_2=1000 mm) and into the single mode fibers (SMF) with lenses f_3=500 mm and f_3=2 mm.The 810 nm photons were filtered with band pass filters (BPF) and collected using SMFs that were coupled to avalanche photon diodes (APD) in arm A and B. The count between the two detectors were conditioned on coincidence. Our APDs were Perkin-Elmer single photon counting modules (SPCM) with a coincidence window of 25 ns. (b) Back projection used to charactorise the system. We replaced the crystal with a mirror and detector A with a helium-neon (HeNe) laser. The alignment procedure is detailed in the text.

A. The 810 nm photons were filtered using band pass filters (BPF) (or interference filters) having a 10 nm bandwidth. The SMF were used to collected once they were modulated by the SLMs. These were fed into the avalanche photo diodes (APD) in arm A and B connected in coincidence. The APDs converted each photon into an

avalanche current using Transistor-Transistor-Logic (TTL) signals that translated the signals into photon counts with a 6602 PCI/PXI counting card. A gating (grace) time of 25 ns was set between the detectors. Overlapping photon signals within each gating event were considered as a coincidence events. The photon counting was performed over a time interval (5 s), much larger than the gating time.

3.3 Results and discussion

3.3.1 Spiral Bandwidth

We present and compare the results of the spiral bandwidth measurements obtained from measurements with the experimental set-ups for back-projection Fig. 3-10(b) and down-conversion Fig. 3-10(a). SLM A and B were used to scan through OAM modes ranging from $\ell = -10$ to $\ell = 10$ with each measurement recorded with a 5s integration time, significantly above the time resolution of the detectors (25 ns).

The results are presented in Fig. 3-11. In Fig. 3-11(a) and Fig. 3-11(b) we present the phase only decomposition in back-projection and down-conversion, respectively. That is we encode fork holograms corresponding to the azimuthal phase mode functions, $e^{i\ell\phi}$. The density plots (matrix plots) are anti-diagonal, showing maximal counts when $\ell_s + \ell_i = 0$. This is consistent with the conservation of OAM in the SPDC process [20]. The bar plots are the corresponding anti-diagonal elements of the matrix plots. These are the experimental probabilities, $|c_\ell|^2$, corresponding to Eq. (3.9). The full-width-half-maximum (FWHM) was used as figure of merit for the number of highly correlated modes ($\Delta\ell$) detectable by the system. The back projection system enabled for the use of $\Delta\ell \approx 6$ modes while in down-conversion we obtained $\Delta\ell \approx 8$ the discrepancies may arise due to the differences in mode quality after the SLM (SLMs are calibrated for a particular wavelength).

Further, more a decomposition with the LG basis was performed by encoding the amplitude and phase of each OAM mode and set the radial modes (p) to 0. The results are presented in Fig. 3-11. The anti-diagonal matrix confirms the OAM conservation,
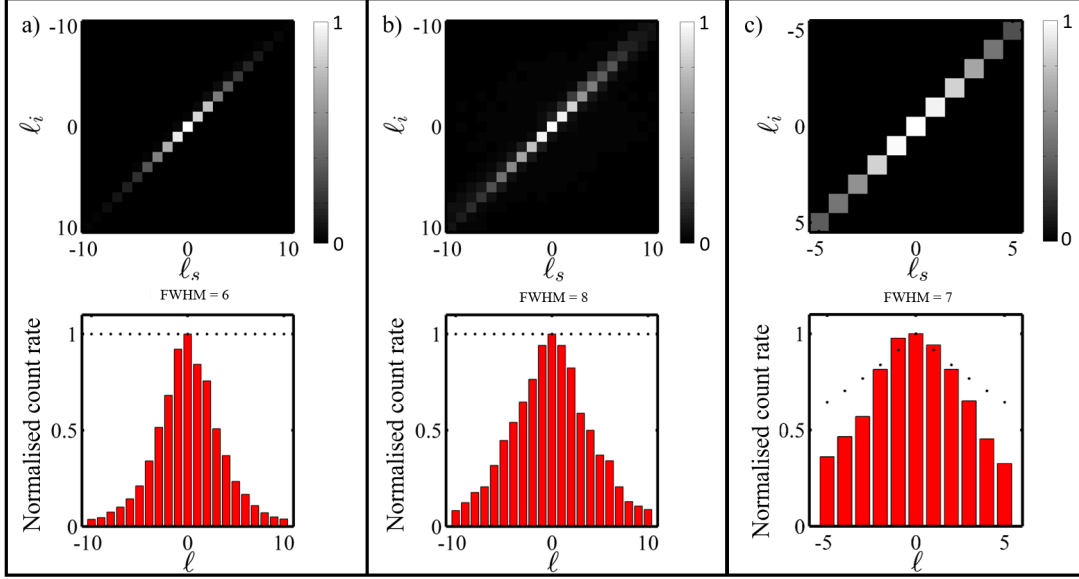
Figure 3-11: Experimental and theoretical (points) spiral bandwidth measurements for the (a) down-converted photons, (b) back-projection beam using a phase only decomposition (no radial dependence of the mode functions encoded on the SLM) and (c) an LG mode decomposition of the down-conversion. The matrix plots represent measurements taken for different OAM states corresponding to ℓ (OAM topological charge), with the diagonal entries presented in the bar plots. The points in the bar plot represent the theoretical prediction. It is important to note that in back projection, the counts where collected from detector B while coincidences between detector A and B where used for the down-conversion. FWHM denotes the full-width-half-maximum of each photon distribution or the number of highly correlated modes.

as expected. The distribution of ℓ is maximal for $\ell = 0$ also decreases with increasing OAM. The predicted FWHM is $\Delta\ell = 8$ and we it ours to be $\Delta\ell \approx 7$.

3.3.2 Bell inequality measurement

To show that the PPKTP crystal produces OAM entangled photons, correlated measurements with OAM superposition states in the $|\ell = 1|$ subspace were taken to demonstrated a violation of the Bell inequality as described in Sec. 3.1.5. SLM A was encoded with a phase aperture orientated at an angle θ_A while the another was encoded on SLM B, and rotated. The phase apertures are illustrated in Fig. 3-7. Remember that the phase apertures corresponding to superpositions of OAM described in Eq. (3.11).
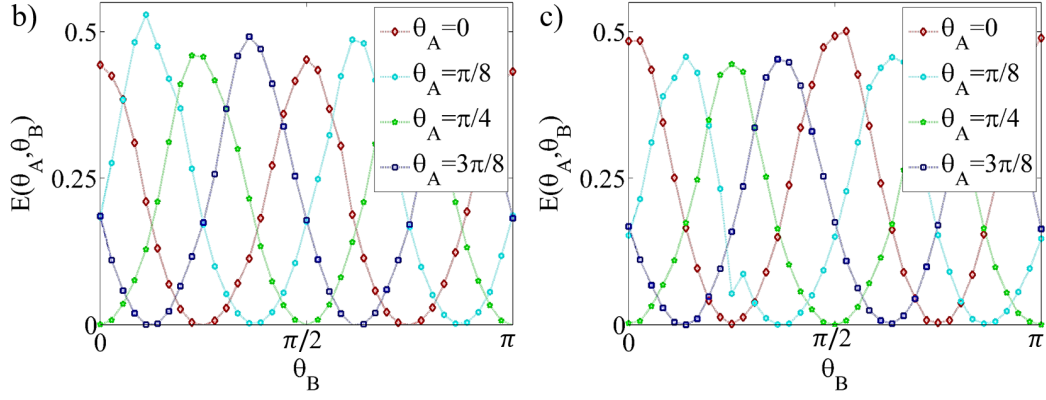
Figure 3-12: CHSH-Bell analysis of the (a) back projected He-Ne 633 nm laser beam and (b) 810 nm SPDC source.

The measured correlations for the back projection and down-converted experiment are presented in Fig. 3-12. It is necessary to point out that the back-projection results only provide an indication of the maximal observable correlations although it is performed as a prepare and measure scheme. The sinusoidal behavior is predicted in Eq. (3.13) from the overlap between the phase apertures (for SLM and B) and the OAM Bell state. Such correlations are only observed in entangled systems and cannot be accounted for by local hidden variable theories [22, 89]. Note that this implication holds for the down-converted photons only. We calculated the S parameter using Eq. (3.14) to confirm the entanglement of photons emitted form the PPKTP crystal. We obtained $S = 2.80 \pm 0.03$ for the back-projected laser beam and $S = 2.66 \pm 0.04$ down-converted photons. Therefore these results violate the Bell inequality ($S \leq 2$) by 20 and 16 standard deviations, respectively. The violation observed in the down-converted case confirms entanglement in the $|\ell| = 1$ OAM subspace. The discrepancy between the two result may have resulted due to misalignment since placing the crystal back to the position of the mirror after back-projection requires the system to be tuned back into the alignment again. For that reason the alignment does not stay the same.

3.3.3 Quantum state reconstruction

After confirming that system produces and detects OAM entangled photons that conserve the OAM of the pump photon, we reconstructed the density matrix in OAM subspaces, $|\ell| = 1, 2$.

The quantum state $|AB\rangle$ (Eq. (3.12) of a system can be represented by a density matrix, ρ_{AB}. In Chapter 2, we noted that ρ_{AB} is given by $\rho = |\psi_{AB}\rangle \langle \psi_{AB}|$. In the OAM basis of a two particle system, the state ψ_{AB} belongs to the tensor product of two Bloch spheres representing the state space of each photon in the entangled pair. The state-space is spanned by the following basis $\{|1\rangle |1\rangle, |1\rangle |-1\rangle, |-1\rangle |1\rangle, |-1\rangle |-1\rangle\}$ for a chosen ℓ. The entries of the matrix are given by

$$
\rho = \begin{bmatrix}
A_{1,1} & A_{1,2}e^{i\phi_{1,2}} & A_{1,3}e^{i\phi_{1,3}} & A_{1,4}e^{i\phi_{1,4}} \\
A_{2,1}e^{i\phi_{2,1}} & A_{2,2} & A_{2,3}e^{i\phi_{2,3}} & A_{2,4}e^{i\phi_{2,4}} \\
A_{3,1}e^{i\phi_{3,1}} & A_{3,2}e^{i\phi_{3,2}} & A_{3,3} & A_{3,4}e^{i\phi_{3,4}} \\
A_{4,1}e^{i\phi_{4,1}} & A_{4,2}e^{\phi_{4,2}} & A_{4,3}e^{i\phi_{4,3}} & A_{4,4}
\end{bmatrix},
\tag{3.16}
$$

where $A_{i,j}$ are the amplitudes and $\phi_{i,j}$ are the phases that make up the 16 matrix elements. The diagonal elements represent the probability of finding the system in one of the basis states. The amplitudes and phases can be determined from a set of measurements in the mutual unbiased basis of angular states given by $|\theta\rangle$ (Eq. (3.11)). The measurements comprise projections across the OAM eigenstates $|\ell\rangle, |-\ell\rangle$ and the superposition states $|\theta = 0\rangle, |\theta = \frac{\pi}{4}\rangle, |\theta = \frac{\pi}{2}\rangle$ and $|\theta = 3\frac{\pi}{4}\rangle$ defined in .

The experimental results are presented in Fig. 3-13 for the $\ell = 1, 2$ subspaces. From these results the density matrix is reconstructed using numerical techniques. The density matrix elements can be written in terms of the count rates obtained from measurements. This yields 36 coupled equations. We employ the procedure used in [92] to calculate the amplitudes and phases of the density matrix elements defined in Eq. (3.16) through a numerical procedure that predicts the amplitudes
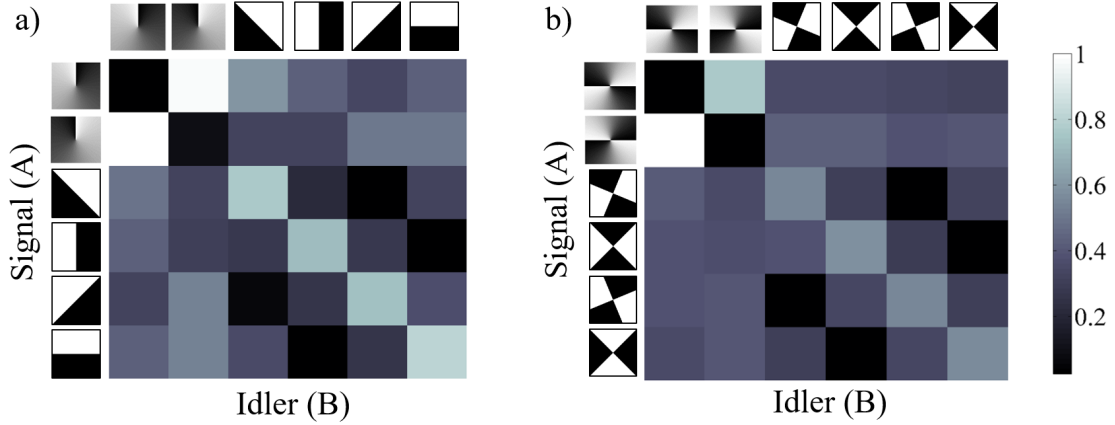
Figure 3-13: Normalised experimental full state tomography results for the (a) $|\ell| = 1$ and (b) $|\ell| = 2$ subspace where each of the holograms were encoded in arm A and B. It is from these results that the density matrix is computed.

and phases by minimising [93]

$$\chi^{(2)} = \sum_i^{N^2} \frac{(C_i^{(M)} - C_i^{(P)})^2}{C_i^{(P)}}, \tag{3.17}$$

where $C_i^{(M)}$ are the coincidence counts from measurements and the $C_i^{(P)}$ are predicted from the density matrix. $\chi^{(2)}$ is minimised on condition the density matrix yields positive eigenvalues.

In Fig. 3-14(a) and Fig. 3-14(a) we present the reconstructed real and imaginary parts of the density matrices for the $|\ell| = 1$ and $|\ell| = 2$ subspaces, respectively. To determine how well the matrix obtained from the experiment approximates a target state, we calculate its fidelity [94]

$$F = \mathrm{Tr}\left(\sqrt{\sqrt{\rho_t}\rho_e\sqrt{\rho_t}}\right)^2. \tag{3.18}$$

Here ρ_t is the density matrix representing a target state $|\psi\rangle = \frac{1}{\sqrt{2}}(|\ell\rangle_A |-\ell\rangle_B + |-\ell\rangle_A |\ell\rangle_B)$ and ρ_e is the experimentally reconstructed density matrix. If the matrices are identical then F=1, conversely F=0. We obtained fidelities of 0.92 ± 01 and 0.94 ± 01 for the $\ell = 1$ and $\ell = 2$ subspaces, respectively. These are close to 1 and
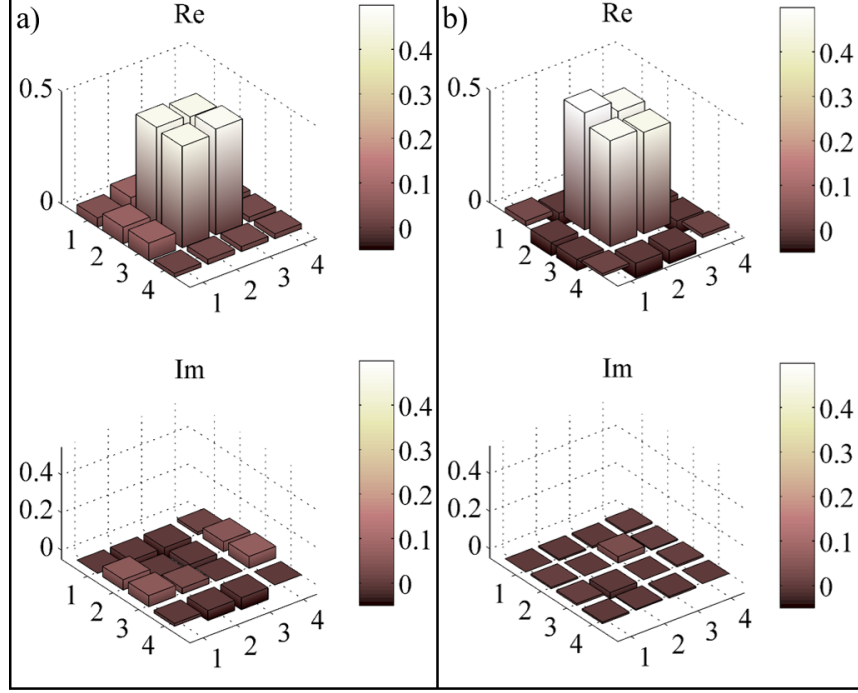
Figure 3-14: Experimentally measured real and imaginary parts of the density matrix for the post-selected (a) $|\ell| = 1$ and (b) $|\ell| = 2$ subspaces.

hence indicate that the reconstructed quantum states close to a maximally entangled Bell state.

Next, use a qualitative measure of entanglement, the concurrence [95]

$$\mathcal{C}(\rho) = \max\{0, \lambda_1 - \lambda_2 - \lambda_3 - \lambda_4\}, \tag{3.19}$$

to determine the level of entanglement in the system. Here the λ_i represent the eigenvalues of the matrix $\rho(A\rho A)$ in descending order with $A = \sigma_2 \otimes \sigma_2$, calculated from the Pauli operator $\sigma_2 = \begin{bmatrix} 0 & -i \\ i & 0 \end{bmatrix}$. If $\mathcal{C}(\rho) = 1$ then ρ represents an entangled sytem while on the contrary $\mathcal{C}(\rho) = 0$ would mean a quantum system represented by ρ is not entangled. Our measured concurrences are 0.88 ± 0.01 and 0.90 ± 0.02 for the $|\ell| = 1$ and $|\ell| = 2$ subspaces, respectively. Close the expected result for an entangled system of photons.

Finally we calculate the linear Entropy $(L = \frac{1}{4}(1 - Tr(\rho)))$ – a measure of the

quantum state's purity [92, 96]. For pure states the linear entropy is 0. In our experiment we measured entropies of $L = 0.095 \pm 0.003$ and $L = 0.063 \pm 0.001$ for the $\ell = 1$ and $\ell = 2$ subspaces, respectively. Our measured values are close to zero.

We point out that the measured fidelity, concurrence and linear entropy in the $|\ell| = 2$ subspace are higher than the $|\ell| = 1$. This may have resulted from misalignment or small temperature fluctuations which may affect the phase matching of the PPKTP crystal.

3.4 Conclusion

In this chapter we have developed the techniques required to generate and detected photons entanglement in the OAM DoF. We generated them using SPDC with a PP-KTP crystal. We have shown that temperature change affects its the phase matching conditions, enabling the down-converted photons to morph between a non-collinear and a collinear geometry. For the detection, we used SLMs coupled to single photon detectors with a SMF to perform projective measurements. Using back-projection, we assembled and aligned the system and thereafter introduced the down-converted photons. We measured the OAM spectrum and found that our PPKTP crystal produced photons pairs that conserved OAM. We tested for local hidden variables via a CHSHS-Bell inequality experiment and calculated the Bell parameter, S, from measurements with superpositions of OAM states. We measured $S = 2.66 \pm 0.04$ which violated the Bell inequality by 16 standard deviations. Such a violation means that the correlations between the entangled pairs cannot be explained by any local hidden variable theories. Lastly, we performed a tomography of the photon pairs and reconstructed the system's density matrix. From density matrix we measured the fidelities, concurrences and linear entropies which yielded results indicating that our PPKTP crystal produced entangled photons that can be described by a pure OAM Bell state. The confirmation of entanglement is important for the generation of hybrid-entanglement entangled states in the coupled OAM and polarisation DoFs. It was shown that hybrid entanglement can be generated from OAM entanglement [37]. We exploit this

in the following chapter in a quantum eraser experiment.

Chapter 4

Quantum eraser using hybrid entanglement

This work has in published in Ref. [97].

4.1 Introduction

Wave-particle duality is a salient feature of quantum mechanics and has primarily been observed through modern variations of Thomas Young's double slit experiments [98–102]. When the paths of the double slit are indistinguishable, multi-path interference results in fringes of high visibility (V) in the far-field, which is a characteristic trait of wave-like behavior. Conversely, if the paths are distinguishable (D), for example, through the use of which-path markers, the fringes disappear (particle behavior). The physical implications of this are embodied through the principle of complementarity [103], emphasizing the mutual exclusivity that exists between complimentary observables. The special case of $D = 0$ and $V = 1$ corresponds to a maximal observation of interference fringes while that of $D = 1$ and $V = 0$ corresponds to a full obtainment of the which-path information. Intriguingly, it is permitted to have partial visibility and partial distinguishability, where the result cannot be explained exclusively by a wave-like or particle-like interaction [104–107], and this may quantitatively be expressed through the following inequality: $V^2 + D^2 \leq 1$. Thus,

gaining knowledge of path information ($D \neq 0$), reduces the visibility of the fringes ($V < 1$). Interestingly, the path information can be erased with a complimentary projection with respect to the path markers of the double slit, reviving the interference fringes. Scully and co-authors [24, 108] proposed such a device, the quantum eraser, which is now ubiquitous in experimental verifications of the complementarity principle. For example, in the double slit experiment presented in [25], a polariser is used to recover the interference pattern that is lost due to path distinguishability with circular polarisers. By orienting a polariser in a diagonal position, the path information is erased. Numerous other experiments have been performed with photonic systems using double slits [9, 109], interferometers [26, 110–113], and in delayed-choice measurement schemes [26, 114, 115]. All these experiments have used physical paths to study the multi-path interference in the context of quantum erasers. Here we generalise the concept of "path", showing that it need not be a physical path in the sense of a route through space but an abstract "path" in any degree of freedom. We employ orbital angular momentum (OAM) as our "path" and use polarisation as the "which-path" marker. To test this we create hybrid entanglement between photons carrying spin and orbital angular momentum and show control of the fringe visibility through a generalised quantum eraser experiment: the OAM paths marked with polarization do not lead to interference, while introducing the eraser (polarizer) which projects the polarization of one of the entangled photons onto a complementary polarisation basis results in azimuthal fringes with high visibility. We perform this experiment in both the conventional quantum eraser and delayed-choice schemes, in both cases showing control of the nature of the photons, from particle (no visibility) to wave (full visibility). Our experimental results are in very good agreement with theory, offering a simple approach to illustrate the concept of path in quantum mechanics.
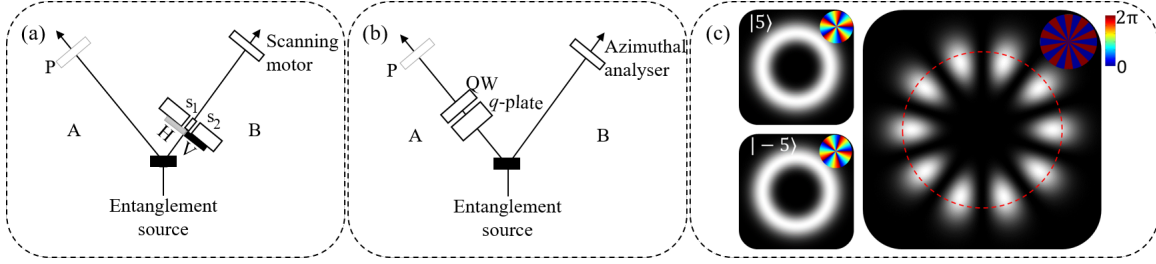
Figure 4-1: (a) Schematic of a quantum eraser that uses polarization entangled photons using a physical double slit as reported by Walborn *et al.* [25] is shown. The two slits (s_1, s_2) are marked with orthogonal horizontal (H) and vertical (V) linear polarizers to distinguish the two paths. The polarizer (P) in arm A acts as the eraser. (b) The proposed quantum eraser using geometric phase control to perform OAM-polarization conversion. The polarization control (P) of photon A sets the OAM interference of photon B. (c) An example of two independent OAM abstract paths ($|\ell = 5\rangle$ and $|-5\rangle$), and their superposition, $|5\rangle + |-5\rangle$, having 2ℓ azimuthal spatial fringes analogous to path interference fringes in the double slit experiment.

4.2 Theory

4.2.1 Revisiting the double-slit quantum eraser

It is instructive to revisit the concepts of the traditional quantum eraser experiment, illustrated in Fig. 4-1 (a), which we do here briefly for the benefit of the reader. Consider a photon traversing two unmarked slits, which can be represented by the following coherent superposition

$$|\Phi\rangle = \frac{1}{\sqrt{2}} \left(|\psi_1\rangle + |\psi_2\rangle \right), \tag{4.1}$$

where $|\psi_1\rangle$ and $|\psi_2\rangle$ are the non-orthogonal states upon traversing slit 1 and 2 (path 1 and path 2), respectively. The spatial probability distribution of the photon after the slits is given by $|\langle\Phi\rangle\Phi|^2$ where the interference pattern, a sign of the photon travelling through indistinguishable paths, emerges due to the cross terms $\langle\psi_i\rangle\psi_j$ for $i \neq j$. However, the fringes disappear when the paths are marked (distinguishable), for example, with orthogonal polarizers which, we assume are oriented along the horizontal (H) and vertical axis (V)

$$|\Phi\rangle = \frac{1}{\sqrt{2}} \left(|\psi_1\rangle |H\rangle + |\psi_2\rangle |V\rangle \right). \tag{4.2}$$

59

Now, the cross terms vanish and $|\langle \Phi \rangle \Phi|^2 = \sum_i |\langle \psi_i \rangle \psi_i|^2/2$. Equation 4.2 represent a general state of entangled spatial and polarization degrees of freedom of a single photon. An identical representation can be extended to a two-photon case using entanglement. To illustrate this, consider the schematic for a system that produces polarization entangled photons given by the following state,

$$|\Phi\rangle_{AB} = \frac{1}{\sqrt{2}} \left(|H\rangle_A |V\rangle_B + |V\rangle_A |H\rangle_B \right), \tag{4.3}$$

where the subscripts A and B label the entangled photons. Inserting a double slit in the path of photon B, with each slit (s_1 and s_2) marked with orthogonal linear polarizers yields

$$|\Phi'\rangle_{AB} = \frac{1}{\sqrt{2}} \left(|H\rangle_A |s_1\rangle_B + |V\rangle_A |s_2\rangle_B \right). \tag{4.4}$$

Equation (4.4) is a hybrid entangled state where the polarization of photon A is entangled with the slit (path) traversed by photon B. For example, measuring the state $|H\rangle$ for photon A means that photon B traverses through slit s_1, hence no interference fringes will be observed in the far-field of the double slit since there is path information in the system. However if photon A is projected onto the complimentary diagonal basis, $\{|D\rangle, |A\rangle\}$, where $|D\rangle = (|H\rangle + |V\rangle)/\sqrt{2}$ and $|A\rangle = (|H\rangle - |V\rangle)/\sqrt{2}$ are the diagonal and anti-diagonal states respectively, then the following projections hold

$$|\Phi'\rangle_{AB} \xrightarrow{\hat{D}_A} \frac{1}{\sqrt{2}} \left(|D\rangle_A \left(|s_1\rangle_B + |s_2\rangle_B \right) \right), \tag{4.5}$$

$$|\Phi'\rangle_{AB} \xrightarrow{\hat{A}_A} \frac{1}{\sqrt{2}} \left(|A\rangle_A \left(|s_1\rangle_B - |s_2\rangle_B \right) \right), \tag{4.6}$$

where $\hat{D}_A$ and $\hat{A}_A$ are projection operators associated with the states $|D\rangle$ and $|A\rangle$, acting on photon A. Thus the projections of photon A onto complimentary polarization states collapses photon B into a coherent superposition of the two paths, consequently recovering the interference pattern. This means that the which-way path information of photon B has been erased.

4.2.2 Engineering hybrid OAM-polarisation entanglement for the OAM based quantum eraser

Now we exchange the notion of path or slit, for that of orbital angular momentum (OAM). Photons carrying OAM [28,116] have attracted great interest in both classical and quantum studies [29,31,32]. OAM modes possess a transverse spatial distribution characterized by an azimuthal phase of $e^{i\ell\phi}$ such that each photon has an angular momentum of $\pm\ell\hbar$ where the integer ℓ represents the twist or helicity of the phase profile. Since OAM states of differing ℓ are orthogonal, entanglement may be expressed in this basis where each photon OAM subspace is spanned by $\mathcal{H}_2 = \{|\ell\rangle, |-\ell\rangle\}$. The detected distribution (intensity distribution in classical light) of the photons is symmetric and uniform in the azimuth for both basis states, each with an azimuthal helicity in phase of opposite sign. These properties allow OAM mode of opposite helicity to be treated as two paths, indistinguishable in the intensity domain, so that one may conceive an OAM quantum eraser as depicted in Fig. 4-1(b).

To create an analogous quantum eraser for OAM we require a hybrid entangled state of OAM and polarisation. To generate the hybrid entanglement, we consider type I spontaneous parametric down-conversion (SPDC) as a source of entangled photons and employ geometric phase control of one of the entangled pairs using Pancharatnam-Berry phase to execute spin-orbit coupling.

The quantum state of the photon pair produced from a type I SPDC process is

$$|\Psi\rangle = \sum_\ell c_{|\ell|} |\ell\rangle_A |-\ell\rangle_B |H\rangle_A |H\rangle_B, \tag{4.7}$$

where $|c_\ell|^2$ is the probability of finding photon A and B in the state $|\pm\ell\rangle$.

The hybrid entanglement between photon A and B is obtained by using geometric phase control to perform an orbit-to-spin conversion in arm A [37,117]. This may be done by using a q-plate [10,71], a wave-plate with a locally varying birefringence, that couples the polarization and OAM DoF of light according to the rules in Eq. (2.9) of Chapter 2, where $|L\rangle$ and $|R\rangle$ represent the left and right circular polarization states

and q is the charge of the q-plate. Noting that $|H\rangle = (|R\rangle + |L\rangle)/\sqrt{2}$ and applying the transformation of the q-plate to photon A transforms Eq. (4.7) to

$$|\Psi\rangle \xrightarrow{\hat{Q}_A} \sum_\ell c_{|\ell|} \big(|\ell + 2q\rangle_A |R\rangle_A$$
$$+ |\ell - 2q\rangle_A |L\rangle_A \big) |-\ell\rangle_B |H\rangle_B, \tag{4.8}$$

where $\hat{Q}_A$ is the transformation of the q-plate. Coupling photon A into a single mode fiber imposes the condition $\ell = \pm 2q$ on the entangled pair (since the OAM of A and B must now be zero). Subsequently, the post-selected two-photon state reduces to

$$|\Psi'\rangle_{AB} = \frac{1}{\sqrt{2}} \big(|R\rangle_A |\ell\rangle_B + |L\rangle_A |-\ell\rangle_B \big), \tag{4.9}$$

where $\ell = 2q$. Equation (4.9) represents a maximally entangled Bell state where the polarization DoF of photon A is entangled with the OAM degree of freedom of photon B, as desired.

To obtain the OAM information of photon B, the circular polarization of photon A is converted to linear polarization using a $\lambda/4$ wave plate inserted after the q-plate and oriented at $\pi/4$ with respect to the horizontal. Therefore Eq. (4.9) becomes

$$|\psi\rangle_{AB} = \frac{1}{\sqrt{2}} \big(|H\rangle_A |\ell\rangle_B + e^{i\delta} |V\rangle_A |-\ell\rangle_B \big). \tag{4.10}$$

Here $\delta = \pi/2$ is a relative phase after the transformation of the $\lambda/4$ wave-plate. We note that the OAM "path" is marked by polarisation. When one path is selected in this way, no interference appears. However, just as in the double slit case, a projection of the polarization of photon A onto a complimentary basis state (diagonal or anti-diagonal) will collapse the state of photon B into a superposition of OAM, $|+\ell\rangle + i |-\ell\rangle$, leading to the emergence of azimuthal intensity fringes with angular frequency proportional to $2|\ell|$. An example for the $|\ell| = 5$ subspace is shown in Fig. 4-1 (c). In this case the OAM "path" information is erased.

62

4.2.3 Detection scheme

Suppose the state of the hybrid entangled system is represented by Eq. (4.10). A polarizer orientated at an angle α (with respect to the horizontal) in arm A will project photon A onto the following target state

$$|\alpha\rangle_A = \cos(\alpha) |H\rangle_A + \sin(\alpha) |V\rangle_A, \tag{4.11}$$

thus allowing the "path" to evolve from marked to unmarked by a judicious choice of α. Next, the visibility of fringes in arm B needs to be detected, which may easily be done with scanning detectors (or more expensive camera-based systems). We instead make use of scanning holograms and a fixed detector as our pattern sensitive detector [118]. We create sector states from superpositions of OAM with a relative intermodal phase of θ:

$$|\theta\rangle_B = \left(|\ell\rangle_B + e^{i2\theta} |-\ell\rangle_B \right). \tag{4.12}$$

The phase structure of $|\theta\rangle_B$ is azimuthally periodic, and allows a measurement of the path (OAM) interference in arm B, analogous to detecting OAM entanglement with Bell-like measurements [21–23, 119]. Thus the fringe pattern (or lack thereof) can be detected by scanning through θ.

The normalized probability of detection given the two projections is

$$P(\alpha, \theta) \propto |\langle\theta|_B \langle\alpha|_A |\psi\rangle_{AB}|^2$$
$$= \frac{1}{2}(1 + \sin(2\alpha)\cos(2\theta + \delta)). \tag{4.13}$$

$P(\alpha, \theta)$ is synonymous to the coincidence counts of the entangled pair. When the polarizer is orientated at $\alpha = 0$, which corresponds to the $|H\rangle$ polarization state, the probability distribution with respect to θ is a constant since the path is marked. Conversely, for $\alpha = \pm\pi/4$ which corresponds to complimentary polarization projections on $|D\rangle$ or $|A\rangle$, then $P(\alpha = \pm\pi/4, \theta) \propto 1 \pm \cos(\theta + \delta)$ and hence the oscillation is an indication of an interference pattern emerging from a superposition of the OAM paths of photon B. Therefore the which-path (OAM) information has been erased.
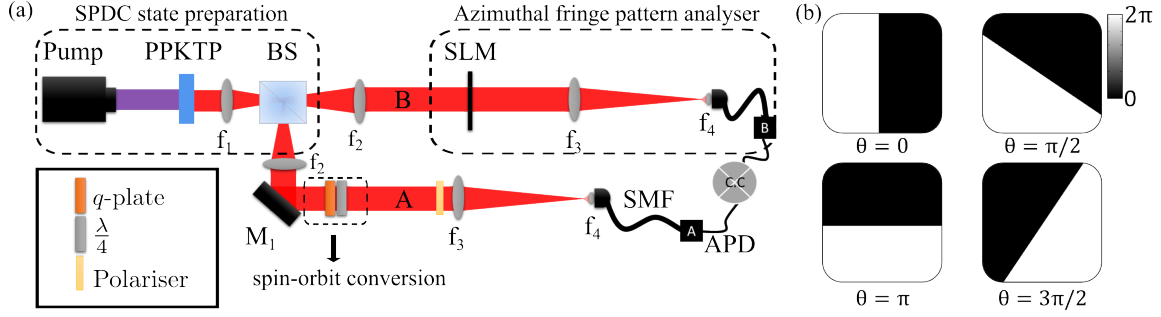
Figure 4-2: (a) Experimental setup for the hybrid entanglement based quantum eraser. The SPDC state was prepared at the plane of the non-linear crystal (PPKTP) and imaged onto the spatial light modulator (SLM) in arm B. The same imaging system was replicated in arm A, where the crystal plane was imaged onto the polariser while the OAM to spin (polarisation) conversion was obtained through the geometric phase control of photon A using a q-plate (q=0.5). The imaging system consisted of lenses $f_1 = 100$ mm and $f_2 = 300$ mm. Lenses $f_3 = 500$ mm and $f_4 = 2$ mm were used to couple the photons into single mode fibers (SMF). Note that the photons passed through 10 nm bandwidth interference filters (IF) prior to collection. The SMFs were coupled to avalanche photon diodes (APD) which detected the down-converted photons in coincidence. Furthermore, we performed a delay measure type eraser by extending arm A by 2.3 m, corresponding to a relative delay time of 7.66 ns with the polariser placed after the lens f_3. (b) Angular phase masks that were encoded on the SLM and rotated by an angle θ, serving as an azimuthal scanner to detect the spatial fringes.

The fringe visibility is given by

$$V = \frac{P_{\max} + P_{\min}}{P_{\max} + P_{\min}}. \tag{4.14}$$

Here, $P_{\max}$ and $P_{\min}$ are the maximum and minimum photon probabilities obtained from the azimuthal scanning, respectively. The theoretical visibility of the interference fringes with respect to the angle of the polarizer (α) is $V = |\sin(2\alpha)|$.

4.3   Experimental set-up

In Fig. 4-2 (a), we present the experimental set-up for our quantum eraser with polarization-OAM hybrid entangled photons when the path lengths of arm A and arm B are equal. A periodically poled potassium titanyl phosphate (PPKTP) nonlinear crystal, cut for type 1 phase matching, was pumped with a 100 mW Coherent Cube diode laser with a 450 nm nominal wavelength, producing collinear entangled photon

pairs at a wavelength of 810 nm. Each photon pair was spatially separated in two arms using a 50/50 beam splitter (BS). The spin-orbit conversion was achieved by inserting a q-plate with $q = 0.5$ in arm A, creating polarisation-OAM hybrid entanglement in the $|\ell| = \pm 1$ subspace. In this arrangement, the state of the system is given by Eq. (4.9). To mark the states, a $\lambda/4$ wave plate with fast axis at $\pi/4$ with respect to the horizontal direction, as well as a linear polarizer (eraser), were inserted in arm A. The detection in arm B was performed with binary phase masks shown in Fig.4-2 (b), encoded on a phase-only spatial light modulator (Holoeye PLUTO) to scan the spatial distribution of photon B; this was done for $\alpha = [0, \pi/4]$ while scanning holograms through $\theta = [0, 2\pi]$. Note that the crystal plane was imaged onto the SLM and polariser which are placed at equivalent positions relative to each other. The modulated photons were collected with a single mode fiber and measured in coincidence with a 25 ns gating time between two avalanche photo-diodes (Perkin-Elmer) that were inserted at the end of arms A and B. In delayed measurement mode we extended arm A by 2.3 m and moved the polariser nearer to the lens (f_3). Thus the analysis of the spatial fringes occurs before the polarisation projection.

4.4   Results

The OAM path information of photon B was obtained by projecting photon A onto the states $|H\rangle$ or $|V\rangle$. Here we chose $|H\rangle$, by setting the polarizer in arm A to $\alpha = 0$, collapsing the state of photon B to the OAM $|\ell = 1\rangle$. The results are presented in Fig. 4-3 (a), confirming that no interference fringes were observed. The small oscillations are due to imperfections in the polarization filtering of photon A. The calculated visibility of the interference fringes is 0.04 ± 0.01, in good agreement with the theoretical value of 0. One can interpret this as photon B carrying a well defined amount OAM, or equivalently, that the OAM path is marked (distinguished) and thus visibility is zero. The OAM path information was erased by performing a complimentary measurement of the polarization of photon A. We set the polarizer angle to $\alpha = -\pi/4$, thus selecting the polarization state $|A\rangle$, collapsing the state of
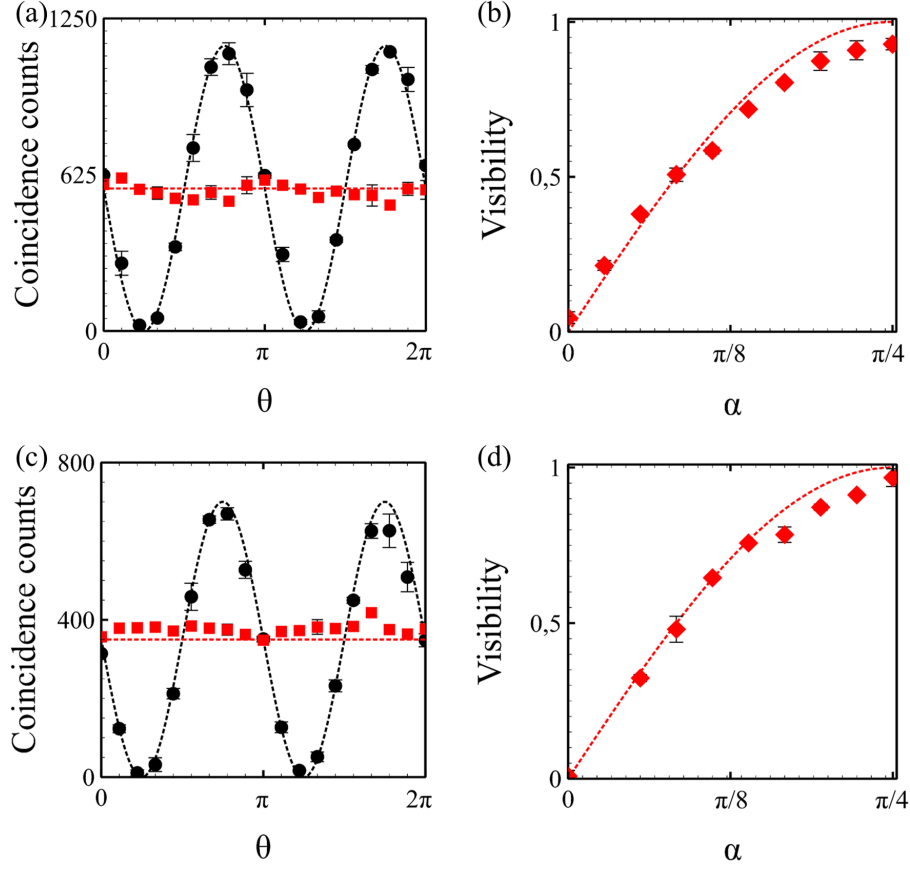
Figure 4-3: Comparison of theory and experiment for a OAM quantum eraser. (a) Interference measurements where the OAM path information of photon B is distinguished (squares) and erased (circles) by marking the path with a polarisation choice on photon A. (b) Visibility of interference fringes with a variation of the polariser angle (α) in the range 0 to $\pi/4$. Similarly, (c) delayed-choice measurement results where the OAM path is distinguished (squares) and erased (circles), and subsequence measurements of the fringe visibility (d) with the polariser angle. In all panels experimental data is shown as symbols with error bars and theoretical calculations as dashed curves. In some frames the error bars are of similar scale to the symbols.

photon B into a superposition of OAM: $|1\rangle - i|-1\rangle$. The coincidence counts from the azimuthal scanning are presented in Fig.4-3 (a), where interference fringes with a visibility of 0.92 ± 0.01 are observed, indicating that the path information has been erased, and equivalently, the OAM of the photon. The detection probability function is consistent with the theory of Eq. (4.13).

Next, the polarizer angle was varied in the range $\alpha = 0$ through π with subsequent measurements of the spatial pattern. The visibility of the interference fringes with respect to the polarizer orientation was calculated from the measured data and is

presented in Fig. 4-3 (b). The interference fringes are minimal at $\alpha = 0$ and maximal when $\alpha = \pi/4$, as expected. Indeed, the polarizer controls the interference between the two OAM paths with a visibility proportional to $|\sin(2\alpha)|$, as predicted by the theory.

Finally, we performed a delayed measurement variation of the quantum eraser by extending the path length of arm A by 2.3 m, with the experimental results presented in Fig. 4-3 (c) and (d). The same procedures were used to mark the OAM paths and to erased the path information. The visibility with respect to the variation of the polarizer angle was calculated and presented in Fig. 4-3 (d), showing a range from $V = 0.008 \pm 0.01$ to $V = 0.96 \pm 0.02$, in good agreement with theory.

Complementarity between path information and fringe visibility is essential to the quantum eraser. By defining the two distinct paths using the OAM DoF, we have shown that through polarisation-OAM hybrid entanglement, it is possible to distinguish ($V = 0.04\pm0.01$) and erase ($V = 0.92\pm0.01$) the OAM path information of a photon through the polarisation control of its entangled twin. Our work is consistent with previous studies using entanglement and linear momentum of light [25], as well as with angular fringes observed with weak classical light [113], both of which used physical paths rather than abstract paths for the path interference. Our delayed-choice experiment highlights the extent to which information is made available to an observer through a delayed measurement variation of the quantum eraser, where the analysis of the fringe pattern occurs before the decision to mark the paths (or not) is made. Indeed, we distinguished ($V = 0.008 \pm 0.01$) and erased ($V = 0.96 \pm 0.02$) the OAM path information, showing that causality does not play a role in the outcome path interference, which is a non-classical property of quantum mechanics. The improvement in the visibility of our results is due to the enhanced quality of the spin-orbit modulation owing to the extension of the distance between detection system and q-plate: the quality of the OAM mode improves with propagation. Furthermore, mutual exclusivity between the visibility and path information was demonstrated by varying the amount of OAM path information present in the system.

Significantly, our scheme shows the important role of hybrid entanglement which

has been discussed previously as the main aspect of the quantum eraser [9, 26]. Abstracting the path to OAM, with all the versatile tools that come with this choice of path, may provide the possibility of finding new approaches for studies in quantum information and communication. While we note that in principle any degree of freedom may be used, OAM is an attractive choice due to the possibility to explore the impact of dimensionality in such systems, given that it offers an infinitely large Hilbert space in which to operate. Finally, our scheme contrasts previous reports that rely primarily on traditional path-phase interferometric methods, overcoming the sensitivity and complexity of such experiments.

In conclusion, we have shown that the OAM of a photon may be treated as an abstract path, reminiscent of a slit. Using OAM-polarization hybrid entanglement, we have shown that, just as in the double slit quantum eraser, the OAM information of a photon that is marked with orthogonal polarizations can be erased through the polarization control of a bi-photon twin, both in the conventional scheme and in a delayed measurement type arrangement. In both schemes the fringe visibility increases with a reduction in the OAM path information.

Chapter 5

High-bit-rate quantum key distribution with entangled internal degrees of freedom of photons

Quantum communication over long distances is integral to information security and has been demonstrated in free space and fibre with two-dimensional polarisation states of light. Although increased bit rates can be achieved using high-dimensional encoding with spatial modes of light, the efficient detection of high-dimensional states remains a challenge to realise the full benefit of the increased state space. Here we exploit the entanglement between spatial modes and polarization to realise a four-dimensional quantum key distribution (QKD) protocol based on eigenmodes of free-space and fibre. We introduce a detection scheme which allows for the detection of all basis modes in a high-dimensional space deterministically, and demonstrate efficient QKD at high secure key and sift rates, with the highest capacity-to-dimension reported to date. This work opens the possibility to increase the dimensionality of the state-space indefinitely while still maintaining deterministic detection and will be invaluable for long distance "secure and fast" data transfer.

5.1   Introduction

The use of polarization encoded qubits has become ubiquitous in quantum communication protocols with single photons [120–123]. Most notably, they have enabled unconditionally secure cryptography protocols through quantum key distribution (QKD) over appreciable distances [124–126]. With the increasing technological prowess in the field, faster and efficient key generation together with robustness to third party attacks have become paramount issues to address. A topical approach to overcome these hurdles is through higher-dimensional QKD: increasing the dimensionality, d, of a QKD protocol leads to better security and higher secure key rates, with each photon carrying up to $\log_2(d)$ bits of information [47, 48].

Employing spatial modes of light, particularly those carrying orbital angular momentum (OAM), has shown considerable improvements in data transfer of classical communication systems [127–129]. However, realizing high-dimensional quantum communication remains challenging. To date, the list of reports on high dimensional QKD with spatial modes is not exhaustive, and include protocols in up to $d = 7$ [56, 58].

Photons with complex spatial and polarization structure, commonly known as vector modes, have been used as information carriers for polarisation encoded qubits in alignment-free QKD [46, 130], exploiting the fact that vector modes that carry OAM exhibit rotational symmetry, removing the need to align the detectors in order to reconcile the encoding and decoding bases, as would be the case in QKD with only polarization. In these vector modes, the spatial and polarization degrees of freedom (DoFs) are coupled in a non-separable manner, reminiscent of entanglement in quantum mechanics. This non-separability can be used to encode information and has been done so with classical light [131, 132], for example, in mode division multiplexing [133].

Here we use vector OAM modes (vector vortex modes) to realize four-dimensional QKD based on the "BB84" protocol [6]. Rather than carrying information encoded in one DoF, the non-separable state can itself constitute a basis for a higher dimensional

space that combines two DoFs, namely the spatial and polarisation DoFs. Importantly, our basis is made from the natural modes of free-space and optical fibre (e.g., step-index fibre), thus facilitating long distance transport of information. To fully benefit from the increased state space, we introduce a new detection scheme that, deterministically and without dimension dependent sifting loss, can detect all basis elements in our high-dimensional space. This differs from previous schemes that have used mode filters as detectors, sifting through the space one mode at a time, thus removing all benefit of the dimensionality of the space, or have used mode sets that are not suitable for long distance propagation (see for example ref. [56]) Our approach combines manipulations of the dynamic and Panchanratnam-Berry phase with static optical elements and, in principle, allows detection of the basis elements with unit probability. We demonstrate high-dimensional encoding/decoding in our entangled space, obtaining a detection fidelity as high as 97%, with a secret key rate of 1.52 bits per photon and quantum error rate of 3%. As a means of comparison to other protocols, we calculated the capacity-to-dimension ratio and show that our scheme is more efficient than any other reported to date.

5.2   Methods and Results

5.2.1   High-dimensional encoding

The first QKD demonstrations were performed using the polarisation DoF, namely, states in the space spanned by left- circular $|L\rangle$ and right-circular polarization $|R\rangle$, i.e., $\mathcal{H}_\sigma = \mathrm{span}\{|L\rangle, |R\rangle\}$, and later using the spatial mode of light as a DoF, e.g., space spanned by the OAM modes $|\ell\rangle$ and $|-\ell\rangle$, i.e. $\mathcal{H}_\ell = \mathrm{span}\{|\ell\rangle, |-\ell\rangle\}$. Using entangled states in both DoFs allows one to access an even larger state space, i.e., $\mathcal{H}_{\sigma,\ell} = \mathcal{H}_\sigma \otimes \mathcal{H}_\ell$, described by the higher-order Poincaré sphere [134, 135]. Employing multiple OAM values the final state space is a direct sum of the subspaces $\mathcal{H}_{\sigma,\ell}$ for different ℓ:

$$\mathcal{H}_M = \bigoplus_{\ell \in M} \mathcal{H}_{\sigma,\ell}, \tag{5.1}$$
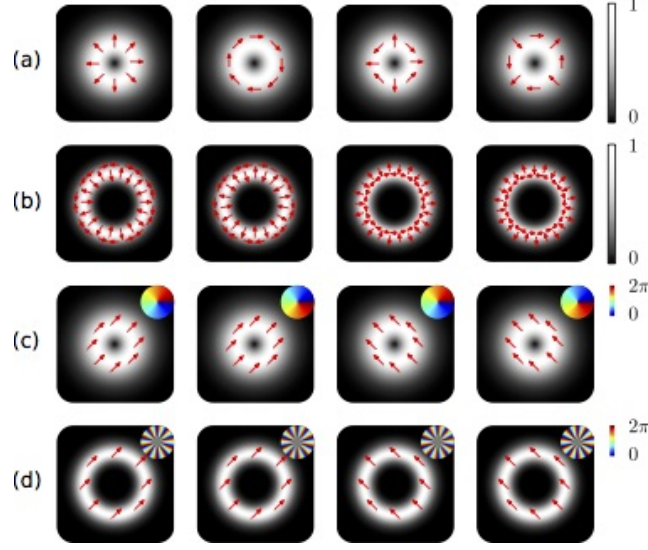
Figure 5-1: Vector vortex modes for (a) $\ell = \pm 1$ and (b) $\ell = \pm 10$, with the mutually unbiased scalar modes also for the (c) $\ell = \pm 1$ and (d) $\ell = \pm 10$ subspaces. The insets show the azimuthally varying phase profile of the scalar/OAM modes.

where $M \subset \mathbb{N}$ and the direct sum $\bigoplus$ of vector spaces A_i is given by $\bigoplus_i A_i = \{\sum_i \alpha_i |a_i\rangle : |a_i\rangle \in A_i, \alpha_i \in \mathbb{C}\}$. The dimension of $\mathcal{H}_M$ equals the sum of the dimensions of the subspaces $\mathcal{H}_{\sigma,\ell}$, i.e. $d = 4N$, with $N = |\Omega|$ being the number of different values $|\ell|$ (subspaces). This opens the way to infinite dimensional encoding using such entangled states. For example, using only the $|\ell|$ subspace of OAM ($N = 1$) leads to a four dimensional space spanned by $\{|\ell, L\rangle, |-\ell, L\rangle, |\ell, R\rangle, |-\ell, R\rangle\}$. It is precisely in this four-dimensional subspace that, here, we define our vector and scalar modes. Alice randomly prepares photons in modes from two sets: a vector mode set, $|\psi\rangle_{\ell,\theta}$, and a mutually unbiased scalar mode set, $|\phi\rangle_{\ell,\theta}$, defined as

$$|\psi\rangle_{\ell,\theta} = \frac{1}{\sqrt{2}}(|R\rangle|\ell\rangle + e^{i\theta}|L\rangle|-\ell\rangle), \tag{5.2}$$

$$|\phi\rangle_{\ell,\theta} = \frac{1}{\sqrt{2}}\left(|R\rangle + e^{i\left(\theta-\frac{\pi}{2}\right)}|L\rangle\right)|\ell\rangle, \tag{5.3}$$

where each OAM state ($|\pm\ell\rangle$) carries $\pm\ell\hbar$ quanta of OAM, $|R\rangle$ and $|L\rangle$ are, respectively, the right and left circular polarization eigenstates and $\theta = 0$ or π is the intra-modal phase. For a given $|\ell|$ OAM subspace, there exist four orthogonal modes

in both the vector basis (Eq. (5.2)) and its mutually unbiased counterpart (Eq. (5.3)), such that $|\langle\psi\rangle\,\phi|^2 = 1/d$ with $d = 4$. These vector and scalar modes can be generated by manipulating the dynamic or geometric phase of light [45, 136–138]. Our four vector modes for QKD are:

$$|00\rangle_v \;\; = \;\; \frac{1}{\sqrt{2}}(|R\rangle\,|\ell\rangle + |L\rangle\,|-\ell\rangle), \tag{5.4}$$

$$|01\rangle_v \;\; = \;\; \frac{1}{\sqrt{2}}(|R\rangle\,|\ell\rangle - |L\rangle\,|-\ell\rangle), \tag{5.5}$$

$$|10\rangle_v \;\; = \;\; \frac{1}{\sqrt{2}}(|L\rangle\,|\ell\rangle + |R\rangle\,|-\ell\rangle), \tag{5.6}$$

$$|11\rangle_v \;\; = \;\; \frac{1}{\sqrt{2}}(|L\rangle\,|\ell\rangle - |R\rangle\,|-\ell\rangle), \tag{5.7}$$

with corresponding mutually unbiased bases (MUB)

$$|00\rangle_s \;\; = \;\; |D\rangle\,|-\ell\rangle\,, \tag{5.8}$$

$$|01\rangle_s \;\; = \;\; |D\rangle\,|\ell\rangle\,, \tag{5.9}$$

$$|10\rangle_s \;\; = \;\; |A\rangle\,|-\ell\rangle\,, \tag{5.10}$$

$$|11\rangle_s \;\; = \;\; |A\rangle\,|\ell\rangle\,, \tag{5.11}$$

where the subscripts s and v refer to, respectively, the scalar and vector mode basis, while D and A are the diagonal and anti-diagonal polarisation states. For the purpose of demonstration, we use vector and scalar modes in the $\ell = \pm 1$ and $\ell = \pm 10$ OAM subspaces, shown graphically in Fig. 5-1.

5.2.2 Mode generation

We used q-plates to couple the polarisation and orbital angular momentum degrees of freedom through geometric phase control [10, 139]. With locally varying birefringence across a wave plate, the geometric phase imparted by a q-plate was engineered to produce transformation given by Eq. (2.9) in Sec. 2.2 The vector modes investigated here were generated by transforming an input linearly polarized Gaussian mode with quarter- or half- wave plates and $q = 1/2$ and $q = 5$ plates, producing either separable
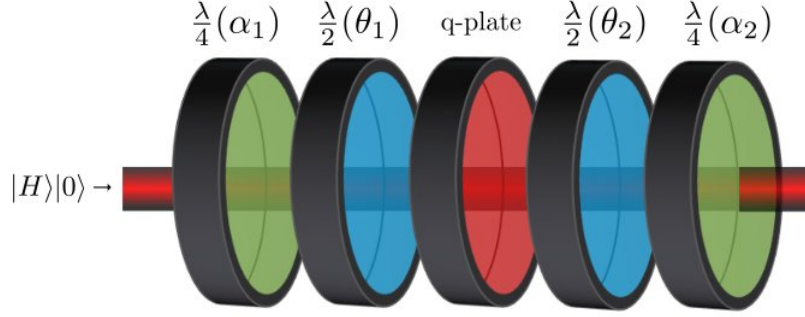
Figure 5-2: We generate the set of vector and scalar modes using a q-plate and wave plates ($\lambda/2$ and $\lambda/4$) stacked and orientated at angles given in Table. 5.1. We use the $\lambda/4$ wave plates to convert between linear and circular polarisation states and the $\lambda/2$ plates to rotate between desired linear polarisation states. The generation scheme assumes an input of horizontally polarised light with a Gaussian profile ($|H\rangle|0\rangle$).

(scalar) non-separable (vector) superpositions of qubit states in Eqs. (5.2) and (5.3).

The generated states and the elements setting are given in Table 5.1.

Table 5.1: Generation of MUBs of vector and scalar modes from an input, horizontally polarized Gaussian beam. The wave-plate angles are defined with respect to the fast axis of each plate.

Mode	$\lambda/4(\alpha_1)$	$\lambda/2(\theta_1)$	q-plate	$\lambda/4(\alpha_2)$	$\lambda/2(\theta_2)$
$|\psi\rangle_{\ell,0}$	$-$	0	$|q|$	$-$	$-$
$|\psi\rangle_{\ell,\pi}$	$-$	$\pi/4$	$|q|$	$-$	$-$
$|\psi\rangle_{-\ell,0}$	$-$	$-$	$|q|$	$-$	0
$|\psi\rangle_{-\ell,\pi}$	$-$	$-$	$|q|$	$-$	$\pi/4$
$|\phi\rangle_{\ell,0}$	$-\pi/4$	$-$	$|q|$	$-\pi/4$	$\pi/4$
$|\phi\rangle_{\ell,\pi}$	$-\pi/4$	$-$	$|q|$	$-\pi/4$	$-\pi/4$
$|\phi\rangle_{-\ell,0}$	$\pi/4$	$-$	$|q|$	$\pi/4$	$\pi/4$
$|\phi\rangle_{-\ell,\pi}$	$\pi/4$	$-$	$|q|$	$\pi/4$	$-\pi/4$

5.2.3 High-dimensional decoding

At the receiver's end, Bob randomly opts to measure the received photon in either the scalar or vector basis. The randomness of the choice between the two bases is implemented here with a 50:50 beam splitter (BS) as shown in Fig. 5-3(a) – due to the quantum nature of the photon, there is an equal probability that the photon will be measured in either of the two bases. Prior QKD experiments beyond two-
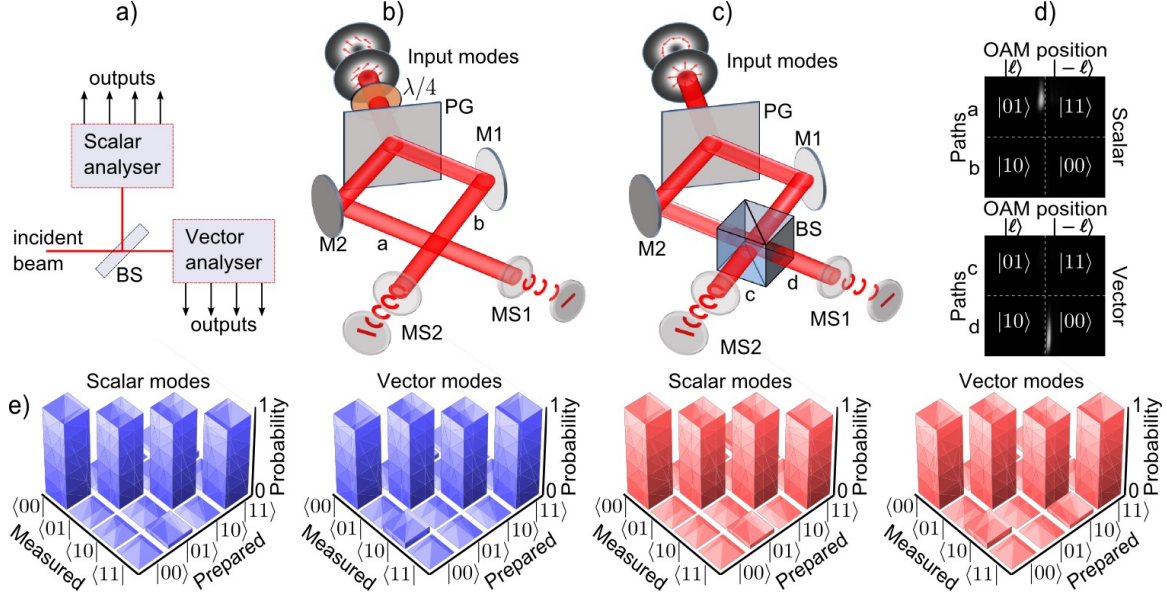
Figure 5-3: (a) Bob randomly selects to measure the incoming single photon from Alice in either the $|\psi\rangle_\ell$ (vector) or $|\phi\rangle_\ell$ (scalar) basis and detects the photon deterministically with eight detection ports. (b) The $|\phi\rangle_\ell$ scalar analyser first convert linear to circular polarisation using a quarter-wave plate, then polarisation to path with a polarisation grating (PG). Subsequently the OAM states are measured using mode sorters (MS1 and MS2) that map OAM to position. (c) The $|\psi\rangle_\ell$ vector analyser works in analogous fashion, with the exception that the paths after the PG are interfered on a beam-splitter (BS) before passing the resulting output from each port to an OAM detector (mode sorter). (d) The input states prepared by Alice are now unambiguously mapped to detectors in Bob's measurement system, allowing all states to be detected with the eight detectors. Classical experimental data is shown for two examples from the $\ell = \pm 10$ subspace. (e) Experimental confirmation of Bob's detection scheme for both $|\psi\rangle_\ell$ and $|\phi\rangle_\ell$ states prepared by Alice, for $\ell = \pm 1$ (blue) and $\ell = \pm 10$ (red).

dimensions have used filtering based techniques that negate the very benefit of the increased state space as highlighted in [140]; by filtering for only one mode at a time, the effective data transfer rate is reduced by a factor $1/d$. We introduce a new scheme to deterministically detect the modes, as detailed in Fig. 5-3 (b) and (c), that has a number of practical advantages for quantum cryptography. Consider a vector mode as defined in Eq. (5.2). The sorting of the different vector modes is achieved through a combination of geometric phase control and multi-path interference. First, a polarisation grating based on geometric phase acts as a beam splitter for left- and

right-circularly polarised photons, creating two paths

$$|\Psi\rangle_{\ell,\theta} \rightarrow \frac{1}{\sqrt{2}} \left(|R\rangle_a |\ell\rangle_a + e^{i\theta} |L\rangle_b |-\ell\rangle_b \right), \qquad (5.12)$$

where the subscript a and b refer to the polarisation-marked paths.

The photon paths a and b are interfered at a 50:50 BS, resulting in the following state after the BS:

$$|\Psi'\rangle_{\ell,\theta} = \frac{1 + e^{i(\delta+\theta+\frac{\pi}{2})}}{2} |\ell\rangle_c + i\frac{1 + e^{i(\delta+\theta-\frac{\pi}{2})}}{2} |-\ell\rangle_d, \qquad (5.13)$$

where the subscripts c and d refer to the output ports of the beam splitter and δ is the dynamic phase difference between the two paths. Note that the polarisation of the two paths is automatically reconciled in each of the output ports of the beam splitter due to the difference of parity in the number of reflections for each input arm. Also note that at this point it is not necessary to retain the polarisation kets in the expression of the photon state since the polarisation information is contained in the path. In our setup we set $\delta = \pi/2$, reducing the state in Eq. (5.13) to

$$|\Psi'\rangle_{\ell,\theta} = \frac{1 - e^{i\theta}}{2} |\ell\rangle_c + i\frac{1 + e^{i\theta}}{2} |-\ell\rangle_d. \qquad (5.14)$$

The measurement system is completed by passing each of the outputs in c and d through a mode sorter and collecting the photons using 4 fibres coupled to avalanche photodiodes. The mode sorters are refractive (lossless) aspheres that map OAM to position [141–144]. While it is trivial to measure such entangled (non-separable) vector states at the classical level with many photons [131,133,145], with our approach each such state is detected with, in principle, unit probability at the single photon level. For example, consider the modes $|00\rangle$ and $|01\rangle$, where $\theta = 0$ and $\theta = \pi$, respectively. The mapping is such that

$$|00\rangle \quad \rightarrow \quad |\Psi'\rangle_{\ell,0} = i\,|-\ell\rangle_d\,, \qquad (5.15)$$

$$|01\rangle \quad \rightarrow \quad |\Psi'\rangle_{\ell,\pi} = -\,|\ell\rangle_c\,, \qquad (5.16)$$

where the indices c and d label the output ports of the BS. Thus, through this path interference, the vector modes are mapped such that $|00\rangle$ produces a signal in port d at position X_ℓ while $|01\rangle$ produces a signal in port c at position $X_{-\ell}$. Sample results for these modes are shown in Fig. 5-3(d) and for all states in the Methods. Thus the combination of path (c or d) and lateral location (X_ℓ or $X_{-\ell}$) uniquely determines the original vector mode.

The scalar mode detector works on an analogous principle but without the need of the BS to resolve the intermodal phases. The polarisation states are resolved by first performing a unitary transformation that maps linear to circular basis, and passing the scalar mode through the polarisation grating. The OAM states are subsequently sorted using the mode sorters.

5.2.4 Sorting of scalar and vector modes OAM mode

We use a compact phase element to perform a geometric transformation on OAM modes such that azimuthal phase is mapped to a transverse phase variation, i.e., a tilted wavefront. The first optical element of our OAM mode sorter performs a conformal mapping in the standard Cartesian coordinates, from a position in the input plane (x, y) to one in the output plane (u, v), such that

$$u \quad = \quad \frac{d}{2\pi}\arctan\left(\frac{y}{x}\right), \qquad (5.17)$$

$$v \quad = \quad -\frac{d}{2\pi}\ln\left(\frac{\sqrt{x^2 + y^2}}{b},\right) \qquad (5.18)$$

where d is the aperture size of the free form optics and b is a scaling factor that controls the translation of the transformed beam in the u direction of the new coordinate
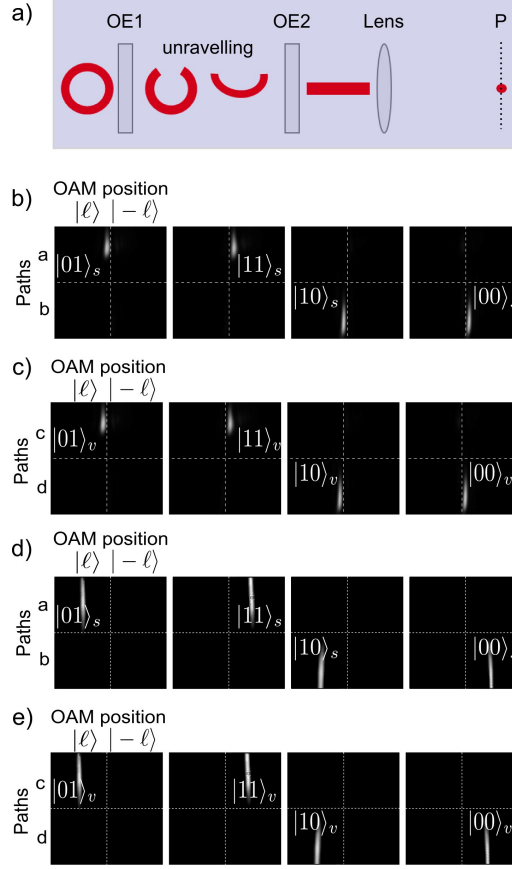
Figure 5-4: (a) We use a mode sorter that consists of two refractive optical lenses, OE1 and OE2 which transform the azimuthal phase into a linear phase and mapped onto unique positions. The input mode unravels after OE1 and a linear phase is retained by OE2. The phase is then mapped onto a position unique to the azimuthal charge by a Fourier lens. We use these lenses to map the mode set $(|\phi\rangle, |\psi\rangle)$ onto positions based on their orbital angular momentum. Here (b) and (c) are the scalar and vector mode CCD camera images of the signal (elongated spots) when $\ell = \pm 1$, and (d) and (e) for $\ell = \pm 10$. The detection schemes corresponding to the scalar and vector analysis are illustrated in Fig. 5-3.

system. The result is that after passing through a second phase-correcting optic and then a Fourier transforming lens (of focal length f), the input OAM (ℓ) is mapped to output positions, X_ℓ, following

$$X_\ell = \frac{\lambda f \ell}{d}. \tag{5.19}$$

This conformal mapping of ring to line to point, is shown in Fig. 5-4(a). The classical result for the vector and scalar detections are shown in Figs. 5-4(b) and (c) for $|\ell| = 1$, and in Figs. 5-4(d) and (e) for $|\ell| = 10$. Note that here, we use standard

78

Table 5.2: Mode detection paths and respective positions of the spots after the mode sorter

Mode	Path	Spot position
$|\psi\rangle_{\ell,0}$	c	X_ℓ
$|\psi\rangle_{\ell,\pi}$	d	X_ℓ
$|\psi\rangle_{-\ell,0}$	c	$X_{-\ell}$
$|\psi\rangle_{-\ell,\pi}$	d	$X_{-\ell}$
$|\phi\rangle_{\ell,0}$	a	X_ℓ
$|\phi\rangle_{\ell,\pi}$	b	X_ℓ
$|\phi\rangle_{-\ell,0}$	a	$X_{-\ell}$
$|\phi\rangle_{-\ell,\pi}$	b	$X_{-\ell}$

convex lenses to do the mapping to position, as opposed to cylindrical lenses which would transform the lines to a point. A summary of the scalar and vector detection is shown in Table 5.2.

5.2.5 Crosstalk analysis

The crosstalk analysis of the vector ($|\psi\rangle$) and scalar ($|\phi\rangle$) modes is represented by a matrix of detection probabilities for each of the modes sent by Alice (rows) and measured by Bob (columns). The entries are partitioned into four quadrants: the diagonal quadrants correspond to the outcomes of measurements in matching bases while the off-diagonal show the outcomes of measurements in the complementary bases (see Fig.5-5 (a)).

A graphical illustration of the experimental performance of both the scalar and vector analysers is shown in Fig. 5-3(e) (the diagonal matrices of Fig. 5-5(c) and (d)), where modes from the $\ell = \pm 1$ and $\ell = \pm 10$ subsets were measured with high fidelity (approx. 97%).

5.2.6 High dimensional cryptography

We performed a four-dimensional prepare-and-measure BB84 scheme [6] using mutually unbiased vector and scalar modes. Our laser source was attenuated with neutral density filters to nearly $\mu = 0.008$ photon per pulse. We assembled single mode fiber couplers at the classically predicted positions of the strips of light. The fibers were
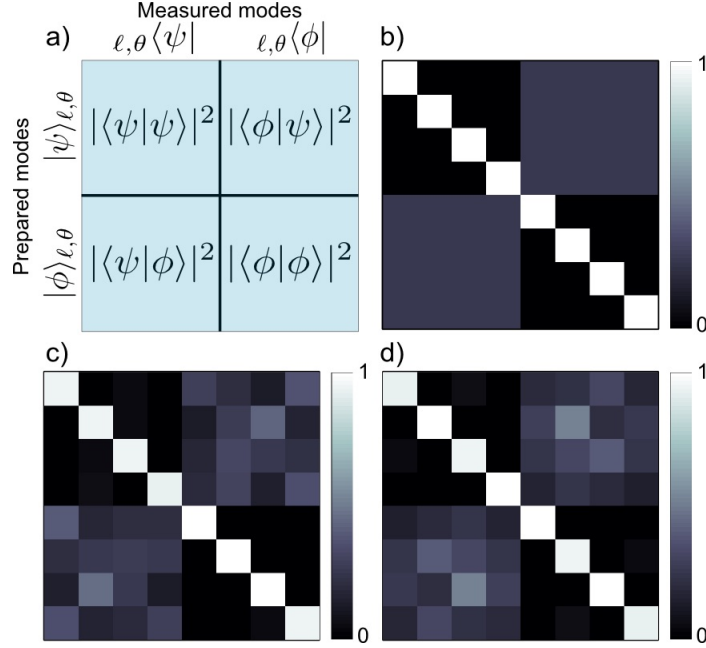
Figure 5-5: (a) Schematic of the inner product measurements performed between the vector states $|\psi\rangle_{\ell,\theta}$ and their mutually unbiased counterparts $|\phi\rangle_{\ell,\theta}$. (b) Theoretical scattering probabilities among the vector and scalar modes following the measurement process of (a). The experimental results are shown in (c) and (d) for modes in the $\ell = \pm 1$ and $\ell = \pm 10$ subspaces, respectively.

coupled to Perkin-Elmer Single photon counting modules. Alice prepared an initial state in either the $|\psi\rangle_\ell$ (vector) or $|\phi\rangle_\ell$ (scalar) basis and transmitted it to Bob, who made his measurements as detailed in the previous section. Through optical projection onto both the vector and scalar bases as laid out in Fig. 5-5(a), we determined the crosstalk matrices shown in Fig. 5-5(c) and (d), relating the input and measured modes within, respectively, the subspaces $\ell = \pm 1$ and $\ell = \pm 10$. The average fidelity of detection, measured for modes prepared and detected in identical bases, is 0.965 ± 0.004 while the overlap between modes from MUBs is $|\langle \phi| \psi\rangle|^2 = 0.255 \pm 0.004$, in good agreement with theory (0.25).

Next, we performed a four dimensional prepare-and-measure BB84 scheme using mutually unbiased vector and scalar modes. For each mode, Alice and Bob assign the bit values $00, 01, 10$ and 11, as shown in Fig. 5-6(a). During the transmission, Alice randomly prepares her photon in a vector (scalar) mode state while Bob randomly measures the photon with either the vector or scalar analyser detailed in Fig. 5-3. At
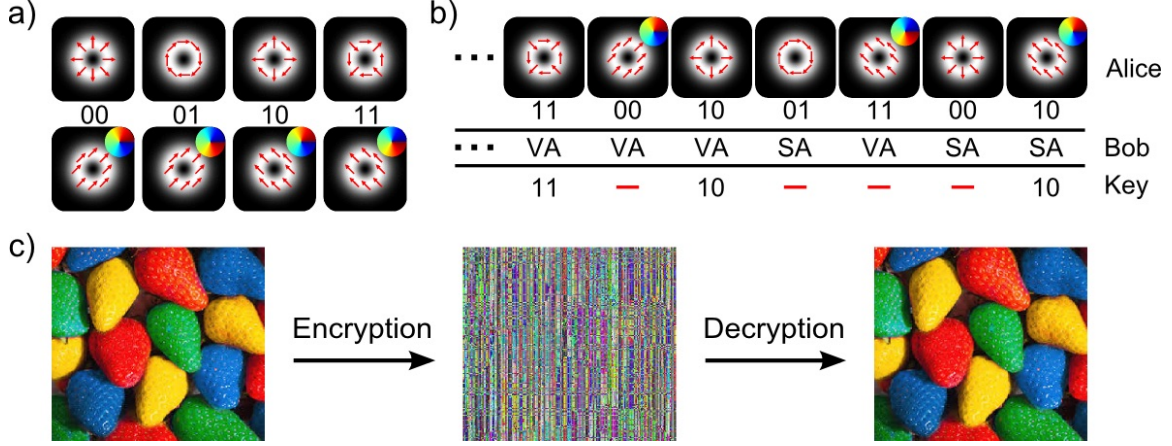
Figure 5-6: Alice and Bob agree on bit values for the vector and scalar modes. (b) Alice sends a random sequence of vector and scalar modes, which Bob randomly measures using either a vector analyser (VA) or a scalar analyser (SA). Alice and Bob, upon communication of the encoding and decoding bases through a classical channel, discard bit values for modes prepared and measured in complementary bases. (c) Shows a simple encryption/decryption of an image using a 98 bit long key, sifted from a total of 200 transmitted bits.

the end of the transmission, Alice and Bob reconcile the prepare and measure bases and discard measurements in complementary bases, as described in Fig. 5-6(b). We performed this transmission using a sequence of 100 modes and retained a sifted key of 49 spatial modes (98 bits), which was used to encrypt and decrypt a picture as shown in Fig. 5-6(c).

5.2.7   Security analysis.

From the measured crosstalk matrices in Fig. 5-5(c) and (d), we performed a security analysis on our QKD scheme in dimensions $d = 4$ for the two OAM subspaces (± 1 and ± 10). The results of the analysis are summarised in Table 5.3. From the measured detection fidelity F, we computed the mutual information between Alice and Bob in d-dimensions as follows [48]

$$I_{AB} = \log_2(d) + F \log_2(F) + (1 - F) \log_2\left(\frac{1 - F}{d - 1}\right). \tag{5.20}$$

The measured I_{AB} for $d = 4$ is nearly double (1.7×) that of the maximum achievable with only qubit states (1). Assuming a third party, Eve, uses an ideal quan-

81

Table 5.3: Summary of the security analysis on the high dimensional protocol showing the experimental and theoretical values of the detection fidelity (F), mutual information I_{AB} between Alice and Bob, Eve's cloning fidelity (F_E) and mutual information with Alice I_{AE}, as well as the quantum error rate Q and secret key rate R.

	$d = 4$ ($\ell = \pm 1$)	$d = 4$ ($\ell = \pm 10$)	
Measures	experiment	experiment	ideal
F	0.96	0.97	1.00
I_{AB}	1.69	1.76	2.00
F_E	0.44	0.41	0.25
I_{AE}	0.17	0.13	0.00
Q	0.04	0.03	0.00
R	1.39	1.52	2.00

tum cloning machine to extract information, the associated cloning fidelity, F_E, in d-dimensions is given by [48]

$$F_E = \frac{F}{d} + \frac{(d-1)(1-F)}{d} + \frac{2\sqrt{(d-1)F(1-F)}}{d}. \qquad (5.21)$$

With increasing dimensions, the four dimensional protocol reduces the efficiency of Eve's cloning machine to as low as 0.38 well below the maximum limit in a two-dimensional protocol (0.5) Thus, increasing the dimensionality of QKD protocols does indeed have, in addition to higher mutual information capacity, higher robustness to cloning based attacks.

The mutual information shared between Alice and Bob, conditioned on Bob's error – that is, Bob making a wrong measurement is as a result of Eve extracting the correct information – is computed in d-dimension as follows [48]

$$\begin{aligned} I_{AE} = \log_2(d) + (F + F_E - 1) \log_2 \left(\frac{F + F_E - 1}{F} \right) \\ + (1 - F_E) \log_2 \left(\frac{1 - F_E}{(d-1)F} \right). \end{aligned} \qquad (5.22)$$

The consequent measured quantum error rate of $Q = 1 - F = 0.04$ is well below the 0.11 and 0.18 bounds for unconditional security against coherent attacks in two and four dimensions [48], respectively. The lower bound on the secret key rate, given

by [55]

$$R = \log_2(d) + 2F \log_2(F) + 2(1 - F) \log_2 \left(\frac{1 - F}{d - 1} \right), \qquad (5.23)$$

yields a value as high as 1.52 bits per photon, well above the Shannon limit of one bit per photon achievable with qubit states. While the security of the protocol can be increased with privacy amplification, the measured four-dimensional secret key rate demonstrates the potential of such entangled modes for high bandwidth quantum communication.

Deterministic measurement versus filter-based measurement. The above analysis assumes that the detection schemes can deterministically distinguish all basis states from each basis. In the case where filters are used to distinguish a single basis element from all others, the probability to choose the filter that corresponds to the sent signal state is given by $1/d$. As such, using a filter based detection, the sifting loss grows with the dimension, d.

The sifting losses can, however, be reduced by using additional DoFs; For example, when detecting vector OAM modes, the polarization DoF can be exploited as a "marker" for the higher dimensional OAM space. This hybrid system allows the higher dimensional vector mode space to be probed two modes at a time (see App. B), thus doubling the performance of the pure filter-based technique.

In this work we present a deterministic measurement scheme where all basis modes are sorted and detected, including the mutually unbiased vector modes using single photon interference at a beam splitter. Since each mode maps to a unique position in the spatial domain, such a detection will not suffer from any dimension-dependent loss. To account for the effect of the detection system on the QKD performance, we define the effective secret key R_E, given by $R_E = \alpha R$ where α is the basis detection efficiency of the detection scheme. This would represent the bits of information that is extracted on average, for every photon sent (data transfer rate), and is shown theoretically in Fig. 5-7 (a) for the maximum allowable effective key rate, which assumes perfect Fidelity ($F = 1$) and no additional loss, together with experimental data. Deterministic measurement ($\alpha = 1$) outperforms filtering which, coincidentally, does
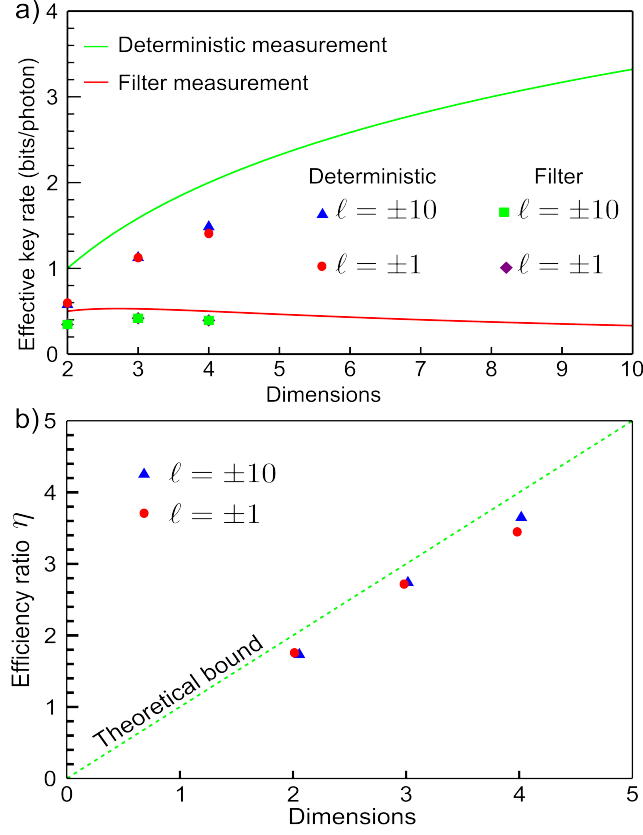
Figure 5-7: (a) Effective key rate as a function of dimension shown theoretically (solid curves) for two measurement approaches, namely, filtering and deterministic detection. Data points show measurements in the subspaces of $\ell = \pm 1$ and $\ell = \pm 10$ for three dimensions ($d = 2,3$ and 4). In (b) the efficiency ratio, η, is plotted theoretically (dashed line) together with the experimental data (symbols) inferred from (a), highlighting the performance enhancement of deterministic measurement over filter-based measurement. The theoretical plots are for a Fidelity of $F = 1$.

not show any improvement over the maximum achievable with just two dimensional polarization states. This is because the gain coefficient for filtering, given by $\alpha = 1/d$, decays faster than the logarithmic term $\log_2(d)$ grows. In other words, while higher dimensions allows more bits per photon, unless the detection is deterministic it takes many more photons to detect a particular mode from the Hilbert space, so that the very benefit of the dimensionality is negated in as far as data transfer is concerned. To test this we built a filter-based measurement scheme for comparison purposes (see Fig. B-1 in App. B), with the data shown in Fig. 5-7 (a) and (b). A graphical illustration of the performance enhancement of our scheme over a filter-based scheme

is shown in Fig. 5-7 (b) where the ratio η, defined as follows

$$\eta = \frac{R_E^{\text{deterministic}}}{R_E^{\text{filter}}}, \tag{5.24}$$

is plotted as function of the dimension, clearly showing the superiority of the deterministic detection. For example, we note that while all data points are below the allowed maximum (due to imperfect Fidelities and non-zero loss in the systems), the deterministic measurement scheme provides a $3.7\times$ enhancement in performance for $d = 4$, in good agreement with the theoretical value of $4\times$. In our analysis we have assumed in both cases that the rest of the measurement system has identical loss, which may be taken to be zero. While this is adequate for this comparative study, it is worth noting that experimental limitations do play a role in how QKD protocols scale with dimension [146].

The effective key rate (R_E) we obtained with our new vector OAM basis and its deterministic measurement exceeds previously reported [56] $d = 4$ laboratory results by more than $5\times$, the latter based on scalar OAM modes with a filter measurement scheme. In order to compare the efficiency of general higher-dimensional protocols using spatial modes of light, we define the information per photon per dimension as a figure of merit. Using this, we find that we achieve a value of 0.38, compared to reported values of 0.17 ($d = 5$) [56] and 0.24 ($d = 7$) [58], highlighting the efficiency of our scheme.

5.3 Discussion and conclusion

The prepare-and-measure quantum cryptography scheme we report here realised the potential of entanglement between spatial modes and polarisation as means to achieving higher bandwidth optical communication at the single photon level as well as classically. Our secret key rate of 1.52 bits per photon represents a significant increase in data transfer rates as compared to QKD with conventional polarisation eigenstates.

An important aspect of our scheme is the deterministic measurement of all higher

dimensional states, allowing, in principle, unit detection probability by Bob for any prepared mode by Alice. This makes it possible to increase the dimensionality of quantum cryptography protocols without compromising on the sifting rate, the fraction of the transmitted bits that constitute the key, unlike with other methods where the data transfer rate is decreased due to filtering for one mode at a time, thereby decreasing the detection probability for a given mode by a factor $1/d$. We point out that our scheme would likewise increase the signal-to-noise of classical mode division multiplexing communication systems: rather than distribute the signal across d modes, each with $1/d$ of the signal, we can achieve full signal on each mode with a factor d greater signal-to-noise ratio [147]. A major advantage is that all modes in our Hilbert space are eigenmodes of free-space and optical fibre, unlike prior QKD demonstrations with spatial modes, thus facilitating long distance applications outside the laboratory environment. Furthermore we anticipate that no benefit will be derived to Eve (mutual information between Bob/Alice and Eve) from this mode set when propagated over long distance in free space due to the identical scattering of vector and scalar OAM modes in turbulence [148].

In conclusion, we have performed efficient high-dimensional QKD using a basis formed from eigenmodes of free-space and fibre with entangled spatial and polarisation DoFs. By outlining a new measurement approach for the vector elements in this basis we were able to show that this QKD approach is capable of realising high-bits per photon at high sift rates and high data transfer rates, substantially improving on previously reported results. When combined with real-time error correction [45] that also exploits properties of this mode set, and the possibility to increase the dimensionality of the state-space indefinitely while still maintaining unit probability detection, we foresee that this approach will be invaluable for long distance "secure and fast" data transfer.

Chapter 6

Conclusion

Quantum entanglement is a property that describes systems with physical descriptions that cannot be described independently even when spatially separated by infinite distances. Although such systems are usually studied in single degree of freedom (DoF), e.g, the 2-dimensional polarisation, the high dimensional orbital angular momentum (OAM) or transverse momentum, it is possible to combine such properties to benefit from the individual characteristics of each DOF through hybrid entanglement – the entanglement between particles defined in differing DoFs. In this dissertation, I focused on the hybrid entanglement between the polarisation and OAM of light for novel applications in quantum communication and information.

In Chapter 2, I demonstrated the techniques required to generate and detect spatial modes of light with coupled DoF. To generate the spatial modes I used geometric phase control with q-plates and showed that high dimensional photon states of coupled DoFs can be unambiguously detected based on the reciprocity of light. I also showed that a projective measurement can be constructed using a spatial light modulator (SLM), a single mode fiber (SMF) and a single photon detector. These methods were crucial for engineering hybrid entanglement and measuring the spatial modes of entangled photons.

In Chapter 3, I demonstrated the techniques required to generate and detect entan-

gled photons in the OAM DoF with a periodically-poled-potassium-titanyl-phosphate (PPKTP) crystal via spontaneous parametric down-conversion (SPDC). I showed that a variance in temperature of the crystal affects the phase matching conditions (momentum and energy conservation) and consequently the geometry of the emitted photons. To detect the down-converted photons, I used digital holography based on the projective measurement technique that was demonstrated in Chapter 2. The system was assembled and characterised using a back-projection - one of the entangled photons is treated retrodictively and replaced with laser light. Furthermore, I showed that the PPKTP crystal conserved OAM. Moreover, the entanglement of the system was confirmed via a Bell-like inequality violation. I also demonstrated a full state tomography and measured the fidelities, concurrences and linear entropies which yielded results indicating that the non-linear crystal produced entangled photons that can be described by a pure OAM maximally entangled Bell state.

In Chapter 4, I used the techniques developed in Chapter 2 and 3 to generate hybrid entanglement and demonstrated a quantum eraser experiment with orbital angular momentum. The OAM entangled photons were first prepared from SPDC. Subsequently, OAM to polarisation conversion of one of the entangled photons was performed with the aid of the q-plate allowing the photon's polarisation to be entangled to the OAM of its twin. I showed that through polarisation-OAM hybrid entanglement, a quantum eraser experiment can be performed in a delayed measure scheme where I treat OAM as an analogous path which can be distinguished and erased.

These results serve as a stepping stone to extending the study of wave-particle duality to other abstract variables in quantum mechanics. Previously, the study of particle-wave duality and the complementarity principle was pervasively explored through path interferometers. However, the scheme I presented introduces a new way of exploiting hybrid-entanglement to achieve the same result. An avenue to explore would be to perhaps implement the high dimensionality of OAM modes which could

expand the abstract paths of the eraser. Its interesting to ask whether multiple OAM "path" information could also be erased? This could serve as a potential method of confirming the entanglement of a compound quantum systems. For example, a Bell analysis becomes more difficult to implement in higher dimensions, but a quantum eraser procedure may also serve as an entanglement probe which could replace it. Implementing high dimensional (QKD) with entangled photons would benefit from this analysis in order to confirm the entanglement of the system. Therefore this technique may be useful in characterising quantum channels that use entangled photons.

In Chapter 5, I demonstrated the advantage of using the non-separable (entangled) vector modes and their mutually unbiased set of scalar modes, prepared and measured in Chapter 2, to demonstrate a high dimension QKD BB84 protocol. The high dimensional capabilities of theses spatial modes have not been exploited for quantum key distribution. Contrary to exploiting the reciprocity of q-plates, I engineered a system that resolves the mode sets in position enabling for their unambiguous detection deterministically. I showed that the detection scheme outperforms probabilistic sifting methods which may reduce the detection efficiency of the system and consequently reduce the key generation rate. The presented scheme has a high photon efficiency as compared to state-of-art which is desirable for high-rate secure key generation. The scheme yielded high fidelities, information capacity per photon and high key rates.

It may be necessary, in future, to study the impeding losses which were ignored in the system. As presented, the scheme makes use of an attenuated lasers source however, it is known that such sources do-not produce single photons all the time, making the scheme vulnerable to eavesdropping without detection. Interestingly, there are alternative protocols that only require random phase weakly coherent photon sources where unconditional security is still maintained even if the source emits more that one photon at a time [149]. It may be useful to investigate whether the scheme is secure against all forms of eavesdropping. The eavesdropping analysis I presented was based on a simulation which could be analysed better in an actual experiment.

Such an addition could give a better indication of the actual security of the system. I emphasise that the main aim of chapter 5 was to demonstrate that spatial modes of coupled DoF (hybrid photon states) can be used for QKD with the advantage of high dimensional encoding. However, for a full practical implementation (full characterisation of the photon source and eavesdropping) needs to be considered and I aim to address this in future work.

In summary I have shown the following:

(1) Through hybrid entanglement, the fundamental wave and particle nature of photons can be controlled even when abstracting the idea of physical paths to other DOF making the erasure of the OAM of a photon possible. Having such meticulous control is essential for quantum communication since the fundamental nature of photons is exploited for transmitting quantum information.

(2) High dimensional quantum key distribution with hybrid photonic states show a significant increase in data transfer rates as compared to quantum key distribution with conventional polarisation eigenstates. Through hybridised detection schemes, efficient and deterministic detection systems are easily realisable which may enable for efficient key generation with spatial modes with high key rates relevant for secure quantum communication.

Appendix A

Bell inequality derivation

It was Bell who showed that the quirkiness of quantum entanglement could not be accounted for by local hidden variable theories [12]. He derived inequalities based on the EPR assumptions. This places a restriction on a system that satisfies classical correlations under local hidden variable theories. Clauser, Horne Shimony and Holt (CHSH) [87] later extended these inequalities, making them useful for experimental demonstrations in optics.

To derive the inequalities, Bell adopted the EPR assumptions thus assuming the existence of a hidden variables, λ, with a normalised distribution $p(\lambda)$ that mediates maximal correlations between two spatially separated photons,

$$\int p(\lambda)d\lambda = 1. \tag{A.1}$$

Measuring the two subsystems in single DOF, say polarisation, requires that the polarisation analysers are orientated at α and β, respectively, for each photon which is treated as individual subsystem. Suppose the outcome of measuring the signal (s) photon at an orientation α (as in Fig. A.1) is $A(\alpha, \lambda) = 1$ for the right (R) circular polarization and $A(\alpha, \lambda) = -1$ for left (L) circular polarisation states. Similarly, for the idler (i), we obtain (L, $B(\beta, \lambda) = 1$) and (R, $B(\beta, \lambda) = -1$). The expectation
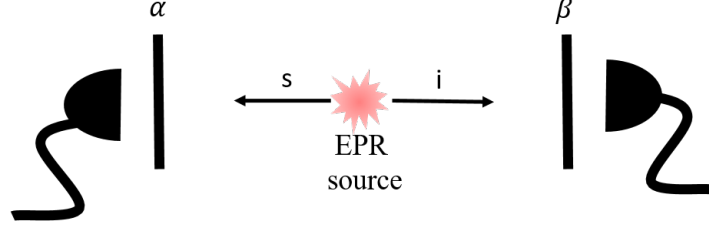
Figure A-1: An EPR like correlated system where an EPR source sends two particles that are spatially separated in the paths of the signal (s) and idler (i) where correlated measurements are performed at each end.

value of polarisation measurements performed on the compound system is given by

$$P(\alpha, \beta) = \int A(\alpha, \lambda) B(\beta, \lambda)(\lambda) d\lambda. \tag{A.2}$$

It follows that

$$P(\alpha, \beta) - P(\alpha, \beta') = \int \Big(A(\alpha, \lambda) B(\beta, \lambda) - A(\alpha, \lambda) B(\beta, \lambda) \Big) p(\lambda) d\lambda. \tag{A.3}$$

If we define $\Phi_{\alpha', \beta}(\lambda) = A(\alpha', \lambda) B(\beta', \lambda)$ and manipulate Eq. A.3, we obtain

$$
\begin{aligned}
P(\alpha, \beta) - P(\alpha, \beta') &= \int \Big(\Phi_{\alpha, \beta}(\lambda) \big(1 \pm \Phi_{\alpha', \beta'}(\lambda) \big) \\
&\quad - \Phi_{\alpha, \beta'}(\lambda) \big(1 \pm \Phi_{\alpha', \beta}(\lambda) \big) \Big) \ p(\lambda) d\lambda.
\end{aligned}
\tag{A.4}
$$

Taking the absolute value of both sides if the equation and applying the triangle inequality yields,

$$
\begin{aligned}
|P(\alpha, \beta)| - |P(\alpha, \beta')| &\leq \int |\Phi_{\alpha, \beta}(\lambda)| \big(1 \pm \Phi_{\alpha', \beta'}(\lambda) \big) \ p(\lambda) d\lambda \\
&\quad + \int |\Phi_{\alpha, \beta'}(\lambda)| \big(1 \pm \Phi_{\alpha', \beta}(\lambda) \big) \ p(\lambda) d\lambda.
\end{aligned}
\tag{A.5}
$$

Noting that $|A(\theta, \lambda)| \leq 1$ and $|B(\theta, \lambda)| \leq 1 \ \forall \theta$, it follows that

$$
\begin{aligned}
|P(\alpha, \beta)| - |P(\alpha, \beta')| &\leq \int \big(1 \pm \Phi_{\alpha', \beta'}(\lambda) \big) \ p(\lambda) d\lambda \\
&\quad + \int \big(1 \pm \Phi_{\alpha', \beta}(\lambda) \big) \ p(\lambda) d\lambda..
\end{aligned}
\tag{A.6}
$$

92

By Eq. (A.1) it follows that Eq. (A.7) simplifies to

$$|P(\alpha, \beta) - P(\alpha, \beta')| \leq 2 \pm |P(\alpha', \beta') + P(\alpha', \beta)|. \tag{A.7}$$

By choosing the equation with $\leq 2 - |P(\alpha', \beta) + P(\alpha', \beta)|$ on the left hand side, it holds that

$$|P(\alpha, \beta) - P(\alpha, \beta')| + |P(\alpha', \beta') + P(\alpha', \beta)| \leq 2. \tag{A.8}$$

Using the triangle inequality yields the CHSH/Bell inequality,

$$|P(\alpha, \beta) - P(\alpha, \beta') + P(\alpha', \beta') + P(\alpha', \beta)| \leq 2, \tag{A.9}$$

where the left hand side represents the correlations between the two subsystems which is usually denoted as S. Therefore Eq. (A.9) constrains a correlated system under the assumption of local hidden variables and independent of the outcome of measurements on each subsystem (EPR). A violation ($S > 2$) would thus prove the entanglement of the system.

Appendix B

Detection schemes

To compare deterministic and filter-based detection schemes, consider a state $|\psi_\ell\rangle$ in a d-dimensional Hilbert space $\mathcal{H}_d$. We will assume that the states $|\psi_\ell\rangle$ are eigenstates of a given observable $\mathcal{O}$ (e.g., polarization, orbital angular momentum, or any other degree of freedom of the photon). Suppose Alice prepares her photon in an arbitrary state $|\psi_\ell\rangle$. First, consider the case where Bob decides to measure the photons using a filter based approach; that is, Bob performs a strong measurement or projection onto the eigenstates of $\mathcal{O}$: $\mathcal{P}_{\ell'} = |\psi_{\ell'}\rangle\langle\psi_{\ell'}|$. The ideal measurement apparatus to probe the $\mathcal{H}_d$, must produce a unit probability of detection for a given eigenstate $|\psi_\ell\rangle$ that Alice prepares: $\mathcal{P}_{\ell'}|\psi_\ell\rangle = \delta_{\ell,\ell'}|\psi_{\ell'}\rangle$. Thus, the operator for the ideal filter based measurement apparatus takes the form

$$\mathcal{P} = \sum_{\ell'} |\psi_{\ell'}\rangle\langle\psi_{\ell'}|. \tag{B.1}$$

In dimensions $d > 2$, it is not possible perform the projection $\mathcal{P}$ with traditional measuring apparatus such as using digital holograms or a geometric phase plate because these optical elements modulate the photons such that their transformation $\mathcal{T} = |\psi\rangle\langle\psi|$ is described by

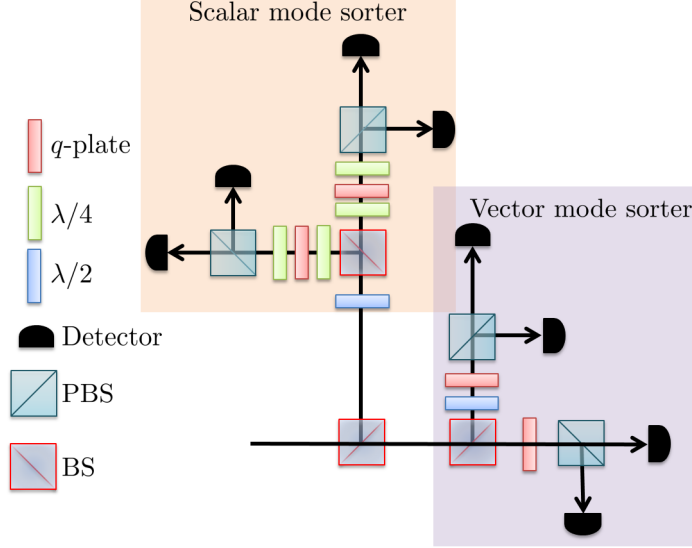$$|\psi\rangle = \sum_{\ell''} c_{\ell''} |\psi_{\ell''}\rangle, \tag{B.2}$$

Figure B-1: The combination of wave-plates ($\frac{\lambda}{4}$, $\frac{\lambda}{2}$), q-plates and 50/50 (BS) and polarisation (PBS) beam splitters can serve as a detection system. The wave plates can be rotated at angles shown in Table.5.1.

where $|c_{\ell''}|^2$ is the probability of measuring the state $|\psi_{\ell''}\rangle$. With this approach, the high-dimensional space needs to be probed *one mode at a time*. Thus all the d detectors will return a positive detection with an average probability of $|c_{\ell''}|^2 \leq 1/d$.

The filter based detection system used in this study depends on the use of beam splitters with a combination with q-plates, wave plates and polarizers. While it is common practice for the measurement process to be identical to the generation for reversible processes – as is the case in linear optics – this approach would fail in measuring high dimensional vector mode spaces. This is because vector modes within one subset required oppositely charged q-plates. The best approach to probe the high dimensional space would require the use of beam splitters as shown in Fig. B-1, however, at the cost of reducing the detection probability by a factor of 1/2, thus halving the sift rate and secure key rate; for a key that is N-bit long, one would require sending, on average, $4N$ bits. We have tested this by building the system depicted in Fig. B-1 and performing the same prepare and measure QKD protocol as detailed in the main text. For a 200 bit transmission we were only able to produce a key with 25% of the transmitted bits, as compared to 50% using the scheme described in Fig. 5-3 of Chapter 5. This highlights one of the advantages of a deterministic

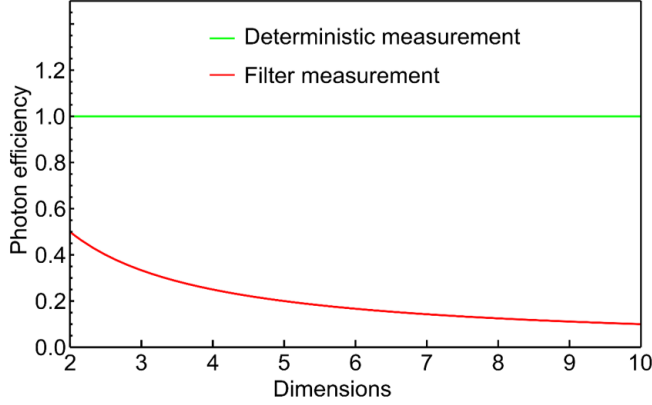detection system versus the probabilistic (filter-based) system.

Figure B-2: Photon efficiency as a function of dimension for a deterministic and filter-based measurement scheme.

The advantage of our approach is graphically depicted in Fig. B-2, where we plot, as a function of the dimension, the photon efficiency of the detection: defined as $1 - S$ where S is the fraction of photons whose information is lost due to measurement approach. Using a filter based detection, the efficiency of the protocol degrades in higher dimensions as opposed to our scheme that, in principle, allows operation at maximum efficiency for high bit rate quantum key distribution. The sifting losses can, however, be reduced by a factor of 2 with OAM vector modes for example. Using a combination of geometric phase plates and polarizing beam splitters, the OAM vector mode is first projected onto OAM then polarization states. The key in using vector modes lies in the final projection onto polarization states. Because polarization is two-dimensional, a null detection of one of the eigenstates automatically translates in a positive detection of the orthogonal eigenstate with unit probability. For demonstration purposes, consider the following input vector mode:

$$|\psi_\ell^\pm\rangle = \frac{1}{\sqrt{2}} \left(|\ell, R\rangle \pm |-\ell, L\rangle \right), \tag{B.3}$$

where L and R are the left- and right-circular polarization. By passing such a vector mode through a q-plate with topological charge $2q = |\ell|$, we obtain the following state

$$|\psi_{\ell}'^{\pm}\rangle = \frac{1}{\sqrt{2}} |0\rangle \left(|R\rangle \pm |L\rangle \right). \tag{B.4}$$

While and input $|\psi_{\ell}^{+}\rangle$ results in a horizontally polarized Gaussian mode ($\ell = 0$), the orthogonal vector mode $|\psi_{\ell}^{-}\rangle$ results in a vertically polarized Gaussian mode. The two modes can thus be separated using a polarizing beam splitter. The same approach can be taken for the other two vector modes $|\psi_{-\ell}^{\pm}\rangle$. Using this principle, it is possible to probe the hybrid, high-dimensional polarization-OAM space, two modes at the time. This translates in half the sifting loss of the filtering approach detailed in the section above.

Bibliography

[1] R. Horodecki, P. Horodecki, M. Horodecki, and K. Horodecki, "Quantum entanglement," *Reviews of Modern Physics*, vol. 81, no. 2, p. 865, 2009.

[2] M. A. Nielsen and I. Chuang, *Quantum computation and quantum information.* 2002.

[3] D. Bouwmeester, J.-W. Pan, K. Mattle, M. Eibl, H. Weinfurter, and A. Zeilinger, "Experimental quantum teleportation," *Nature*, vol. 390, no. 6660, pp. 575–579, 1997.

[4] C. H. Bennett and S. J. Wiesner, "Communication via one-and two-particle operators on Einstein-Podolsky-Rosen states," *Physical Review Letters*, vol. 69, no. 20, p. 2881, 1992.

[5] K. Mattle, H. Weinfurter, P. G. Kwiat, and A. Zeilinger, "Dense coding in experimental quantum communication," *Physical Review Letters*, vol. 76, no. 25, p. 4656, 1996.

[6] C. H. Bennett, "Quantum cryptography: Public key distribution and coin tossing," in *International Conference on Computer System and Signal Processing, IEEE, 1984*, pp. 175–179, 1984.

[7] A. K. Ekert, "Quantum cryptography based on Bells theorem," *Physical Review Letters*, vol. 67, no. 6, p. 661, 1991.

[8] J. T. Barreiro, T.-C. Wei, and P. G. Kwiat, "Beating the channel capacity limit for linear photonic superdense coding," *Nature Physics*, vol. 4, no. 4, pp. 282–286, 2008.

[9] L. Neves, G. Lima, A. Delgado, and C. Saavedra, "Hybrid photonic entanglement: Realization, characterization, and applications," *Physical Review A*, vol. 80, no. 4, p. 042322, 2009.

[10] L. Marrucci, E. Karimi, S. Slussarenko, B. Piccirillo, E. Santamato, E. Nagali, and F. Sciarrino, "Spin-to-orbital conversion of the angular momentum of light and its classical and quantum applications," *Journal of Optics*, vol. 13, no. 6, p. 064001, 2011.

[11] A. Einstein, B. Podolsky, and N. Rosen, "Can quantum-mechanical description of physical reality be considered complete?," *Physical Review*, vol. 47, no. 10, p. 777, 1935.

[12] J. S. Bell, "On the Einstein Podolsky Rosen paradox," *Physics*, vol. 1, no. 3, pp. 369–371, 1964.

[13] D. J. Griffiths, *Introduction to quantum mechanics*. Cambridge University Press, 2016.

[14] A. Aspect, P. Grangier, and G. Roger, "Experimental tests of realistic local theories via Bell's theorem," *Physical Review Letters*, vol. 47, no. 7, p. 460, 1981.

[15] A. Aspect, P. Grangier, and G. Roger, "Experimental realization of Einstein-Podolsky-Rosen-Bohm Gedankenexperiment: a new violation of Bell's inequalities," *Physical Review Letters*, vol. 49, no. 2, p. 91, 1982.

[16] P. G. Kwiat, E. Waks, A. G. White, I. Appelbaum, and P. H. Eberhard, "Ultrabright source of polarization-entangled photons," *Physical Review A*, vol. 60, no. 2, p. R773, 1999.

[17] R. T. Thew, S. Tanzilli, W. Tittel, H. Zbinden, and N. Gisin, "Experimental investigation of the robustness of partially entangled qubits over 11 km," *Physical Review A*, vol. 66, no. 6, p. 062304, 2002.

[18] H. De Riedmatten, I. Marcikic, V. Scarani, W. Tittel, H. Zbinden, and N. Gisin, "Tailoring photonic entanglement in high-dimensional Hilbert spaces," *Physical Review A*, vol. 69, no. 5, p. 050304, 2004.

[19] D. Stucki, H. Zbinden, and N. Gisin, "A Fabry–Perot-like two-photon interferometer for high-dimensional time-bin entanglement," *Journal of Modern Optics*, vol. 52, no. 18, pp. 2637–2648, 2005.

[20] A. Mair, A. Vaziri, G. Weihs, and A. Zeilinger, "Entanglement of the orbital angular momentum states of photons," *Nature*, vol. 412, no. 6844, pp. 313–316, 2001.

[21] A. C. Dada, J. Leach, G. S. Buller, M. J. Padgett, and E. Andersson, "Experimental high-dimensional two-photon entanglement and violations of generalized Bell inequalities," *Nature Physics*, vol. 7, no. 9, pp. 677–680, 2011.

[22] J. Leach, B. Jack, J. Romero, M. Ritsch-Marte, R. Boyd, A. Jha, S. Barnett, S. Franke-Arnold, and M. Padgett, "Violation of a Bell inequality in two-dimensional orbital angular momentum state-spaces," *Optics Express*, vol. 17, no. 10, pp. 8287–8293, 2009.

[23] M. McLaren, M. Agnew, J. Leach, F. S. Roux, M. J. Padgett, R. W. Boyd, and A. Forbes, "Entangled bessel-gaussian beams," *Optics Express*, vol. 20, no. 21, pp. 23589–23597, 2012.

[24] M. O. Scully, B.-G. Englert, and H. Walther, "Quantum optical tests of complementarity," *Nature*, vol. 351, pp. 111–116, 1991.

[25] S. Walborn, M. T. Cunha, S. Pádua, and C. Monken, "Double-slit quantum eraser," *Physical Review A*, vol. 65, no. 3, p. 033818, 2002.

[26] X.-S. Ma, J. Kofler, A. Qarry, N. Tetik, T. Scheidl, R. Ursin, S. Ramelow, T. Herbst, L. Ratschbacher, A. Fedrizzi, *et al.*, "Quantum erasure with causally disconnected choice," *Proceedings of the National Academy of Sciences*, vol. 110, no. 4, pp. 1221–1226, 2013.

[27] D. L. Andrews and M. Babiker, *The angular momentum of light.* Cambridge University Press, 2012.

[28] L. Allen, M. W. Beijersbergen, R. Spreeuw, and J. Woerdman, "Orbital angular momentum of light and the transformation of Laguerre-Gaussian laser modes," *Physical Review A*, vol. 45, no. 11, p. 8185, 1992.

[29] G. Molina-Terriza, J. P. Torres, and L. Torner, "Twisted photons," *Nature Physics*, vol. 3, no. 5, pp. 305–310, 2007.

[30] J. P. Torres and L. Torner, *Twisted photons: applications of light with orbital angular momentum.* John Wiley & Sons, 2011.

[31] S. Franke-Arnold, L. Allen, and M. Padgett, "Advances in optical angular momentum," *Laser & Photonics Reviews*, vol. 2, no. 4, pp. 299–313, 2008.

[32] H. Rubinsztein-Dunlop, A. Forbes, M. Berry, M. Dennis, D. L. Andrews, M. Mansuripur, C. Denz, C. Alpmann, P. Banzer, T. Bauer, *et al.*, "Roadmap on structured light," *Journal of Optics*, vol. 19, no. 1, p. 013001, 2016.

[33] M. A. Bandres and J. C. Gutiérrez-Vega, "Ince–gaussian beams," *Optics Letters*, vol. 29, no. 2, pp. 144–146, 2004.

[34] F. Gori, G. Guattari, and C. Padovani, "Bessel-gauss beams," *Optics Communications*, vol. 64, no. 6, pp. 491–495, 1987.

[35] G. Milione, H. Sztul, D. Nolan, and R. Alfano, "Higher-order poincaré sphere, stokes parameters, and the angular momentum of light," *Physical Review Letters*, vol. 107, no. 5, p. 053601, 2011.

[36] M. McLaren, T. Konrad, and A. Forbes, "Measuring the nonseparability of vector vortex beams," *Physical Review A*, vol. 92, no. 2, p. 023833, 2015.

[37] E. Karimi, J. Leach, S. Slussarenko, B. Piccirillo, L. Marrucci, L. Chen, W. She, S. Franke-Arnold, M. J. Padgett, and E. Santamato, "Spin-orbit hybrid entanglement of photons and quantum contextuality," *Physical Review A*, vol. 82, no. 2, p. 022115, 2010.

[38] E. Nagali, L. Sansoni, L. Marrucci, E. Santamato, and F. Sciarrino, "Experimental generation and characterization of single-photon hybrid ququarts based on polarization and orbital angular momentum encoding," *Physical Review A*, vol. 81, no. 5, p. 052317, 2010.

[39] B. Gadway, E. Galvez, and F. De Zela, "Bell-inequality violations with single photons entangled in momentum and polarization," *Journal of Physics B: Atomic, Molecular and Optical Physics*, vol. 42, no. 1, p. 015503, 2008.

[40] Y. Hasegawa, R. Loidl, G. Badurek, M. Baron, and H. Rauch, "Violation of a bell-like inequality in single-neutron interferometry," *Nature*, vol. 425, no. 6953, pp. 45–48, 2003.

[41] F. Cardano, E. Karimi, S. Slussarenko, L. Marrucci, C. de Lisio, and E. Santamato, "Polarization pattern of vector vortex beams generated by q-plates with different topological charges," *Applied Optics*, vol. 51, no. 10, pp. C1–C6, 2012.

[42] Q. Zhan, "Cylindrical vector beams: from mathematical concepts to applications," *Advances in Optics and Photonics*, vol. 1, no. 1, pp. 1–57, 2009.

[43] G. Volpe and D. Petrov, "Generation of cylindrical vector beams with few-mode fibers excited by Laguerre–Gaussian beams," *Optics Communications*, vol. 237, no. 1, pp. 89–95, 2004.

[44] G. Milione, M. P. Lavery, H. Huang, Y. Ren, G. Xie, T. A. Nguyen, E. Karimi, L. Marrucci, D. A. Nolan, R. R. Alfano, *et al.*, "4× 20 gbit/s mode division

multiplexing over free space using vector modes and a q-plate mode (de) multiplexer," *Optics Letters*, vol. 40, no. 9, pp. 1980–1983, 2015.

[45] B. Ndagano, B. Perez-Garcia, F. S. Roux, M. McLaren, C. Rosales-Guzman, Y. Zhang, O. Mouane, R. I. Hernandez-Aranda, T. Konrad, and A. Forbes, "Characterizing quantum channels with non-separable states of classical light," *Nature Physics*, vol. 13, no. 4, pp. 397–402, 2017.

[46] G. Vallone, V. DAmbrosio, A. Sponselli, S. Slussarenko, L. Marrucci, F. Sciarrino, and P. Villoresi, "Free-space quantum key distribution by rotation-invariant twisted photons," *Physical Review Letters*, vol. 113, no. 6, p. 060503, 2014.

[47] H. Bechmann-Pasquinucci and W. Tittel, "Quantum cryptography using larger alphabets," *Physical Review A*, vol. 61, no. 6, p. 062308, 2000.

[48] N. J. Cerf, M. Bourennane, A. Karlsson, and N. Gisin, "Security of quantum key distribution using d-level systems," *Physical Review Letters*, vol. 88, no. 12, p. 127902, 2002.

[49] R. L. Rivest, A. Shamir, and L. Adleman, "A method for obtaining digital signatures and public-key cryptosystems," *Communications of the ACM*, vol. 21, no. 2, pp. 120–126, 1978.

[50] A. Ekert and R. Jozsa, "Quantum computation and Shor's factoring algorithm," *Reviews of Modern Physics*, vol. 68, no. 3, p. 733, 1996.

[51] A. Klappenecker and M. Rotteler, "Constructions of mutually unbiased bases," *Lecture Notes in Computer Science*, pp. 137–144, 2003.

[52] W. K. Wootters and W. H. Zurek, "A single quantum cannot be cloned," *Nature*, vol. 299, no. 5886, pp. 802–803, 1982.

[53] D. Dieks, "Communication by EPR devices," *Physics Letters A*, vol. 92, no. 6, pp. 271–272, 1982.

[54] H. F. Chau, "Practical scheme to share a secret key through a quantum channel with a 27.6% bit error rate," *Physical Review A*, vol. 66, no. 6, p. 060302, 2002.

[55] A. Ferenczi and N. Lütkenhaus, "Symmetries in quantum key distribution and the connection between optimal attacks and optimal cloning," *Physical Review A*, vol. 85, no. 5, p. 052310, 2012.

[56] M. Mafu, A. Dudley, S. Goyal, D. Giovannini, M. McLaren, M. J. Padgett, T. Konrad, F. Petruccione, N. Lütkenhaus, and A. Forbes, "Higher-dimensional orbital-angular-momentum-based quantum key distribution with mutually unbiased bases," *Physical Review A*, vol. 88, no. 3, p. 032305, 2013.

[57] S. P. Walborn, D. S. Lemelle, M. P. Almeida, and P. H. S. Ribeiro, "Quantum Key Distribution with Higher-Order Alphabets Using Spatially Encoded Qudits," *Physical Review Letters*, vol. 96, p. 090501, Mar 2006.

[58] M. Mirhosseini, O. S. Magaña-Loaiza, M. N. OSullivan, B. Rodenburg, M. Malik, M. P. Lavery, M. J. Padgett, D. J. Gauthier, and R. W. Boyd, "High-dimensional quantum cryptography with twisted light," *New Journal of Physics*, vol. 17, no. 3, p. 033033, 2015.

[59] M. Beijersbergen, R. Coerwinkel, M. Kristensen, and J. Woerdman, "Helical-wavefront laser beams produced with a spiral phaseplate," *Optics Communications*, vol. 112, no. 5-6, pp. 321–327, 1994.

[60] F. S. Roux and Y. Zhang, "Projective measurements in quantum and classical optical systems," *Physical Review A*, vol. 90, no. 3, p. 033835, 2014.

[61] K. Yonezawa, Y. Kozawa, and S. Sato, "Generation of a radially polarized laser beam by use of the birefringence of a c-cut Nd: YVO4 crystal," *Optics Letters*, vol. 31, no. 14, pp. 2151–2153, 2006.

[62] G. Machavariani, Y. Lumer, I. Moshe, A. Meir, S. Jackel, and N. Davidson, "Birefringence-induced bifocusing for selection of radially or azimuthally polarized laser modes," *Applied Optics*, vol. 46, no. 16, pp. 3304–3310, 2007.

[63] K. Yonezawa, Y. Kozawa, and S. Sato, "Compact laser with radial polarization using birefringent laser medium," *Japanese Journal of Applied Physics*, vol. 46, no. 8R, p. 5160, 2007.

[64] J.-F. Bisson, J. Li, K. Ueda, and Y. Senatsky, "Radially polarized ring and arc beams of a neodymium laser with an intra-cavity axicon," *Optics Express*, vol. 14, no. 8, pp. 3304–3311, 2006.

[65] Y. Kozawa and S. Sato, "Generation of a radially polarized laser beam by use of a conical Brewster prism," *Optics Letters*, vol. 30, no. 22, pp. 3063–3065, 2005.

[66] M. A. Neil, F. Massoumian, R. Juškaitis, and T. Wilson, "Method for the generation of arbitrary complex vector wave fronts," *Optics Letters*, vol. 27, no. 21, pp. 1929–1931, 2002.

[67] C. Maurer, A. Jesacher, S. Fürhapter, S. Bernet, and M. Ritsch-Marte, "Tailoring of arbitrary optical vector beams," *New Journal of Physics*, vol. 9, no. 3, p. 78, 2007.

[68] X.-L. Wang, J. Ding, W.-J. Ni, C.-S. Guo, and H.-T. Wang, "Generation of arbitrary vector beams with a spatial light modulator and a common path interferometric arrangement," *Optics letters*, vol. 32, no. 24, pp. 3549–3551, 2007.

[69] Z. Bomzon, G. Biener, V. Kleiner, and E. Hasman, "Space-variant Pancharatnam–Berry phase optical elements with computer-generated subwavelength gratings," *Optics Letters*, vol. 27, no. 13, pp. 1141–1143, 2002.

[70] M. V. Berry, "Quantal phase factors accompanying adiabatic changes," in *Proceedings of the Royal Society of London A: Mathematical, Physical and Engineering Sciences*, vol. 392, pp. 45–57, The Royal Society, 1984.

[71] L. Marrucci, C. Manzo, and D. Paparo, "Optical spin-to-orbital angular momentum conversion in inhomogeneous anisotropic media," *Physical Review Letters*, vol. 96, no. 16, p. 163905, 2006.

[72] E. Nagali, F. Sciarrino, F. De Martini, L. Marrucci, B. Piccirillo, E. Karimi, and E. Santamato, "Quantum information transfer from spin to orbital angular momentum of photons," *Physical Review Letters*, vol. 103, no. 1, p. 013601, 2009.

[73] D. C. Burnham and D. L. Weinberg, "Observation of simultaneity in parametric production of optical photon pairs," *Physical Review Letters*, vol. 25, no. 2, p. 84, 1970.

[74] P. G. Kwiat, K. Mattle, H. Weinfurter, A. Zeilinger, A. V. Sergienko, and Y. Shih, "New high-intensity source of polarization-entangled photon pairs," *Physical Review Letters*, vol. 75, no. 24, p. 4337, 1995.

[75] A. Lamas-Linares, J. C. Howell, and D. Bouwmeester, "Stimulated emission of polarization-entangled photons," *Nature*, vol. 412, no. 6850, pp. 887–890, 2001.

[76] C. Cinelli, G. Di Nepi, F. De Martini, M. Barbieri, and P. Mataloni, "Parametric source of two-photon states with a tunable degree of entanglement and mixing: Experimental preparation of Werner states and maximally entangled mixed states," *Physical Review A*, vol. 70, no. 2, p. 022321, 2004.

[77] A. Rossi, G. Vallone, A. Chiuri, F. De Martini, and P. Mataloni, "Multipath entanglement of two photons," *Physical Review Letters*, vol. 102, no. 15, p. 153902, 2009.

[78] L. Neves, G. Lima, J. A. Gómez, C. Monken, C. Saavedra, and S. Pádua, "Generation of entangled states of qudits using twin photons," *Physical Review Letters*, vol. 94, no. 10, p. 100501, 2005.

[79] B. E. Saleh, A. F. Abouraddy, A. V. Sergienko, and M. C. Teich, "Duality between partial coherence and partial entanglement," *Physical Review A*, vol. 62, no. 4, p. 043816, 2000.

[80] F. M. Miatto, A. M. Yao, and S. M. Barnett, "Full characterization of the quantum spiral bandwidth of entangled biphotons," *Physical Review A*, vol. 83, no. 3, p. 033816, 2011.

[81] J. Torres, A. Alexandrescu, and L. Torner, "Quantum spiral bandwidth of entangled two-photon states," *Physical Review A*, vol. 68, no. 5, p. 050301, 2003.

[82] H. D. L. Pires, H. Florijn, and M. Van Exter, "Measurement of the spiral spectrum of entangled two-photon states," *Physical Review Letters*, vol. 104, no. 2, p. 020505, 2010.

[83] J. Romero, D. Giovannini, S. Franke-Arnold, S. Barnett, and M. Padgett, "Increasing the dimension in high-dimensional two-photon orbital angular momentum entanglement," *Physical Review A*, vol. 86, no. 1, p. 012334, 2012.

[84] D. Klyshko, "A simple method of preparing pure states of an optical field, of implementing the Einstein–Podolsky–Rosen experiment, and of demonstrating the complementarity principle," *Soviet Physics Uspekhi*, vol. 31, no. 1, p. 74, 1988.

[85] Y. Zhang, M. Mclaren, F. S. Roux, and A. Forbes, "Simulating spontaneous parametric down-conversion using classical light," in *SPIE Optical Engineering+ Applications*, pp. 919408–919408, International Society for Optics and Photonics, 2014.

[86] E.-K. Tan, J. Jeffers, S. M. Barnett, and D. T. Pegg, "Retrodictive states and two-photon quantum imaging," *The European Physical Journal D-Atomic, Molecular, Optical and Plasma Physics*, vol. 22, no. 3, pp. 495–499, 2003.

[87] J. F. Clauser, M. A. Horne, A. Shimony, and R. A. Holt, "Proposed experiment to test local hidden-variable theories," *Physical Review Letters*, vol. 23, no. 15, p. 880, 1969.

[88] S. J. Freedman and J. F. Clauser, "Experimental test of local hidden-variable theories," *Physical Review Letters*, vol. 28, no. 14, p. 938, 1972.

[89] J. F. Clauser and M. A. Horne, "Experimental consequences of objective local theories," *Physical Review D*, vol. 10, no. 2, p. 526, 1974.

[90] A. Aspect, J. Dalibard, and G. Roger, "Experimental test of Bell's inequalities using time-varying analyzers," *Physical Review Letters*, vol. 49, no. 25, p. 1804, 1982.

[91] B. S. Cirel'son, "Quantum generalizations of bell's inequality," *Letters in Mathematical Physics*, vol. 4, no. 2, pp. 93–100, 1980.

[92] B. Jack, J. Leach, H. Ritsch, S. Barnett, M. Padgett, and S. Franke-Arnold, "Precise quantum tomography of photon pairs with entangled orbital angular momentum," *New Journal of Physics*, vol. 11, no. 10, p. 103024, 2009.

[93] W. H. Press, S. Teukolsky, W. Vetterling, and B. Flannery, *Numerical Recipes.* Cambridge Univ. Press, 1992.

[94] R. Jozsa, "Fidelity for mixed quantum states," *Journal of Modern Optics*, vol. 41, no. 12, pp. 2315–2323, 1994.

[95] W. K. Wootters, "Entanglement of formation and concurrence.," *Quantum Information & Computation*, vol. 1, no. 1, pp. 27–44, 2001.

[96] N. K. Langford, R. B. Dalton, M. D. Harvey, J. L. OBrien, G. J. Pryde, A. Gilchrist, S. D. Bartlett, and A. G. White, "Measuring entangled qutrits and their use for quantum bit commitment," *Physical Review Letters*, vol. 93, no. 5, p. 053601, 2004.

[97] I. Nape, B. Ndagano, and A. Forbes, "Erasing the orbital angular momentum information of a photon," *Physical Review A*, vol. 95, no. 5, p. 053859, 2017.

[98] H. Rauch, W. Treimer, and U. Bonse, "Test of a single crystal neutron interferometer," *Physics Letters A*, vol. 47, no. 5, pp. 369–371, 1974.

[99] P. Grangier, G. Roger, and A. Aspect, "Experimental evidence for a photon anticorrelation effect on a beam splitter: a new light on single-photon interferences," *EPL (Europhysics Letters)*, vol. 1, no. 4, p. 173, 1986.

[100] A. Zeilinger, R. Gähler, C. Shull, W. Treimer, and W. Mampe, "Single-and double-slit diffraction of neutrons," *Reviews of Modern Physics*, vol. 60, no. 4, p. 1067, 1988.

[101] G. I. Taylor, "Interference fringes with feeble light," in *Proceedings of the Cambridge Philosophical Society*, vol. 15, pp. 114–115, 1909.

[102] S. Gerlich, S. Eibenberger, M. Tomandl, S. Nimmrichter, K. Hornberger, P. J. Fagan, J. Tüxen, M. Mayor, and M. Arndt, "Quantum interference of large organic molecules," *Nature Communications*, vol. 2, p. 263, 2011.

[103] N. Bohr *et al.*, *The quantum postulate and the recent development of atomic theory*, vol. 3. R. & R. Clarke, Limited, 1928.

[104] W. K. Wootters and W. H. Zurek, "Complementarity in the double-slit experiment: Quantum nonseparability and a quantitative statement of Bohr's principle," *Physical Review D*, vol. 19, no. 2, p. 473, 1979.

[105] D. M. Greenberger and A. Yasin, "Simultaneous wave and particle knowledge in a neutron interferometer," *Physics Letters A*, vol. 128, no. 8, pp. 391–394, 1988.

[106] G. Jaeger, A. Shimony, and L. Vaidman, "Two interferometric complementarities," *Physical Review A*, vol. 51, no. 1, p. 54, 1995.

[107] B.-G. Englert, "Fringe visibility and which-way information: An inequality," *Physical Review Letters*, vol. 77, no. 11, p. 2154, 1996.

[108] M. O. Scully and K. Drühl, "Quantum eraser: A proposed photon correlation experiment concerning observation and" delayed choice" in quantum mechanics," *Physical Review A*, vol. 25, no. 4, p. 2208, 1982.

[109] L. Neves, G. Lima, J. Aguirre, F. Torres-Ruiz, C. Saavedra, and A. Delgado, "Control of quantum interference in the quantum eraser," *New Journal of Physics*, vol. 11, no. 7, p. 073035, 2009.

[110] P. G. Kwiat, A. M. Steinberg, and R. Y. Chiao, "Observation of a quantum eraser: A revival of coherence in a two-photon interference experiment," *Physical Review A*, vol. 45, no. 11, p. 7729, 1992.

[111] T. J. Herzog, P. G. Kwiat, H. Weinfurter, and A. Zeilinger, "Complementarity and the quantum eraser," *Physical Review Letters*, vol. 75, no. 17, p. 3034, 1995.

[112] Y.-H. Kim, R. Yu, S. P. Kulik, Y. Shih, and M. O. Scully, "Delayed choice quantum eraser," *Physical Review Letters*, vol. 84, no. 1, p. 1, 2000.

[113] L. Chen, W. Zhang, K. Cai, Y. Zhang, and Q. Qi, "Revisiting the which-way experiment with twisted light beams," *Optics Letters*, vol. 39, no. 20, pp. 5897–5900, 2014.

[114] X.-s. Ma, J. Kofler, and A. Zeilinger, "Delayed-choice gedanken experiments and their realizations," *Reviews of Modern Physics*, vol. 88, no. 1, p. 015005, 2016.

[115] V. Jacques, E. Wu, F. Grosshans, F. Treussart, P. Grangier, A. Aspect, and J.-F. Roch, "Delayed-choice test of quantum complementarity with interfering single photons," *Physical Review Letters*, vol. 100, no. 22, p. 220402, 2008.

[116] L. Allen, M. Padgett, and M. Babiker, "IV The orbital angular momentum of light," *Progress in Optics*, vol. 39, pp. 291–372, 1999.

[117] E. Nagali and F. Sciarrino, "Generation of hybrid polarization-orbital angular momentum entangled states," *Optics Express*, vol. 18, no. 17, pp. 18243–18248, 2010.

[118] A. Forbes, A. Dudley, and M. McLaren, "Creation and detection of optical modes with spatial light modulators," *Advances in Optics and Photonics*, vol. 8, no. 2, pp. 200–227, 2016.

[119] R. Fickler, R. Lapkiewicz, W. N. Plick, M. Krenn, C. Schaeff, S. Ramelow, and A. Zeilinger, "Quantum entanglement of high angular momenta," *Science*, vol. 338, no. 6107, pp. 640–643, 2012.

[120] H. Hübel, M. R. Vanner, T. Lederer, B. Blauensteiner, T. Lorünser, A. Poppe, and A. Zeilinger, "High-fidelity transmission of polarization encoded qubits from an entangled source over 100 km of fiber.," *Optics Express*, vol. 15, no. 12, pp. 7853–7862, 2007.

[121] R. Ursin, F. Tiefenbacher, T. Schmitt-Manderbach, H. Weier, T. Scheidl, M. Lindenthal, B. Blauensteiner, T. Jennewein, J. Perdigues, P. Trojek, B. Ömer, M. Fürst, M. Meyenburg, J. Rarity, Z. Sodnik, C. Barbieri, H. Weinfurter, and A. Zeilinger, "Entanglement-based quantum communication over 144 km," *Nature Physics*, vol. 3, pp. 481–486, jul 2007.

[122] X.-S. Ma, T. Herbst, T. Scheidl, D. Wang, S. Kropatschek, W. Naylor, B. Wittmann, A. Mech, J. Kofler, E. Anisimova, V. Makarov, T. Jennewein, R. Ursin, and A. Zeilinger, "Quantum teleportation over 143 kilometres using active feed-forward.," *Nature*, vol. 489, pp. 269–73, sep 2012.

[123] T. Herbst, T. Scheidl, M. Fink, J. Handsteiner, B. Wittmann, R. Ursin, and A. Zeilinger, "Teleportation of entanglement over 143 km," *Proceedings of the National Academy of Sciences*, vol. 112, no. 46, pp. 14202–14205, 2015.

[124] T. Jennewein, C. Simon, G. Weihs, H. Weinfurter, and A. Zeilinger, "Quantum cryptography with entangled photons," *Physical Review Letters*, vol. 84, no. 20, pp. 4729–32, 2000.

[125] A. Poppe, A. Fedrizzi, R. Ursin, H. R. Bhm, T. Lornser, O. Maurhardt, M. Peev, M. Suda, C. Kurtsiefer, H. Weinfurter, T. Jennewein, and A. Zeilinger, "Practical quantum key distribution with polarization entangled photons," *Optics Express*, vol. 12, no. 16, p. 3865, 2004.

[126] C. Z. Peng, J. Zhang, D. Yang, W. B. Gao, H. X. Ma, H. Yin, H. P. Zeng, T. Yang, X. B. Wang, and J. W. Pan, "Experimental long-distance decoy-state quantum key distribution based on polarization encoding," *Physical Review Letters*, vol. 98, no. 1, pp. 2–5, 2007.

[127] J. Wang, J.-Y. Yang, I. M. Fazal, N. Ahmed, Y. Yan, H. Huang, Y. Ren, Y. Yue, S. Dolinar, M. Tur, and A. E. Willner, "Terabit free-space data transmission employing orbital angular momentum multiplexing," *Nature Photonics*, vol. 6, no. 7, pp. 488–496, 2012.

[128] V. Sleiffer, Y. Jung, V. Veljanovski, R. van Uden, M. Kuschnerov, H. Chen, B. Inan, L. G. Nielsen, Y. Sun, D. Richardson, S. Alam, F. Poletti, J. Sahu, A. Dhar, A. Koonen, B. Corbett, R. Winfield, A. Ellis, and H. de Waardt, "737 Tb/s (96 x 3 x 256-Gb/s) mode-division-multiplexed DP-16QAM transmission with inline MM-EDFA," *Optics Express*, vol. 20, p. B428, dec 2012.

[129] H. Huang, G. Xie, Y. Yan, N. Ahmed, Y. Ren, Y. Yue, D. Rogawski, M. J. Willner, B. I. Erkmen, K. M. Birnbaum, S. J. Dolinar, M. P. J. Lavery, M. J. Padgett, M. Tur, and A. E. Willner, "100 Tbit/s free-space data link enabled by three-dimensional multiplexing of orbital angular momentum, polarization, and wavelength," *Optics Letters*, vol. 39, p. 197, jan 2014.

[130] C. Souza, C. Borges, a. Khoury, J. Huguenin, L. Aolita, and S. Walborn, "Quantum key distribution without a shared reference frame," *Physical Review A*, vol. 77, pp. 1–4, 2008.

[131] G. Milione, T. A. Nguyen, J. Leach, D. A. Nolan, and R. R. Alfano, "Using the nonseparability of vector beams to encode information for optical communication," *Optics Letters*, vol. 40, no. 21, p. 4887, 2015.

[132] P. Li, B. Wang, and X. Zhang, "High-dimensional encoding based on classical nonseparability," *Optics Express*, vol. 24, p. 15143, jun 2016.

[133] G. Milione, M. P. J. Lavery, H. Huang, Y. Ren, G. Xie, T. A. Nguyen, E. Karimi, L. Marrucci, D. A. Nolan, R. R. Alfano, and A. E. Willner, "4 20 Gbit/s mode division multiplexing over free space using vector modes and a q-plate mode (de)multiplexer.," *Optics Letters*, vol. 40, no. 9, pp. 1980–3, 2015.

[134] G. Milione, H. I. Sztul, D. a. Nolan, and R. R. Alfano, "Higher-Order Poincaré Sphere, Stokes Parameters, and the Angular Momentum of Light," *Physical Review Letters*, vol. 107, p. 053601, jul 2011.

[135] G. Milione, S. Evans, D. a. Nolan, and R. R. Alfano, "Higher order Pancharatnam-Berry phase and the angular momentum of light," *Physical Review Letters*, vol. 108, no. 19, pp. 1–4, 2012.

[136] A. Forbes, A. Dudley, and M. McLaren, "Creation and detection of optical modes with spatial light modulators," *Advances in Optics and Photonics*, vol. 8, p. 200, jun 2016.

[137] D. Naidoo, F. S. Roux, A. Dudley, I. Litvin, B. Piccirillo, L. Marrucci, and A. Forbes, "Controlled generation of higher-order Poincaré sphere beams from a laser," *Nature Photonics*, vol. 10, pp. 327–332, Mar 2016.

[138] T. H. Lu, T. D. Huang, J. G. Wang, L. W. Wang, and R. R. Alfano, "Generation of flower high-order Poincaré sphere laser beams from a spatial light modulator," *Scientific Reports*, vol. 6, p. 39657, 2016.

[139] L. Marrucci, C. Manzo, and D. Paparo, "Optical Spin-to-Orbital Angular Momentum Conversion in Inhomogeneous Anisotropic Media," *Physical Review Letters*, vol. 96, p. 163905, apr 2006.

[140] R. Ionicioiu and A. Popescu, "Single-spin measurement using spin–orbital entanglement," *New Journal of Physics*, vol. 7, no. 1, p. 120, 2005.

[141] G. C. G. Berkhout, M. P. J. Lavery, J. Courtial, M. W. Beijersbergen, and M. J. Padgett, "Efficient Sorting of Orbital Angular Momentum States of Light," *Physical Review Letters*, vol. 105, p. 153601, oct 2010.

[142] R. Fickler, R. Lapkiewicz, M. Huber, M. P. Lavery, M. J. Padgett, and A. Zeilinger, "Interface between path and orbital angular momentum entanglement for high-dimensional photonic quantum information," *Nature Communications*, vol. 5, p. 5, 2014.

[143] M. P. J. Lavery, D. J. Robertson, A. Sponselli, J. Courtial, N. K. Steinhoff, G. A. Tyler, A. E. Wilner, and M. J. Padgett, "Efficient measurement of an optical orbital-angular-momentum spectrum comprising more than 50 states," *New Journal of Physics*, vol. 15, 2013.

[144] A. Dudley, T. Mhlanga, M. P. J. Lavery, A. McDonald, F. S. Roux, M. Padgett, and A. Forbes, "Efficient sorting of Bessel beams.," *Optics Express*, vol. 21, no. 1, pp. 165–71, 2013.

[145] B. Ndagano, R. Brüning, M. McLaren, M. Duparré, and A. Forbes, "Fiber propagation of vector modes," *Optics Express*, vol. 23, p. 17330, jun 2015.

[146] J. Leach, E. Bolduc, D. J. Gauthier, and R. W. Boyd, "Secure information capacity of photons entangled in many dimensions," *Physical Review A*, vol. 85, no. 6, p. 060304, 2012.

[147] G. Ruffato, M. Massari, and F. Romanato, "Diffractive optics for combined spatial-and mode-division demultiplexing of optical vortices: design, fabrication and optical characterization," *Scientific reports*, vol. 6, 2016.

[148] M. A. Cox, C. Rosales-Guzmán, M. P. J. Lavery, D. J. Versfeld, and A. Forbes, "On the resilience of scalar and vector vortex modes in turbulence," *Optics Express*, vol. 24, no. 16, p. 18105, 2016.

[149] H.-K. Lo, X. Ma, and K. Chen, "Decoy state quantum key distribution," *Physical Review Letters*, vol. 94, no. 23, p. 230504, 2005.